Superconducting Quantum Metamaterials

zur Erlangung des akademischen Grades

Doktor der Naturwissenschaften

von der KIT-Fakultät für Physik des

Karlsruher Instituts für Technologie (KIT)

genehmigte

Dissertation

von

M.Sc. Jan David Brehm

Tag der mündlichen Prüfung:	15.01.2021
Referent:	Prof. Dr. Alexey V. Ustinov
Korreferent:	Prof. Dr. Alexander Shnirman

Contents

1 Introduction

> "Not only is the universe stranger than we think, it is stranger than we can think."
>
> *Werner Heisenberg*
> *Across the Frontiers, 1975*

Quantum mechanics is one of the most successful theories of modern physics. It did not only help to explain countless physical phenomena, but entailed a vast impact on applications such as lasers and electronic devices, which are shaping our everyday life. To this date, the potential of quantum mechanics has by far not yet been exhausted. It was Dr. Richard Feynman in 1982, to suggest the use of quantum effects in the field of computing [Fey82]. By exploiting the quantum mechanical effects of superposition and entanglement, an exponential computational advantage can be achieved compared to a classical computer. Such computational advantage would be of tremendous importance for the simulation of quantum chemistry problems, which are exponentially hard for a classical computer [Bab+15; Lan+10; Hem+18]. Furthermore, the implementation of quantum algorithms such as Grover's search algorithm for searching lists [Gro97] or Shor's algorithm for factorization of prime numbers [Sho94] would outperform a classical computer and be of practical use.

At the heart of the quantum computer is the quantum bit (qubit) - a quantum two-level system ($|0\rangle, |1\rangle$). In contrast to its binary classical counterpart, its quantum state allows for any complex superposition of its states $|\psi\rangle = \alpha |0\rangle + \beta |1\rangle$. Over the years various physical implementations of qubits have been realized, including nitrogen-vacancies in diamonds [Dut+07], trapped ions [Lei+03], polarized photons [KLM01], quantum dots [Pet05], and superconducting qubits [CW08]. Since the demonstration of the first superconducting qubit in 1999 [NPT99], tremendous experimental progress has been made with an exponential increase in qubit coherence [DS13]. Although state of the art qubits still suffer significantly from decoherence [Kja+20], within the current era of NISQ (noisy intermediate scale

quantum computing) [Pre18] a breakthrough experiment with 53 qubits outperformed a classical supercomputer [Aru+19]. Furthermore, first basic quantum error correction schemes have been demonstrated with superconducting qubits [Kel+15; Ree+12; Cór+15]. With respect to these achievements, superconducting qubits have presented themselves as one of the most promising platforms for a future realization of a quantum computer.

A key ingredient of quantum computing and quantum information processing is strong light matter interaction: photons are not only used to excite, manipulate and to readout the qubits, but are also required to mediate interactions between them. Roughly speaking, the so-called *strong-coupling limit* is defined as the limit where the qubit coupling to a desired channel exceeds the coupling to other dissipative channels [Wal+04]. In most of today's quantum information systems strong coupling is achieved by embedding the qubit in a resonator or cavity. The interaction of qubits with the quantized single modes of cavities is treated in the framework of cavity quantum electrodynamics (cQED) [Bla+04]. Through the resonator, strong coupling can be realized and the qubit is simultaneously protected from noise of the environment. Even more importantly, the detuned resonator qubit system allows for a dispersive quantum non-demolition readout of the qubit state [Bla+04]. In more recent works a further enhancement of the coupling strength in multi-qubit cQED systems with a strong collective non-linear response was demonstrated [Shu+17; Yan+20; Sha+15; Mac+14].

A different approach is required when qubits should be strongly coupled to propagating light, as used for information exchange, instead of standing waves in a cavity. The coupling to propagating light can be achieved when the qubits are electromagnetically coupled to the mode continuum of a waveguide. However, in three-dimensional waveguides it is hard to reach a coherent and strong interaction of light and qubits due to spacial mode mismatches [RWF17]. By confining the waveguides to one dimension, strong [RWF17] and even ultra-strong [For+16] light-qubit interaction can be achieved. In analogy to cQED, the field of qubits interacting with the one-dimensional open space of a waveguide is considered as waveguide quantum electrodynamics (wQED) [Gu+17]. wQED systems have the appealing feature of providing a non-linearity, which is observable at the single photon level in an open space configuration. For single qubits coupled to a waveguide this gives rise to various non-linear quantum effects like the Mollow triplet, Autler-Townes splitting and anti-bunched light [Gu+17].

If multiple qubits are coupled to a common waveguide, it can be shown that the qubits obtain an infinite range interaction mediated by virtual and real photons in the waveguide [Lal+13]. Furthermore, this interaction also leads to collective qubit excitations, which can have radiative lifetimes much bigger (subradiance)

or much smaller (superradiance) than those of the constituting qubits [Lal+13]. The infinite range interaction between qubits could be of great benefit for multi-node quantum computing and quantum networks [Kim08], where propagating photons are used to transfer information between local processing units. Over the recent years numerous applications of multi-qubit wQED systems such as arbitrary Fock state synthesis [Pau+18; Gon+17], generation of entangled states [ZB19], number resolving photon detection [MC19], atomic mirrors [Cha+12], quantum computation [PKG16], and the generation of non-classical light [FZB14] have been proposed. A further highly relevant application would be the realization of slow and even stopped light [Eve+19] and quantum memories [LS12] based on a collective electromagnetically induced transparency protocol. A quantum memory would allow for coherent storage and on-demand retrieval of light pulses and is thus a crucial ingredient of a future quantum computer [LST09].

Besides applications in quantum information processing, a different way of viewing multi-qubit wQED systems is in the context of *quantum metamaterials* [ZFR16]. It extends the idea of classical metamaterials [SPW04] to a regime where its meta-atoms (qubits) can hold their quantum coherence longer than a light pulse traversing the medium. Similar to classical metamaterials, a large ensemble of qubits with periodic, but sub-wavelength inter-qubit spacings allows for an effective medium description. It is predicted that quantum metamaterials can provide global optical response functions that depend on the quantum state of the participating qubits [Rak+08]. Moreover, quantum metamaterials are expected to feature exotic localized polaritonic excitations [Zho+20]. Therefore, large scale multi-qubit wQED system do not only offer numerous applications in quantum information processing, but could also be used to study fundamental excitations in solids.

Experimentally, superconducting wQED systems with single qubits have been studied extensively. The first demonstration of resonance fluorescence was demonstrated by Astafiev et al. [Ast+10a] using a flux qubit coupled to a waveguide, followed by demonstrations of time resolved dynamics [Abd+11] and the Autler-Townes effect [Abd+10] as well as other non-linear effects like frequency mixing [Dmi+17; Hön+18] and amplification [Ast+10b]. Similar experiments with transmons [Hoi+13] showed generation of non-classical light, photon-photon correlations [Hoi+12] and an implementation of a single photon router [Hoi+11].

Even though superconducting qubits show the strongest light matter interaction compared to wQED systems based on other physical implementations [Gu+17], multi-qubit systems have been barely studied to this date. A first demonstration of super- and subradiance was given on a two-qubit wQED system [Loo+13]. Very recently an atomic mirror [Mir+19] and the generation of entangled photons [Kan+20] were demonstrated.

In this work, first experiments with one and two qubits are extended to multiple qubits in order to study cooperative effects in a scaled wQED system. We realize a densely spaced periodic array of eight transmon qubits with local frequency control, which are coupled to a common coplanar superconducting waveguide. In the first part of this thesis, we investigate the collective excitations of this quantum metamaterial [Bre+21]. The individual qubit tunability allows us to consecutively tune the qubits to a common resonance frequency and to observe their collective excitations in the transitioning regime between an individual qubit and a continuous band structure of a full-blown metamaterial. These collective excitations are delocalized polaritons, which have radiative relaxation rates ranging from extremely subradiant to superradiant compared to the individual qubits. Furthermore, we observe the emergence of a polaritonic band gap and present results on the collective Autler-Townes effect, which enables us to effectively control the band gap and the overall optical response of the metamaterial. Concluding the first part, the effect of artificial disorder on the transmission of light in the metamaterial is investigated, which might serve as a tool to study Anderson localization.

In the second part, we utilize the quantum metamaterial for a first realization of slow light in a superconducting wQED system, where the qubits are directly used as dispersive elements. Employing either the collective Autler-Townes effect or an engineered band structure, we are able to achieve a strong reduction of the group velocity of light. This paves the way towards the realization of a quantum memory in superconducting wQED.

In a concluding chapter, we present first experimental efforts to increase the system size to 90 non-tunable qubits. Our preliminary results show that it is possible to achieve a partial collective behavior even in the presence of disorder and also motivate further research in the direction of large scale wQED systems.

2 Superconducting Quantum Bits

This chapter provides a brief introduction to superconducting quantum bits (qubits). It is written for readers from other fields of research. First, the fundamental concept of an idealized two-level system and its mathematical description is provided, which is at the heart of all applications in quantum computing. It is followed by an introduction of the Josephson effect (quantum-tunneling of electron-pairs through a barrier), which provides a strong intrinsic non-linearity and is thus of crucial relevance for the experimental realization of almost all superconducting qubits. This chapter concludes with the introduction to a special kind of superconducting qubit called the *transmon*, which is not only the qubit of choice in this work, but one of the most widely and successfully used superconducting qubit to this date.

2.1 The Quantum Bit

2.1.1 Bloch Sphere

The basic building block of every quantum computer is the quantum bit (qubit). It is the quantum analogue to a classical bit, which can either be in state 0 or 1. The quantum state of a qubit $|\psi\rangle$ however allows for any complex superposition of these two states:

$$|\psi\rangle = \alpha\,|0\rangle + \beta\,|1\rangle = \alpha \begin{pmatrix} 0 \\ 1 \end{pmatrix} + \beta \begin{pmatrix} 1 \\ 0 \end{pmatrix} = \begin{pmatrix} \beta \\ \alpha \end{pmatrix}, \qquad \alpha, \beta \in \mathbb{C} \tag{2.1}$$

From the normalization condition of the wavefunction follows $\langle\psi|\psi\rangle = 1 = |\alpha|^2 + |\beta|^2$. In order to visualize the qubit state $|\psi\rangle$, it is typically regarded as a *Bloch vector* in three-dimensional real space [Kra+19]. Without the loss of generality it can be re-expressed in terms of spherical coordinates:

$$|\psi\rangle = \cos(\frac{\theta}{2})\,|0\rangle + \sin(\frac{\theta}{2})\exp(i\phi)\,|1\rangle\,, \quad 0 \leq \phi < 2\pi, \quad 0 \leq \theta \leq \pi \tag{2.2}$$

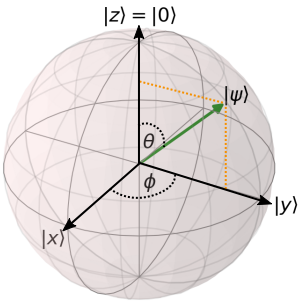

Figure 2.1: Schematic of the Bloch sphere. Every pure state $|\psi\rangle$ can be represented as a Bloch vector pointing to the surface of the Bloch sphere with radius 1. The axes of the three dimensional coordinate system are related via Eq. 2.3 with the states $|0\rangle, |1\rangle$ of the qubit.

By comparing a Bloch-unit vector $\mathbf{a} = \sin(\theta)\cos(\phi)\,|x\rangle + \sin(\theta)\sin(\phi)\,|y\rangle + \cos(\theta)\,|z\rangle$ with Eq. 2.2, the basis of the real space coordinate system can be associated with the qubit states via:

$$|x\rangle = \frac{1}{\sqrt{2}}(|0\rangle + |1\rangle) \quad |y\rangle = \frac{1}{\sqrt{2}}(|0\rangle + i\,|1\rangle) \quad |z\rangle = |0\rangle \tag{2.3}$$

With these relations at hand, any pure qubit state $|\psi\rangle$ can be visualized as a unit *Bloch-vector* lying on the surface of the *Bloch-sphere* (compare Fig. 2.1). It is noted that a qubit state in the Schroedinger picture evolves in time according to:

$$|\psi(t)\rangle = \exp(-i\omega_{10}\sigma_z t/2)\,|\psi(0)\rangle = \cos(\frac{\theta}{2})\,|0\rangle + \sin(\frac{\theta}{2})\exp(i(\phi - \omega_{10}t)\,|1\rangle \tag{2.4}$$

Here, ω_{10} denotes the qubit frequency and σ_z is the corresponding Pauli matrix with $\sigma_z\,|0\rangle = -\,|0\rangle$ and $\sigma_z\,|1\rangle = |1\rangle$. From Eq. 2.4 follows, that the Bloch vector $|\psi(t)\rangle$ is constantly precessing around the z-axis at the transition frequency of the qubit ω_{10}. In order to regard the qubit state as stationary, typically a transformation into the rotating reference frame of the qubit is applied. The transformation of the Hamilton operator H in a resting frame to the rotating frame (H') of the qubit can be achieved with:

$$H' = U(t)HU^{\dagger}(t) - i\hbar U(t)\dot{U}^{\dagger}(t) \quad \text{with} \quad U(t) = \exp(i\frac{\omega_{10}}{2}\sigma_z t) \tag{2.5}$$

2.1.2 Driving a Qubit

In order to manipulate the qubit, it can be driven with an oscillating microwave drive. The Hamilton operator of a driven two-level system is given by:

$$H = \hbar\frac{\omega_{10}}{2}\sigma_z + \hbar\Omega\cos(\omega t + \varphi)\sigma_x \tag{2.6}$$

Ω is the Rabi-strength of the drive, ω is its frequency, and φ accounts for a phase offset. For a the relation between the Rabi-strength Ω and the actual microwave power P driving the qubit, see section 5.3.2. It is instructive to transform Eq. 2.6 into a reference frame rotating with the frequency of the drive, such that a time independent Hamiltonian H' is obtained. This can be done by using again Eq. 2.5 with $U = \exp(i\omega\sigma_z t/2)$. Thus, in the rotating frame of the drive H' is given by:

$$H' \approx -\hbar\frac{\omega - \omega_{10}}{2}\sigma_z + \hbar\frac{\Omega}{2}(\cos(\varphi)\sigma_x + \sin(\varphi)\sigma_y) \tag{2.7}$$

Note that here the so-called rotating wave approximation (RWA) was applied, meaning that fast rotating terms in H'can be neglected ($\exp(\pm 2i\omega t) \approx 0$). Eq. 2.7 indicates that, depending on the phase-offset φ, the microwave drive induces a rotation around an axis in the xy-plane of the Bloch sphere. This can be better understood by calculating the time-dependent probability to find the qubit in the excited state $P_1(t) = |\langle 1|\psi(t)\rangle|^2$. Solving the time-dependent Schroedinger equation with H' from Eq. 2.7, with $\varphi = 0$ yields:

$$P_1(t) = |\langle 1|\psi(t)\rangle|^2 = \frac{\Omega^2}{\Omega^2 + \Delta^2}\sin^2\left(\frac{\sqrt{\Omega^2 + \Delta^2}t}{2}\right), \qquad \Delta = \omega_{10} - \omega \tag{2.8}$$

If the microwave drive is resonant with the qubit ($\Delta = 0$), Eq. 2.8 yields that the probability to find the qubit in the excited state oscillates periodically between zero and one. These drive-induced oscillations of a qubit are called Rabi oscillations.

2.1.3 Decoherence

In any realistic implementation of qubits the idealized picture of a perfectly isolated two-level is incomplete and can't fully capture its dynamics [Kra+19]. Since the qubits have to be controlled and read out from outside, they have to be coupled to the environment to some extend. Moreover, spurious couplings to the environment via for example electromagnetic modes cannot be avoided. Therefore a qubit is in fact an open quantum system and subject to noise and decoherence, which destroy the quantum state of the qubit. As such, the qubit state has to be characterized in terms of the density matrix ρ, because it allows for a statistical mixture of pure states $|\psi_i\rangle$ [Man20]:

$$\rho = \sum_i p_i |\psi_i\rangle\langle\psi_i| \qquad \sum_i p_i = 1 \tag{2.9}$$

Here, p_i is the probability to find the qubit in the state ψ_i. When mixed states are represented with the Bloch sphere, they are no longer lying on the surface, but inside the unit sphere [Kra+19].

The time evolution of the density matrix of a dissipative quantum system is described by the Lindblad master equation [Man20]:

$$\dot{\rho}(t) = -\frac{i}{\hbar}[H,\rho] + \sum_i \Gamma_i \mathcal{D}[A_i]\rho \quad \text{with} \quad \mathcal{D}[A]\rho = [A\rho A^\dagger - \frac{1}{2}\{A^\dagger A, \rho\}] \tag{2.10}$$

The first term on the right hand side of Eq. 2.10 describes the unitary time evolution of ρ, while the second term contains a sum over all decoherence channels of the corresponding system. Each of these channels is characterized by a decoherence rate Γ_i and a collapse operator A_i.

For the case of a two level system, which is subject to transversal and longitudinal noise, there are three decoherence channels with the collapse operators σ_+, σ_- and $\sigma_z/\sqrt{2}$[1]. In the limit of low temperatures ($k_B T \ll \omega_{10}\hbar$) thermal activation of the qubit through the environment via σ_+ can be excluded. The transversal decay rate is denoted with Γ_{10} and describes the energy relaxation of the qubit population. The longitudinal rate is denoted with Γ_ϕ and accounts for pure dephasing. With $H = \hbar\omega_{10}\sigma_z/2$ the Lindblad equation of the system is given by:

$$\begin{pmatrix} \dot{\rho}_{11} & \dot{\rho}_{10} \\ \dot{\rho}_{01} & \dot{\rho}_{00} \end{pmatrix} = \begin{pmatrix} 0 & -i\omega_{10}\rho_{10} \\ i\omega_{10}\rho_{01} & 0 \end{pmatrix} + \begin{pmatrix} -\Gamma_{10}\rho_{11} & -(\frac{\Gamma_{10}}{2} + \Gamma_\phi)\rho_{10} \\ -(\frac{\Gamma_{10}}{2} + \Gamma_\phi)\rho_{01} & \Gamma_{10}\rho_{11} \end{pmatrix} \tag{2.11}$$

Solving this set of differential equations yields

$$\rho(t) = \begin{pmatrix} a\exp(-t/T_1) & b\exp(-t/T_2)\exp(-i\omega_{10}t) \\ b^*\exp(-t/T_2)\exp(i\omega_{10}t) & 1 - a\exp(-t/T_1) \end{pmatrix} \tag{2.12}$$

Here, a and b are some introduced constants, which depend on the initial state of the qubit at $t = 0$. As can be seen from Eq. 2.12, the qubit population, which is given by ρ_{11} decays exponentially on a timescale given by $T_1 = 1/\Gamma_{10}$. The phase information of the qubit state decays exponentially too on a timescale given by $T_2 = 1/\gamma_{10} = 1/(\Gamma_{10}/2 + \Gamma_\phi)$.

2.2 Josephson Tunnel Barriers

2.2.1 A Brief Review of Superconductivity

Materials in the superconducting state feature a variety of hallmark phenomena, which separate them from conductors in the normal state. The most prominent

[1] $\sigma_+ = 1/2(\sigma_x - i\sigma_y)$, $\sigma_- = 1/2(\sigma_x + i\sigma_y)$

property of superconductors is the complete loss of electrical resistance below a certain critical temperature T_c. The effect was first observed in 1911 by H. Kamerlingh Onnes, in resistance measurements of mercury at different cryogenic temperatures [Kam11]. Several years later a further hallmark property was found by Meissner and Ochsenfeld [MO33]: superconductors can not be penetrated by magnetic fields smaller than a critical field-strength H_c. While this behavior resembles the one of any perfect conductor, a superconductor also repels magnetic field lines when being cooled down below T_c in the presence of a magnetic field. The Meissner-Ochsenfeld-Effect was explained in 1935 by F. London with the London equations [LLL35]. These phenomenologically derived equations explain the effect by the exponential decay of magnetic fields inside the superconductor on a characteristic length-scale λ_L. It took another 22 years until the the microscopic origin of superconductivity was explained in 1957 by Bardeen, Cooper and Schrieffer in the BCS-theory [BCS57]. They showed that a weak attractive interaction between electrons, which is mediated by phonons, can lead to an instability to the electronic groundstate of a superconductor and to a transition into a new superconducting groundstate at lower energy. This is caused by the pairing of electrons into bosonic particles called Cooper-pairs with zero spin and total momentum. A major prediction of the theory was that the quasi-particle excitation spectrum in a superconductor possesses an energy gap $\Delta(T)$ and that at least an energy of $E = 2\Delta(T)$ is required to create a pair of quasi-particle excitations [Tin04]. It is also the energy gap which causes the electrical resistance to vanish due to the lack of scattering states. Moreover the critical temperature T_c is connected with the gap energy by:

$$2\Delta(0) = 3.528 k_B T_c \tag{2.13}$$

A further important finding was that the BCS-groundstate (i.e. the electronic ground state of the superconducting condensate) can be described with a macroscopic wave function $\psi(r,t)$, with a well defined coherent phase $\theta(\mathbf{r},t)$ over the whole superconductor [Tin04]:

$$\psi(\mathbf{r},t) = \sqrt{n_s(\mathbf{r},t)}\exp\left(i\theta(\mathbf{r},t)\right) \tag{2.14}$$

$n_s(\mathbf{r},t)$ is the density of superconducting electrons. The number N of Cooper pairs (or their associated charge $Q = 2eN$) and the superconducting phase θ are conjugate variables and thus fulfill Heissenbergs uncertainty relation [Tin04]:

$$\delta N \delta\theta \gtrsim 1 \tag{2.15}$$

A further consequence of the macroscopic wave function in Eq. 2.14 is the quantization of magnetic fluxoids $\Phi = n\Phi_0$ penetrating a superconducting loop, since

the phase θ can only change by integer multiples of 2π around a ring. Φ_0 is the superconducting flux quantum:

$$\Phi_0 = \frac{h}{2e} \tag{2.16}$$

2.2.2 The Josephson Effect

In 1962 B. D. Josephson solved the problem of tunneling Cooper pairs through a thin insulating barrier between two superconductors (S-I-S) [Jos62]. He showed that the interference of the two macroscopic wavefunctions ψ_1 and ψ_2 of the two bulk superconductors leads to coherent tunneling of Cooper pairs in dependence on the phase difference $\varphi = \theta_1 - \theta_2$ between the superconductors (Fig. 2.2). The effect is described by two Josephson equations:

$$I = I_\mathrm{c} \sin \varphi \tag{2.17}$$

$$V = \frac{\Phi_0}{2\pi} \frac{\mathrm{d}\varphi}{\mathrm{d}t} \tag{2.18}$$

The first equation describes the remarkable property that a supercurrent I flows through the barrier between the two superconductors which depends only on the phase difference φ, without any voltage drop across the barrier. This is therefore also referred to as dc Josephson effect. The second equation states: if a dc current larger than a critical current I_c is applied to the junction, a voltage V appears across the barrier, which oscillates periodically in time and thus generates high frequency waves with $\omega = 2eV/\hbar$ [Sch+97]. Later it was found that the above equations do not only hold for S-I-S junctions, but in fact for every form of a weak link between two superconductors [Tin04]. The dependence of the critical current I_c on other model parameters, such as the used superconductors, junction geometry, room temperature resistance of the barrier R_n and temperature was solved by Ambegaokar and Baratoff for S-I-S type junctions [AB63]:

$$I_\mathrm{c} R_\mathrm{n} = \frac{\pi \Delta}{2e} \tanh\left(\frac{\Delta}{2k_\mathrm{B}T}\right) \tag{2.19}$$

Further, the energy stored in a Josephson junction is given by the integration of the electrical power with respect to time:

$$E = \int I(t)V(t)\,dt = \int I_\mathrm{c} \sin(\varphi) \frac{\Phi_0}{2\pi} \frac{\mathrm{d}\varphi}{\mathrm{d}t}\,dt = E_\mathrm{J}(1 - \cos(\varphi)) \tag{2.20}$$

Here, E_J is the Josephson energy defined by:

$$E_\mathrm{J} = \frac{\Phi_0}{2\pi} I_\mathrm{c} \tag{2.21}$$

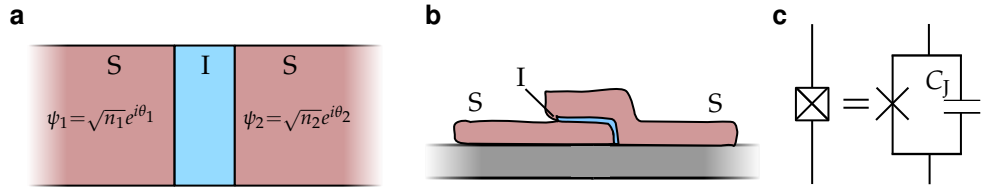

Figure 2.2: (a) Schematic of a Josephson tunneling barrier of S-I-S type. Left and right superconductors are described by macroscopic wave functions ψ_1 and ψ_2. (b) Actual realization of a Josephson junction with thin metallic films. (c) Circuit diagram of a Josephson junction. Note that the intrinsic capacitance C_J of the contact is accounted for.

Using Faradays law $V = -L_J \frac{\partial I}{\partial t}$ combined with Eq. 2.17 and Eq. 2.18, an effective inductance L_J can be associated to a Josephson junction:

$$L_J = \frac{\Phi_0}{2\pi I_c \cos(\varphi)} \tag{2.22}$$

It is noted that L_J is non-linear due to its dependence on the phase difference φ. As shown in the next section this non-linearity is of crucial importance for adding anharmonicity to the superconducting qubits, allowing to realize a two-state computational basis. As shown in Fig. 2.2, a real Josephson junction resembles a plate capacitor and therefore possesses a shunting capacitance C_J. Thus, a junction has the electrostatic charging energy:

$$\frac{1}{2} C_J U^2 = \frac{1}{2} C_J \left(\frac{Q}{C_J} \right)^2 = 4 E_c N^2 \quad \text{with} \quad E_c = \frac{e^2}{2C_J} \tag{2.23}$$

2.2.3 Superconducting Quantum Interference Devices

Superconducting Quantum Interference Devices (SQUIDs) are one of the most prominent applications of the Josephson effect. They are used for extremely sensitive detection of magnetic fields and the flux-tunability of superconducting resonators and qubits [Ken+19; Kra+19]. The most common type are dc SQUIDs, where two Josephson in parallel form a superconducting ring (Fig. 2.3(a)). The working principle of a dc SQUID is based on quantum interference between two supercurrents (I_a and I_b), passing through a ring penetrated by an external magnetic field B.

$$\begin{aligned} I_{tot} &= I_a + I_b && (2.24)\\ &= I_c \sin(\underbrace{\theta_2 - \theta_1}_{\varphi_a}) + I_c \sin(\underbrace{\theta_4 - \theta_3}_{\varphi_b}) && (2.25)\\ &= 2 I_c \sin((\varphi_a + \varphi_b)/2) \cos((\varphi_a - \varphi_b)/2) && (2.26) \end{aligned}$$

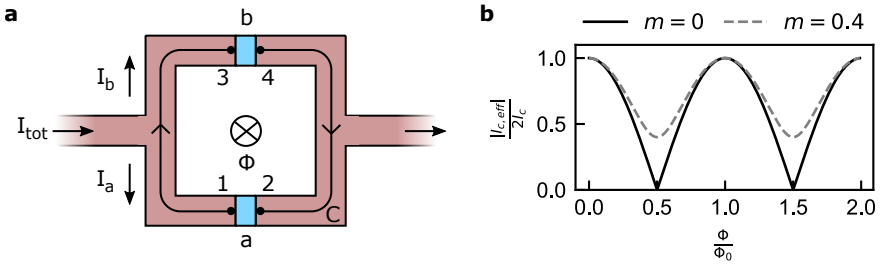

Figure 2.3: (a) Sketch of a dc superconducting quantum interference device (SQUID). The SQUID is formed by two Josephson junctions in parallel, forming a loop which encloses a magnetic flux Φ from an outer magnetic field density. (b) Absolute value of the SQUID's maximal super current $I_{c,eff}$ for symmetric and asymmetric Josephson junctions (see Eq. 2.29)).

Integrating the gauge invariant London equation $\mathbf{j} = \Lambda(\nabla\varphi - 2\pi/\Phi_0\mathbf{A})$ around the path C indicated in Fig. 2.3(a) under the assumption that $\mathbf{j} = 0$ in the middle of the ring, the following relation is obtained [Sch+97]:

$$\varphi_a - \varphi_b = \frac{2\pi}{\Phi_0}\oint_C \mathbf{A}\, d\mathbf{l} = \frac{2\pi\Phi}{\Phi_0} \tag{2.27}$$

Here, Φ is the magnetic flux penetrating the SQUID. Combining Eqs. 2.26 and 2.27 the total current through the SQUID is given by:

$$I_{tot} = I_{c,eff}\sin(\varphi_b + \frac{2\pi\Phi}{\Phi_0}) \quad \text{with} \quad I_{c,eff} = 2I_c\cos\left(\frac{\pi\Phi}{\Phi_0}\right) \tag{2.28}$$

The SQUIDs effective critical current $I_{c,eff}$ in Eq. 2.28 features a strong dependence on external magnetic fields and can thus be used as a magnetic sensor (Fig. 2.3(b)). If two different Josephson junctions with critical currents $I_{c,a}$ and $I_{c,b}$ are used to form a SQUID, $I_{c,eff}$ gets renormalized [Koc+07]:

$$I_{c,eff} = (I_{c,a} + I_{c,b})\cos\left(\frac{\pi\Phi}{\Phi_0}\right)\sqrt{1 + m^2\tan^2\left(\frac{\pi\Phi}{\Phi_0}\right)} \quad \text{with} \quad m = \frac{I_{c,a} - I_{c,b}}{I_{c,a} + I_{c,b}} \tag{2.29}$$

2.3 Physical Implementation of Superconducting Qubits

2.3.1 From a Josephson Junction to a Qubit

The properties of quantum circuits can be best understood by first studying the quantum harmonic oscillator, which is one of the most well-known models in

physics. In a superconducting electrical circuit, in the absence of restive losses, a quantum harmonic oscillator is realized by a capacitance C and an inductance L in parallel (Fig. 2.4(a)). If driven with a current, the electromagnetic energy stored in the inductor is associated with a potential energy and the charging energy of the capacitance is associated with a kinetic energy:

$$H = \frac{1}{2}CU^2 + \frac{1}{2}LI^2 = \frac{1}{2}\frac{Q^2}{C} + \frac{1}{2}\frac{\Phi^2}{L} = 4E_c N^2 + \frac{1}{2}E_L\varphi^2 \tag{2.30}$$

The so called node-flux Φ and charge Q are connected to the voltage V across the capacitor and the current I through the inductor by [VD17]:

$$Q(t) = \int_{-\infty}^{t} I(t')\,dt' \qquad \Phi(t) = \int_{-\infty}^{t} V(t')\,dt' \tag{2.31}$$

Equivalently, the dimensionless variables of charge number $N = Q/2e$ and phase $\varphi = \Phi 2\pi/\Phi_0$ can be used. $E_c = e^2/2C$ is the charging energy of the capacitor, i.e. the amount of energy needed to add a cooper pair to the capacitor, and $E_L = (\Phi_0/2\pi)^2/L$ the inductive energy. In the quantum regime the conjugate variables Φ and Q are replaced by non-commuting operators $\hat{\Phi}$, $\hat{Q}$ with $[\hat{\Phi}, \hat{Q}] = i\hbar$. Using the second quantization procedure with $\hat{Q} \propto i(a^\dagger - a)$ and $\hat{\Phi} \propto (a + a^\dagger)$ Eq. 2.30 reduces to [Kra+19]:

$$H = \hbar\omega_r \left(a^\dagger a + \frac{1}{2}\right) \quad \text{with} \quad \omega_r = \frac{1}{\sqrt{LC}} \tag{2.32}$$

As depicted in Fig. 2.4(a) the eigenenergies of the quantum harmonic oscillator are equally spaced by its resonance frequency $\hbar\omega_r$. The degeneracy in the transition energy between the energy levels prevents an application of the harmonic resonator as a qubit, since photons at frequency ω_r can also excite higher levels. The situation changes drastically if the linear inductor is exchanged by a Josephson junction (Fig. 2.4(b)) which provides an anharmonic potential energy given by the cosine potential of Eq. 2.20 and an additional contribution to the charging energy by Eq. 2.23. The Hamilton-operator of the total system is then given by:

$$H = 4E_C N^2 - E_J\cos(\varphi) \quad \text{with} \quad E_C = \frac{e^2}{2C_\Sigma} = \frac{e^2}{2(C_J + C)} \tag{2.33}$$

Due to the anharmonic potential the degeneracy of the eigenenergies is lifted and the spacing between energy levels is uneven. For a quantitative calculation see section 2.3.2. The anharmonicity is defined by the frequency difference of the first two quantum levels (here, the energy of the m-th level is denoted as E_m):

$$\alpha = \frac{1}{\hbar}((E_2 - E_1) - (E_1 - E_0)) = \omega_{21} - \omega_{10} \tag{2.34}$$

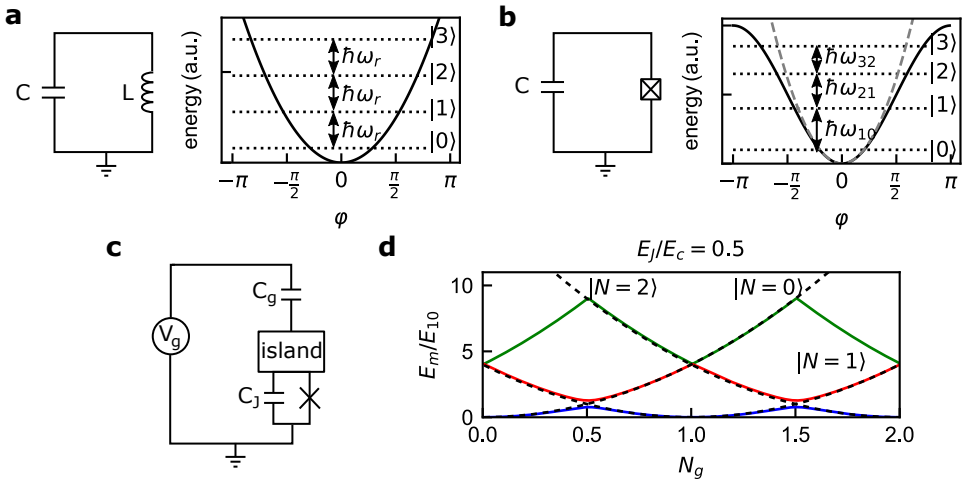

Figure 2.4: (a) Sketch of the harmonic LC-oscillator. Due to its harmonic potential energy with respect to the phase φ its quantum levels are spaced equidistantly by $\hbar\omega_r$. (b) The oscillator becomes anharmonic if the linear inductance is replaced by a Josephson junction and therefore the degeneracy between its transition energies gets lifted. (c) Effective circuit of a charge qubit with additional gate capacitance C_g to control the offset charge N_g on a superconducting island. (d) Charge dispersion of the lowest three energy levels of the charge qubit with respect to the offset charge N_g. Black dashed parabolas correspond to the unperturbed charging energy.

Even though a perfect two-level system would require $\alpha \to \infty$, already in a real system with finite α, two levels can be picked (usually the first two) which serve as a computational space [Kra+19]. When dealing with superconducting qubits it is therefore important to keep in mind that one is not operating a two-level system but in fact an anharmonic multilevel system. Parasitic effects of higher levels come into play by multiphoton-transitions at higher microwave powers [Bra+15] or by utilizing ultra-short pulses to operate the qubits [Kra+19].

The first superconducting qubit realized on this principle was the so called *charge qubit* [Bou+98; NPT99; SSH97]. It is based on the circuit shown in Fig. 2.4(c), which is in close resemblance to the circuit of Fig. 2.2(c), but with an added gate capacitance C_g to control the number of offset charge N_g on a superconducting island. Thus, its Hamiltonian is given by:

$$H = 4E_C(N - N_g)^2 - E_J\cos(\varphi) \quad \text{with} \quad E_C = \frac{e^2}{2C_\Sigma} = \frac{e^2}{2(C_J + C_g)} \tag{2.35}$$

An important hallmark characterizing the dynamics of a quantum circuit is the ratio between the Josephson energy and the charging energy E_J/E_C. The charge qubit is operated in the charge-regime where $E_C > E_J$ and therefore the charge number N is a well defined quantum number. Its energy levels are plotted in Fig. 2.4(d).

Typically, the charge qubit is operated at $N_g = 1/2$, where the energy degeneracy between the $N = 0$ and $N = 1$ state is lifted by the small contribution of the periodic Josephson potential. The exact eigenenergies E_m and wavefunctions $\psi_m(\phi)$ of Eq. 2.35 (Fig. 2.4(d)) can be found by solving the corresponding Schroedinger equation in the phase basis:

$$\left[4E_C(-i\frac{\partial}{\partial\varphi} - N_g)^2 - E_J\cos(\varphi)\right]\psi_m(\varphi) = E_m\psi_m(\varphi) \tag{2.36}$$

As shown in Ref. [Koc+07], Eq. 2.36 can be mapped to Mathieu's differential equation, with the following eigenenergies:

$$E_m(N_g) = E_C a_{2(N_g+k(m,N_g))}\left(\frac{-E_J}{2E_C}\right) \tag{2.37}$$

Here, $a_\nu(x)$ is the Mathieu characteristic value with characteristic exponent ν and $k(m, N_g)$ a sorting function defined in Ref. [Koc+07].

2.3.2 The Transmon Qubit

Despite successful demonstration of coherent quantum oscillations in the charge qubit [NPT99], its coherence times turned out to be insufficient for quantum error correction and other advanced applications in quantum computing [Koc+07]. For charge qubits the main cause of decoherence is charge noise, i.e. fluctuation in the qubits energy splitting due to fluctuations in the charge number on the superconducting island [Sch+08]. In 2007 Koch et al. proposed a new type of qubit called *transmon* (transmission-line shunted plasma oscillation qubit), which operates in a regime of $E_J/E_C \gg 1$ [Koc+07]. This regime can be achieved by adding a shunting capacitance C_s in parallel to the Josephson junction to the circuit of the charge qubit (compare Fig. 2.4(c), Fig. 2.5(a)). The circuit is still described by the same Hamiltonian as the charge qubit (Eq. 2.35), but with a larger total capacitance $C_\Sigma = C_s + C_c$ and a therefore reduced charging energy E_C. The main advantage of the transmon qubit is an exponential suppression of charge noise with E_J/E_C, while the qubits anharmonicity is only reduced by a weak power law with respect to E_J/E_C [Koc+07]. This can be qualitatively understood with the flattening of the charge dispersion of the transmons energy levels with increasing E_J/E_C (compare Fig. 2.5(d)). Since the level spacing of the transmon becomes increasingly harmonic for $E_J/E_C \gg 1$, analytic expressions for the eigenenergies can be obtained with leading-order perturbation theory where the $\cos(\varphi)$ potential in Eq. 2.35 is expanded around $\varphi = 0$ [Koc+07]:

$$H \approx 4E_C N^2 - E_J + \frac{E_J}{2}\varphi^2 - \frac{E_J}{24}\varphi^4 \tag{2.38}$$

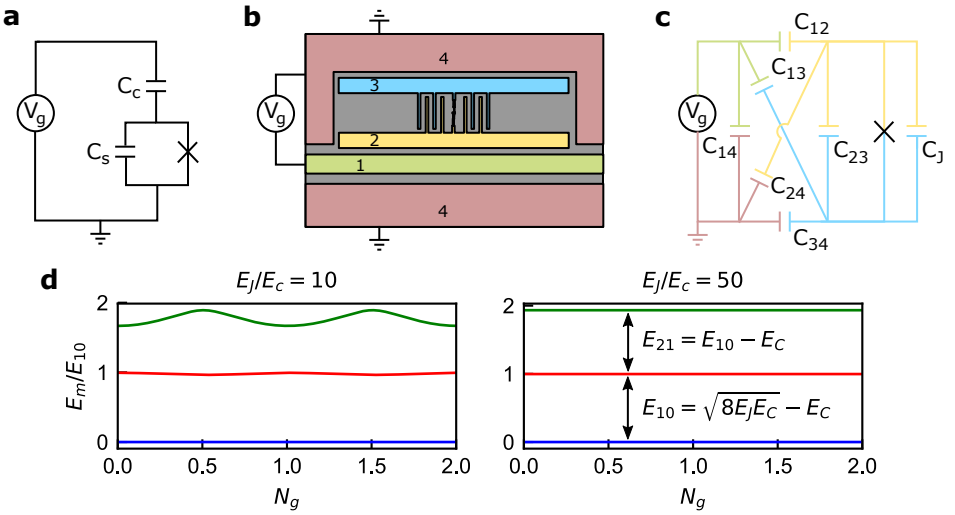

Figure 2.5: (a) Effective transmon circuit with coupling capacitance C_c and shunt capacitance C_s. (b) Sketch of a transmon qubit as realized in the experiment. The transmon (island 2 and 3) is embedded in a ground plane (island 4) and coupled to a waveguide (island 1). (c) Full lumped element circuit model of the transmon qubit. (d) Charge dispersion of the transmon qubit. With increasing E_J/E_C the charge dispersion flattens exponentially, which reduces the impact of charge noise. In the transmon regime $E_J/E_C \gtrsim 50$ the energy levels are almost flat with respect to N_g.

Here, the offset charge N_g was eliminated by a gauge transformation. Re-expressing the Hamiltonian in terms of bosonic creation and annihilation operators ($\varphi = (2E_C/E_J)^{1/4}(a^\dagger + a)$ and $N = i(E_J/(32E_C))^{1/4}(a^\dagger - a)$) yields:

$$H = \sqrt{8E_JE_C}\left(a^\dagger a + \frac{1}{2}\right) - E_J - \frac{E_C}{12}\left(a^\dagger + a\right)^4 \tag{2.39}$$

Thus, in leading order the eigenenergy E_m of the m-th transmon level is given by:

$$E_m = \sqrt{8E_JE_C}m - \frac{E_C}{2}(m^2 + m) + \text{const} \tag{2.40}$$

Using Eq. 2.40 it is straightforward to find the anharmonicity of the transmon qubit: $\alpha = E_{21} - E_{10} = (E_2 - E_1) - (E_1 - E_0) = -E_C$.

In an actual circuit as used in the experiment, the transmon qubit is realized as two interdigitated superconducting islands connected by a Josephson junction (islands 2 and 3 in Fig. 2.5(b)), embedded in a ground plane. Coupling to external circuitry for qubit readout and manipulation is realized via capacitive coupling to superconducting leads (island 1). Its effective capacitance network (Fig. 2.5(c)) can be simplified to the general transmon circuit (Fig. 2.5(a)) with the effective coupling capacitance C_c and the shunting capacitance C_s. In the limit of a large

waveguide capacitance to ground ($C_{14} \to \infty$) and negligible cross capacitances[2] ($C_{24} \approx C_{13} \approx 0$) the expressions simplify to (see appendix B.1):

$$C_c \approx \frac{C_{12}C_{34}}{C_{12} + C_{34}} \tag{2.41}$$

$$C_s \approx C_J + C_{23} \tag{2.42}$$

If a flux-tunable qubit with a SQUID instead of a single junction qubit is used, the transmon Hamiltonian Eq. 2.35 can still be applied, but with an effective Josephson energy $E_{J,\,\mathrm{eff}}(\Phi) = I_{c,\,\mathrm{eff}}(\Phi)\Phi_0/(2\pi)$ and the SQUIDs effective critical current $I_{c,\,\mathrm{eff}}$ from Eq. 2.29 [Koc+07].

2.3.3 Qubit Coupling and Cavity Quantum Electrodynamics

Even though in this work the transmon qubits are coupled to the continuum of electromagnetic modes in a waveguide (giving rise to the field of waveguide quantum electrodynamics, see Sec. 3), the problem of a qubit coupled to the single mode of a resonator should be treated first to understand the coupling of the transmon to external modes in general. From a circuit analysis similar to the one in Sec. 2.3.2, it can be shown that the Hamiltonian of the transmon qubit coupled to a resonator with frequency ω_r via the coupling capacitance C_c is given by [Koc+07]:

$$H = 4E_C(N - N_g)^2 - E_J\cos(\varphi) + \hbar\omega_r b^\dagger b + \frac{2eC_c}{C_\Sigma} N V_{rms}(b + b^\dagger) \tag{2.43}$$

V_{rms} is the rms voltage in the resonator and b, $b^\dagger$ are its bosonic creation and annihilation operators. The last term in Eq. 2.43 is the dipolar-type interaction between qubit and resonator with the dipole operator $\mu = \frac{2eC_c}{C_\Sigma}N$. In the basis of the uncoupled transmon eigenstates $|i\rangle$ Eq. 2.43 reads:

$$H = \hbar\sum_j \omega_j |j\rangle\langle j| + \hbar\omega_r b^\dagger b + \hbar\sum_{i,j} g_{ij} |i\rangle\langle j| (b + b^\dagger) \tag{2.44}$$

The matrix elements of the coupling strength g_{ij} are given by:

$$g_{ij} = \frac{\mu_{ij}}{\hbar} V_{rms} \quad \text{with} \quad \mu_{ij} = \frac{2eC_c}{C_\Sigma} \langle i|N|j\rangle \tag{2.45}$$

[2] For the transmon geometries used in this work numerical simulations of the capacitances indicate that both approximations are fulfilled.

For the transmon, the expectation values of the charge operator N can be calculated analytically within the perturbative treatment in Sec. 2.3.2 to:

$$|\langle j+1|N|j\rangle| \approx \sqrt{\frac{j+1}{2}}\left(\frac{E_\mathrm{J}}{8E_\mathrm{C}}\right)^{1/4} \tag{2.46}$$

All other matrix elements can be shown to vanish for large enough ratios of $E_\mathrm{J}/E_\mathrm{C}$ [Koc+07]. The fact that only neighboring transmon states have a large transition matrix element is explained by dipole selection rules based on the parity of the transmon states. If the Hilbert space of Eq. 2.44 is truncated to the first two transmon levels and the rotating wave approximation is applied, the well-known Jaynes-Cummings Hamiltonian is obtained:

$$H = \frac{1}{2}\hbar\omega_{10}\sigma_\mathrm{z} + \hbar\omega_\mathrm{r} b^\dagger b + \hbar g_{10}(b^\dagger\sigma_- + b\sigma_+) \tag{2.47}$$

In most applications for quantum computing coupled qubit-resonator systems in the limit of $\omega_\mathrm{r} - \omega_{10} \gg g_{10}$ are of crucial importance since they shield the qubits from Johnson-Nyquist noise in the microwave lines used for readout and manipulation. At the same time the qubit infers a frequency shift of the resonator in dependence on its quantum state and can therefore be used for readout [Bla+04].

3 Superconducting Waveguide Quantum Electrodynamics

This chapter provides an introduction to waveguide quantum electrodynamics (wQED), where qubits interact with the electromagnetic mode continuum of a waveguide instead of the single mode of a cavity. First, the properties of a single qubit side-coupled to a one dimensional waveguide are addressed, including the well known resonance fluorescence and the Autler-Townes effect, which gives rise to many practical applications in quantum information processing. In the second part of this chapter the collective properties of multiple qubits coupled to a waveguide are examined. It is shown that the waveguide introduces an effective infinite-range interaction between qubits by exchange of real and virtual photons. This results in an ensemble of collective polariton excitations with varying lifetimes. Finally, the optical response of the ensemble is calculated using band structure and transfer matrix methods.

3.1 Single Qubit wQED

Resonance fluorescence, meaning the resonant absorption and remission of an atom of electromagnetic waves into free space, is one of the most fundamental phenomena in quantum optics. The basic principle of this effect at low incident powers, where incoherent scattering can be neglected, is depicted in Fig. 3.1. On resonance, an impinging wave couples to the atom via its electromagnetic dipole-moment, which starts to oscillate. Thereby, electromagnetic waves with a phase shift of π are remitted in all directions [Zum+08]. Due to destructive interference, the transmitted wave is suppressed and partially reflected. It is noted that at higher powers this simple picture of elastic scattering is incomplete since light can then also be scattered incoherently and the Mollow triplet can be observed in the incoherent spectrum [Ast+10a]. In experiments with ^{87}Rb atoms in 3D space a suppression of 10 % in transmission (extinction) was found [Tey+08]. In wQED the dimension of free space is reduced to one, by using waveguides which have only a significant dimension in the direction of propagation compared to the wavelength

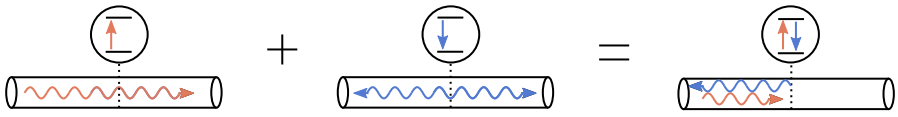

Figure 3.1: Qualitative explanation of the elastically scattered light on a two-level system at low powers. An impinging wave in the open space of a waveguide interferes with the dipole radiation of a qubit, which is phase shifted by π. In the direction of propagation the interference is destructive leading to suppressed transmission and enhanced reflection. Figure inspired by Ref. [Kan18].

λ at the relevant frequencies. On the one hand, the confinement of the modes to one dimension increases the interaction strength with the qubits by reducing the mode volume. On the other hand it enhances interference effects, because it allows for perfect mode matching between the incoming signals and the emitted fields from the qubits [Gu+17]. Beyond resonance fluorescence, wQED systems are particularly suited to study non-linear effects at the single photon level. Due to the intrinsic, strong nonlinearity of the underlying two- or anharmonic multi-level systems, non-classical light, frequency mixing, and amplification can be observed.

Experimentally, superconducting circuits are particularly well suited to study wQED effects because of low-loss waveguides, good coherence times of the qubits, and the absence of parasitic effects like Doppler-broadening in atomic physics. Over the last decade superconducting wQED systems with single qubits were extensively studied experimentally: resonance fluorescence was first demonstrated by Astafiev et al. [Ast+10a] using a flux qubit coupled to a waveguide, followed by demonstrations of time resolved dynamics [Abd+11] and the Autler-Townes effect [Abd+10], as well as other non-linear effects like frequency mixing [Dmi+17; Hön+18] and amplification [Ast+10b]. Similar experiments with transmons [Hoi+13] showed the generation of non-classical light, photon-photon correlations [Hoi+12] and a single photon router [Hoi+11] was implemented.

3.1.1 Two-Level Systems

The Hamiltonian for a two-level system embedded in a waveguide can be derived from its effective lumped element circuit in Fig. 3.2(a) based on a circuit quantization procedure [Lal+13]:

$$H = \frac{1}{2}\hbar\omega_{10}\sigma_z + \hbar\int dk\,\omega_k a_k^\dagger a_k + \hbar\int dk\,g_k(a_k^\dagger\sigma_- + a_k\sigma_+) \tag{3.1}$$

a_k, $a_k^\dagger$ are the bosonic creation and annihilation operators of the waveguide-mode at frequency ω_k and g_k is the coupling strength of the corresponding mode to the qubit. As a next step, the expected elastic scattering properties of the two level

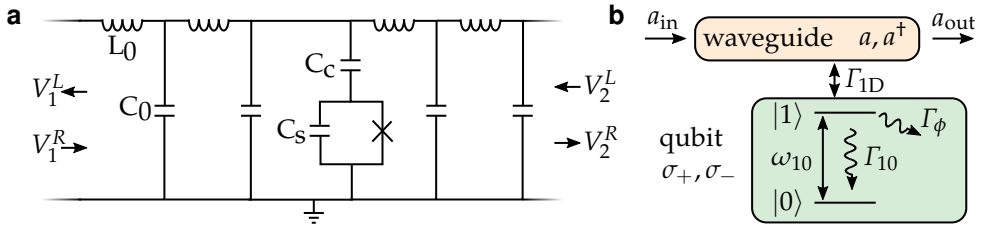

Figure 3.2: (a) Lumped element circuit of a transmon qubit coupled to a waveguide with inductance L_0 and capacitance C_0 per length. $V_{1/2}^{L/R}$ denote in- and outgoing fields in the waveguide. (b) Input-output model of a two-level system coupled to the mode-continuum of a waveguide. First, only the dynamics of the atomic system (green shaded area) are solved and later the photonic degrees of freedom are recovered with the input-output relation of Eq. 3.9.

system based on Eq. 3.1 are calculated. The elastic scattering of light is typically characterized in terms of its scattering matrix (S-Matrix). Experimentally, it is probed by sending coherent microwave states to the qubit through the waveguide and detecting the elastically scattered reflected or transmitted field. For a reciprocal two-port network as shown in Fig. 3.2 the S-Matrix is defined in the following way [Poz11]:

$$\begin{pmatrix} V_1^L \\ V_2^R \end{pmatrix} = \begin{pmatrix} S_{11} & S_{12} \\ S_{21} & S_{22} \end{pmatrix} \begin{pmatrix} V_1^R \\ V_2^L \end{pmatrix} \quad \text{with} \quad S_{11} = S_{22}, \quad S_{12} = S_{21} \tag{3.2}$$

Here, $V_{1/2}^{L/R}$ denote the left- and right propagating fields on the two sides of the waveguide (compare Fig. 3.2(a)). The expected reflection and transmission coefficient ($S_{22}(\omega)$, $S_{21}(\omega)$) are calculated in a two-step process: first, the full problem in Eq. 3.1 is reduced to an individual driven dissipative two-level system. Second, the photonic degrees of freedom of the waveguide are recovered by using input-output theory [GC85] (Fig. 3.2(b)).

The Hamiltonian of a two-level system driven by a classical drive at frequency ω and strength Ω was derived in section 2.1.2:

$$H = -\hbar\frac{\omega - \omega_{10}}{2}\sigma_z + \hbar\frac{\Omega}{2}\sigma_x \tag{3.3}$$

Since the qubit is coupled to a transmission line and other intrinsic loss-channels it is in fact an open quantum system and the Lindblad-Master equation has to be used to calculate the non-unitary dynamics of the system (see section 2.1.3):

$$\dot{\rho}(t) = -\frac{i}{\hbar}[H, \rho] + \Gamma_{10}\mathcal{D}[\sigma_-]\rho + \frac{\Gamma_\phi}{2}\mathcal{D}[\sigma_z]\rho \quad \text{with} \quad \rho = \sum_{i,j=0}^{1} \rho_{ij} |i\rangle \langle j| \tag{3.4}$$

Relaxation with a rate $\Gamma_{10} = \Gamma_{1D} + \Gamma_l$ is included, where Γ_{1D} is the radiative relaxation rate into the waveguide and Γ_l is accounting for all intrinsic non-radiative relaxation processes. Pure dephasing is accounted for with a rate Γ_ϕ. For the sake of simplicity, dissipation due to incoherent pumping of the qubit from thermal activation of the bath is neglected ($\hbar\omega_{10} \gg k_B T$). With the condition $\rho_{11} + \rho_{00} = 1$, Eq. 3.4 can be solved analytically in the steady state ($\dot{\rho} = 0$):

$$\rho_{11} = \frac{\gamma_{10}\Omega^2}{2(\gamma_{10}\Omega^2 + \Gamma_{10}(\gamma_{10}^2 + (\omega - \omega_{10})^2)} \tag{3.5}$$

$$\rho_{10} = \frac{\Gamma_{10}\Omega(-i\gamma_{10} + \omega - \omega_{10})}{2(\gamma_{10}\Omega^2 + \Gamma_{10}(\gamma_{10}^2 + (\omega - \omega_{10})^2)} \tag{3.6}$$

$$\rho_{00} = 1 - \rho_{11} \tag{3.7}$$

$$\rho_{01} = \rho_{10}^* \tag{3.8}$$

In the steady state solution above, the decoherence rate $\gamma_{10} = \frac{\Gamma_{10}}{2} + \Gamma_\phi$ is introduced. Furthermore, it makes sense to define an intrinsic decoherence rate $\Gamma_{nr} = \frac{\Gamma_l}{2} + \Gamma_\phi$ to account for all intrinsic decoherence channels, such that $\gamma_{10} = \frac{\Gamma_{1D}}{2} + \Gamma_{nr}$. For the relation between the Rabi-strength Ω and the actual microwave power P driving the qubit, see section 5.3.2.

After having solved the steady state properties of the driven dissipative qubit, the scattering problem of a photon field in the waveguide on the qubit can be addressed. From input-output theory it can be shown that ingoing and outgoing photon fields (a_{in}, a_{out}) are related via [FKS10]:

$$\langle a_{out} \rangle = \langle a_{in} \rangle - i\sqrt{\frac{\Gamma_{1D}}{2}} \langle \sigma_- \rangle \quad \text{with} \quad \langle \sigma_- \rangle = \mathrm{Tr}(\rho\sigma_-) \tag{3.9}$$

The input field $\langle a_{in} \rangle$ is related with the drive strength Ω by [Mir+19]:

$$\langle a_{in} \rangle = \frac{\Omega}{\sqrt{2\Gamma_{1D}}} \tag{3.10}$$

The transmission and reflection coefficient is given by:

$$S_{21}(\omega) = \frac{\langle a_{out} \rangle}{\langle a_{in} \rangle} = 1 - \frac{\Gamma_{1D}}{2\gamma_{10}} \frac{1 + i\frac{\omega - \omega_{10}}{\gamma_{10}}}{1 + (\frac{\omega - \omega_{10}}{\gamma_{10}})^2 + \frac{\Omega^2}{(\Gamma_{1D} + \Gamma_l)\gamma_{10}}} \tag{3.11}$$

$$S_{22} = S_{21} - 1 \tag{3.12}$$

It is worth noting that $S_{22}(\omega) \propto \chi(\omega)$ (see Appendix B.4), where χ is the linear electric susceptibility of the qubit. Accordingly, $\Re(\chi)$ is a measure for dispersion and $\Im(\chi)$ for absorption.

Until now, the relaxation rate Γ_{1D} of the $1 \rightarrow 0$-transition of the qubit into the waveguide was introduced purely phenomenologically. It can be related to the circuit parameters by modeling the relaxation of the qubit due to Johnson-Nyquist noise in the waveguide with spectral density $S_V^{JN}(\omega)$ [Mar+03]:

$$S_V^{JN}(\omega) = 2\hbar\omega \coth\left(\frac{\hbar\omega}{2k_B T}\right)\Re(Z_0) \tag{3.13}$$

Here, $Z_0 = 50\,\Omega$ is the impedance of the waveguide. The relaxation rate of the qubit is then given by Fermis golden rule [Kra+19]:

$$\Gamma_{1D} = \frac{1}{\hbar^2}\left|\langle 0|\frac{\partial H}{\partial V}|1\rangle\right|^2 S_V^{JN}(\omega_{10}) \tag{3.14}$$

The relevant part of the Hamiltonian which couples to the voltage noise of the waveguide is contained in Eq. 2.44. In agreement with [Hoi13; Loo14], evaluating these expressions in the limit of $\hbar\omega_{10} \gg k_B T$ yields:

$$\Gamma_{1D} = \frac{\mu_{10}^2 \omega_{10} Z_0}{\hbar} \approx \frac{C_c^2 \omega_{10}^2 Z_0}{2C_\Sigma} \tag{3.15}$$

It is noted that relaxation rates Γ_{jD} of the higher $j \rightarrow j-1$-level transition of the transmon into the waveguide scale due to Eq. 2.46 like:

$$\Gamma_{jD} \approx j\Gamma_{1D} \tag{3.16}$$

The calculated transmission coefficient S_{21} of Eq. 3.11 is plotted in Fig. 3.3(a), (b) for the ideal case of vanishing non-radiative decoherence $\Gamma_{nr} = 0$. For low power P of the incoming photon field (i.e. well below the single photon regime, which is defined here as $P = \hbar\omega_{10}\Gamma_{1D}$), transmission is perfectly suppressed (full extinction) on resonance with the qubit. Simultaneously, the corresponding reflection coefficient $|S_{22}|$ is unity, which means the qubit acts as a perfect mirror. If the power is increased beyond the single photon limit, the transmission at resonance gradually approaches unity. This due to the fact that the qubit cannot scatter more than one photon back per average lifetime given by $1/\Gamma_{1D}$, which is an intrinsic signature of the qubits non-linearity (compare Fig. 3.3(b), (d)). If the qubit is subject to internal decoherence $\Gamma_{nr} \neq 0$, the extinction is imperfect, even for low power (compare Fig. 3.3(c)), since the qubit is not coherently remitting all light back into the waveguide. A quantitative measure for the extinction is the extinction coefficient which is defined as $1 - (\Gamma_{nr}/\gamma_{10})^2$ [Ast+10a]. It captures the probability resonant photon absorption and remission by the qubit. A similar measure, which is prevalently used in atomic physics, is the Purcell factor, given by the ratio Γ_{1D}/Γ_{l} of radiative and non-radiative relaxation rates [Fan17]. In previous experiments

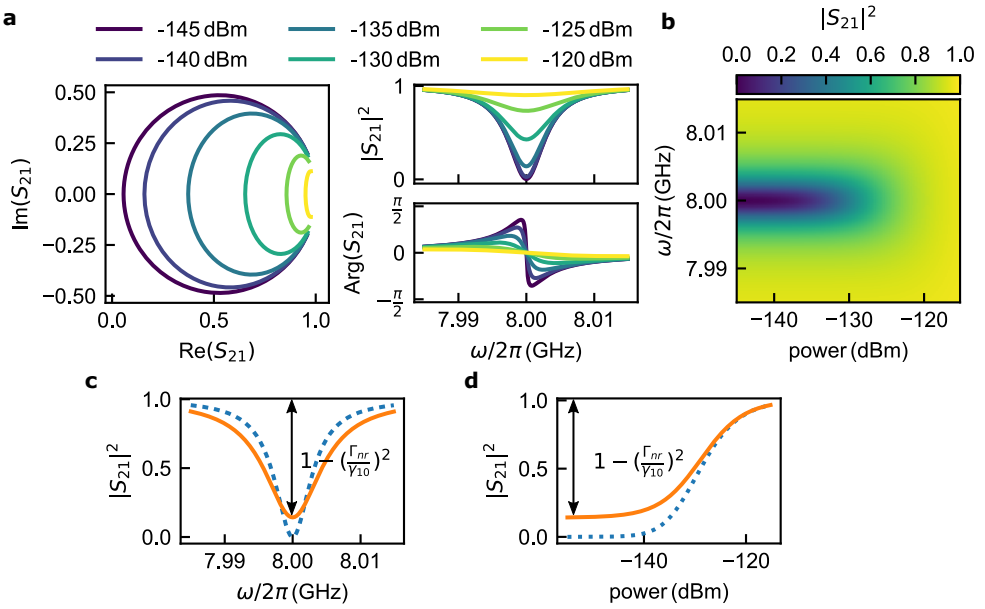

Figure 3.3: Complex transmission coefficient $S_{21}(\omega)$ of a two-level system side-coupled to a waveguide. (a) $S_{21}(\omega)$ as function of frequency and power P of a microwave probe tone, in the case of perfect qubit coherence ($\gamma_{10}/2\pi = \Gamma_{1D}/2/2\pi = 3.2\,\mathrm{MHz}$). At resonance with the qubit and for low power, transmission is completely suppressed and the qubit acts as a perfect mirror. At higher drive power the qubit gets saturated and the transmission increases to unity for full saturation. (b) Saturation of the qubit with increasing power. (c) Comparison of absolute transmission $|S_{21}|^2$ at low power for perfect qubit coherence (blue dotted) and the realistic case of non-vanishing intrinsic decoherence $\Gamma_{\mathrm{nr}}/(2\pi) = 1.9\,\mathrm{MHz}$ (orange). (d) Saturation of resonant absolute transmission coefficient $|S_{21}(\omega_{10})|^2$ with power.

extinction coefficients between 94 % [Ast+10a] and 99.9 % [Mir+19] were achieved with superconducting qubits.

Another interesting property of the derived transmission and reflection coefficients of Eq. 3.11 is that generally $|S_{22}|^2 + |S_{21}|^2 < 1$, even in the limit of vanishing non-radiative decoherence $\Gamma_{\mathrm{nr}} = 0$. The reason for this counter intuitive behavior is, that S_{22} and S_{21} only account for *coherently* and *elastically* scattered light. It can be shown that at increased microwave power beyond the single photon regime light is inelastically and incoherently scattered at the qubit [Ast+10a]. This is caused by the Mollow-triplet which is created by sideband transitions in the hybridized qubit-microwave drive system [Mol69].

In the limit of weak driving, far below the single photon regime, the transmission and reflection coefficient of the qubit (Eq. 3.11) reduce to those of a harmonic oscillator coupled in a so-called *notch-type* configuration to a waveguide [Pro+15;

Kha+12]. Intuitively, the analogy between strongly anharmonic qubits and harmonic systems in the low power limit becomes clear, when considering that the systems are almost exclusively in their ground state such that $\rho_{00} \approx 1$. This implies that a photon will never impinge on a qubit or resonator in the first excited state. Consequently, higher levels beyond the first excited state and non-linear effects can be neglected in the scattering properties [WR20]. In this case, quality factors, typically used for the characterization of resonators, can be associated with the relaxation and decoherence rates:

$$Q_\mathrm{c} = \frac{\omega_{10}}{\Gamma_\mathrm{1D}} \quad Q_\mathrm{l} = \frac{\omega_{10}}{2\gamma_{10}} \quad Q_\mathrm{i} = \frac{\omega_{10}}{2\Gamma_\mathrm{nr}} \tag{3.17}$$

The fact that both, harmonic systems and qubits, show a suppression of transmission in the low power regime implies that the additional observation of non-linear effects is necessary to discriminate them. Besides non-linear saturation with power, the Autler-Townes effect is a hallmark non-linear effect, which will be treated in the next section.

3.1.2 Three-Level Systems

As pointed out in Sec. 2.3.2 the transmon qubits employed in this work are not perfect two-level systems, but in fact anharmonic multilevel systems. As will be discussed below, it is particularly interesting to study the properties of a three-level system coupled to a waveguide which is subject to two microwave tones (compare Fig. 3.4): a weak microwave probe tone (at frequency ω_p and strength Ω_p) is probing the reflection and transmission of the system around the $0 \rightarrow 1$-transition. A second control (ω_c, Ω_c) drives the $1 \rightarrow 2$-transition. The reflection and transmission coefficient are calculated in analog to the two-level case. First, the Lindblad master equation is solved and afterwards the photonic degrees of freedom of the probe fields are extracted using input-output theory. The Hamiltonian of a three-level system in the presence of the two microwave tones in the doubly-rotating frame of both drives is given by (see Appendix B.2):

$$\begin{aligned} H/\hbar &\approx (\omega_{10} - \omega_\mathrm{p})\sigma_{11} + (\omega_{10} - \omega_\mathrm{p} + \omega_{21} - \omega_\mathrm{c})\sigma_{22} \\ &+ \frac{\Omega_\mathrm{p}}{2}(\sigma_{01} + \sigma_{10}) + \frac{\Omega_\mathrm{c}}{2}(\sigma_{12} + \sigma_{21}) \end{aligned} \tag{3.18}$$

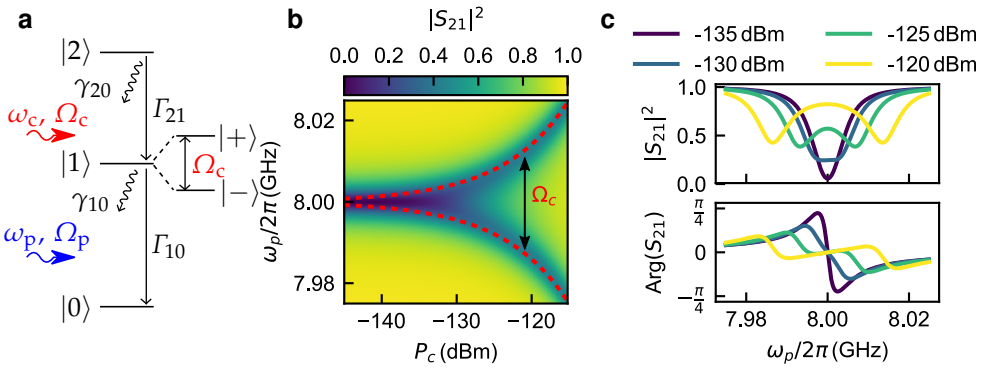

Figure 3.4: (a) Schematic of the ladder-type first three energy levels of the transmon and corresponding relaxation and decoherence rates. The system is subject to two microwave tones: a weak microwave probe tone and a stronger control tone driving the $1 \rightarrow 2$-transition. (b) Calculated Autler-Townes effect for varying control tone power P_c and $\omega_c = \omega_{21}$. For large control power, the region of the $0 \rightarrow 1$-transition is completely transparent. (c) Amplitude and phase of the transmission coefficient for different drive strengths. Used parameters: $\omega_{10}/2\pi = 8\,\mathrm{GHz}$, $\Gamma_{nr} = 0$, $\Gamma_{1D}/2\pi = 6.4\,\mathrm{MHz}$, $\gamma_{20} = \Gamma_{1D}$

Here, a generalized version of the Pauli-matrices with $\sigma_{ij} = |i\rangle\langle j|$, $i, j \in \{0, 1, 2\}$ is used. The three-level version of the Lindblad master equation reads [Abd+10]:

$$\begin{aligned} \dot{\rho}(t) &= -\frac{i}{\hbar}[H, \rho] + \Gamma_{21}\rho_{22}(\sigma_{11} - \sigma_{22}) + \Gamma_{10}\rho_{11}(\sigma_{00} - \sigma_{11}) \\ &+ \Gamma_{20}\rho_{22}(\sigma_{00} - \sigma_{22}) - \sum_{i \neq j}^{2} \gamma_{ij}\rho_{ij}\sigma_{ij} \quad \text{with} \quad \rho = \sum_{i,j=0}^{2} \rho_{ij}\,|i\rangle\langle j| \end{aligned} \tag{3.19}$$

Γ_{ij} with $i > j$ are the relaxation rates of the $i \rightarrow j$-transition. In addition $\Gamma_{ij} = 0$ for all $i < j$ since $\hbar\omega_{ij} \gg k_B T$ is assumed, which would correspond to thermal activation. Furthermore $\Gamma_{20} \approx 0$ is assumed, since the $2 \rightarrow 0$-transition is dipole forbidden (see Sec. 2.3.3) and in this work the relaxation rate is strongly dominated by radiative emission into the waveguide. γ_{ij} are phenomenologically introduced decoherence rates as off-diagonal elements in the dissipator. Full expressions for the rates γ_{ij} in terms of the pure dephasing rates Γ_ϕ^{ij} and relaxation rates are derived in Appendix B.3. An analytical solution to Eq. 3.19 can be found in the limit of a

weak probe tone $\Omega_\mathrm{p} \ll \Omega_\mathrm{c}$ [Gea+95; Hoi13]. In the steady state the off-diagonal elements of Eq. 3.19 read:

$$0 = \dot{\rho}_{10}(t) = -\frac{i}{2}(-2\delta\omega_\mathrm{p}\rho_{10} + \Omega_\mathrm{c}\rho_{20} + \Omega_\mathrm{p}(\rho_{00} - \rho_{11})) - \gamma_{10}\rho_{10} \tag{3.20}$$

$$0 = \dot{\rho}_{20}(t) = -\frac{i}{2}(-2(\delta\omega_\mathrm{p} + \delta\omega_\mathrm{c})\rho_{20} + \Omega_\mathrm{c}\rho_{10} - \Omega_\mathrm{p}\rho_{21}) - \gamma_{20}\rho_{20} \tag{3.21}$$

$$0 = \dot{\rho}_{21}(t) = -\frac{i}{2}(-2\delta\omega_\mathrm{c}\rho_{21} - \Omega_\mathrm{p}\rho_{20} + \Omega_\mathrm{c}(\rho_{11} - \rho_{22})) - \gamma_{21}\rho_{21} \tag{3.22}$$

$$\delta\omega_\mathrm{c} = \omega_\mathrm{c} - \omega_{21} \qquad \delta\omega_\mathrm{p} = \omega_\mathrm{p} - \omega_{10} \tag{3.23}$$

In the limit of $\Omega_\mathrm{p} \ll \Omega_\mathrm{c}$, Eq. 3.21 simplifies to:

$$\rho_{20} \approx -\frac{i\Omega_\mathrm{c}}{2(\gamma_{20} - i(\delta\omega_\mathrm{p} + \delta\omega_\mathrm{c}))}\rho_{10} \tag{3.24}$$

Inserting this result in Eq. 3.20 and assuming that higher qubit levels are not saturated ($\rho_{22} = \rho_{11} \approx 0$, $\rho_{00} \approx 1$) by the weak probe tone yields:

$$\rho_{10} = -\frac{i\Omega_\mathrm{p}}{-2i\delta\omega_\mathrm{p} + 2\gamma_{10} + \frac{\Omega_\mathrm{c}^2}{2(\gamma_{20} - i(\delta\omega_\mathrm{p} + \delta\omega_\mathrm{c}))}} \tag{3.25}$$

Finally the transmission and reflection coefficient are calculated by utilizing the input-output equations (Eqs. 3.9, 3.10) and $\mathrm{Tr}(\rho\sigma_{01}) = \rho_{10}$:

$$S_{21}(\omega_\mathrm{p}) = 1 - \frac{\Gamma_\mathrm{1D}}{2\gamma_{10}}\frac{1}{1 - i\frac{\omega_\mathrm{p} - \omega_{10}}{\gamma_{10}} + \frac{\Omega_\mathrm{c}^2}{4\gamma_{10}(\gamma_{20} - i(\omega_\mathrm{p} - \omega_{10} + \omega_\mathrm{c} - \omega_{21}))}} \tag{3.26}$$

$$S_{22} = S_{21} - 1 \tag{3.27}$$

In the limit of a vanishing control tone Ω_c and weak probe tone strength Ω_p, Eq. 3.26 reduces to the transmission of a two-level system (Eq. 3.11).

The calculated transmission coefficient of Eq. 3.26 is plotted in Fig. 3.4(b), (c). Whereas for low control power transmission is strongly suppressed around ω_{10}, at a larger power a window of high transmission opens up which is enclosed by two new resonances. The splitting between these resonances is called Autler-Townes splitting (ATS) [AT55]. The ATS is a type of dynamic ac-Stark effect. This implies the strong resonant control tone hybridizes with the first qubit level, which splits up into two new non-degenerate eigenstates $|+\rangle$ and $|-\rangle$. For $\Omega_\mathrm{p} \ll \Omega_\mathrm{c}$, $\omega_\mathrm{p} = \omega_{10}$, and $\omega_\mathrm{c} = \omega_{21}$ diagonalization of Eq. 3.18 yields:

$$|\pm\rangle = \frac{1}{\sqrt{2}}(|1\rangle \pm |2\rangle) \quad \text{with} \quad \omega_\pm = \pm\frac{\Omega_\mathrm{c}}{2} \tag{3.28}$$

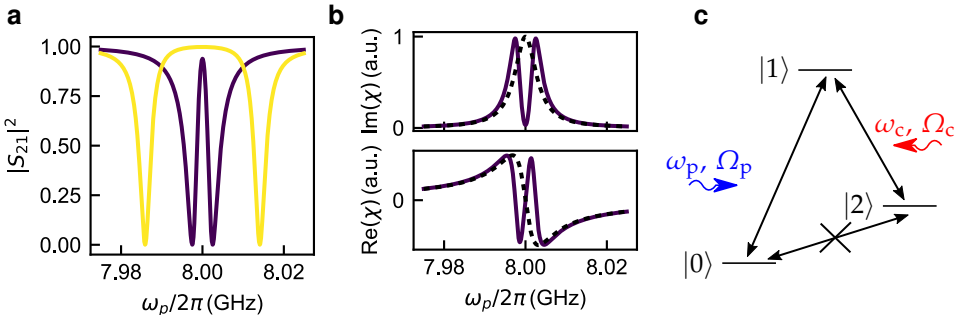

Figure 3.5: (a) Amplitude of the transmission coefficient $|S_{21}|^2$ under the ideal condition of $\gamma_{20} = 0.01\Gamma_{1D}$ and two different control powers P_c (color scale and other parameters are the same as in Fig. 3.4). The narrow transparency window for $\Omega_c < \Gamma_{1D}$ (purple line) is the signature of EIT. (b) Under EIT conditions the system features vanishing absorption $\Im(\chi)$ but simultaneously large dispersion $\Re(\chi)$ around ω_{10}, whereas in the absence of a control tone the absorption is maximal and a strong anomalous dispersion is present (black dashed line). (c) Schematic of a Λ-type three-level system with the $0 \to 2$-transition being dipole-forbidden. It is the only type of three-level system which can feature perfect EIT.

Therefore, in agreement with the calculated transmission in Fig. 3.4, the splitting between the new eigenstates is exactly given by Ω_c. A practical application of the ATS was demonstrated by Hoi et al. with a superconducting transmon qubit coupled to a waveguide [Hoi+11]. By switching the control tone between on- and off-state, the transmission around ω_{10} can be switched between transparent and fully reflecting. Therefore, the qubit acts as a photon router or switch in the single photon regime. Figure 3.5(a) shows the ATS for small $\gamma_{20} \ll \Gamma_{1D}$. In contrast to the case in Fig. 3.4, the transparency window remains intact with $|S_{21}(\omega_{10})| \approx 1$, even for small control tone strengths $\Omega_c < \Gamma_{1D}$. In this limit the transparency is created by a destructive quantum interference by two excitation pathways ($0 \to 1$ and $0 \to 1 \to 2 \to 1$) in the driven three-level system [FIM05]. This effect is called electromagnetically induced transparency (EIT). The interference between the two excitation paths is only perfect if $\gamma_{20} = 0$, since any finite $2 \to 0$-decoherence rate would reduce the contribution of the $0 \to 1 \to 2 \to 1$ path. Therefore, in ladder type three-level systems perfect EIT with $\gamma_{20} \approx 0$ can not be realized since in these systems always $\gamma_{20} > \Gamma_{2D}/2$ (or specifically for the transmon $\gamma_{20} > \Gamma_{1D}$) holds [YRZ01] (see Appendix B.3). It can only be observed in Λ-type three-level systems, where the third level with a dipole-forbidden transition to the first level is energetically lower than the second level (compare Fig. 3.5(c)). While two-level systems (or three-level systems in the absence of a control tone) feature a maximum of the absorption coefficient and strong anomalous dispersion around the resonance, the appealing feature of an EIT system is, that it features both, strong dispersion and low absorption around the atomic resonance (Fig. 3.5(b)). For

effective media made of an ensemble of three-level systems under EIT conditions, the large dispersion manifests itself to measurable group delays of propagating light pulses. This can be exploited in experiments with slow light and quantum memories which are discussed in detail in Sec. 3.2.4.

Even though ATS and EIT are closely related phenomena, they are distinct effects whose discrimination is part of current research [Abi10; ADS11; Hao+18]. Throughout this work, the convention of Refs. [Abi10; Hao+18; ADS11] is used, where $\Omega_c \gtrsim \Gamma_{1D}$ is considered as ATS-regime. In the regime $\Omega_c \lesssim \Gamma_{1D}$, EIT due to quantum interference is possible. This means an interference between dressed states can only happen if their splitting is smaller than their linewidth (see Fig. 3.5(a)). However, depending on the strength of the $2 \to 0$ decoherence, ATS can still be the dominating effect in this regime and an information theoretic quantitative analysis based on AIC (Akaike's information criterion) has to be used to discriminate the two effects [ADS11].

3.2 Multi-Qubit wQED

Coupling more than one qubit to the same waveguide changes the physical situation drastically, since now multiple scattering and interference between waveguide photons can occur. As will be more rigorously shown below, the mutual exchange of photons leads to an effective infinite range interaction between the qubits giving rise to collective excitations. Due to correlated decay, these excitations have radiative relaxation rates which range from orders of magnitude smaller (*subradiant*) to larger (*superradiant*) than the ones from the individual qubits [Alb+19]. A direct consequence of the strong non-linear response of the qubits combined with the inter-qubit scattering is that transmitted and reflected light is predicted to show time dependent quantum correlations [FZB14]. Although multi-qubit wQED Systems are expected to have numerous applications in the field of quantum optics and quantum computing (see Ch. 1), they have been to the date of this work barely studied with superconducting qubits: a first study demonstrated the photon-mediated qubit-qubit coupling of two transmon qubits via a common waveguide [Loo+13], followed by the demonstration of an artificial atomic-cavity using a wQED system of aperiodically spaced qubits [Mir+19] and the creation of entangled light in a three qubit system [Kan+20].

3.2.1 Effective wQED Hamiltonian

The Hamiltonian of N qubits coupled to a one-dimensional bi-directional waveguide with symmetric coupling reads [Can+15]:

$$H = \frac{1}{2}\hbar \sum_{j=1}^{N} \omega_{10}^{j} \sigma_z^j + \hbar \sum_{\nu=\pm} \int dk\, \omega_k a_{k,\nu}^{\dagger} a_{k,\nu} + \hbar \sum_{\nu=\pm} \sum_{j=1}^{N} \int dk\, g_k (a_{k,\nu}^{\dagger} \sigma_-^j \exp(i\nu k d j) + h.c.) \quad (3.29)$$

Here $a_{k,\nu}^{\dagger}$, $a_{k,\nu}$ are bosonic creation and annihilation operators of the waveguide mode with wavenumber k and ν for the left and right propagation direction. The waveguide dispersion is assumed to be linear with $\omega_k \approx ck$. The last term in Eq. 3.29 describes the dipole type interaction between qubits and waveguide modes in the rotating wave approximation with coupling strength g_k. Note, that the coupling term includes a phase factor $\exp(i\nu k d j)$ which accounts for the phase between the qubits when they are placed at finite distance d from each other. Similar to the single-qubit case of Sec. 3.1.1, solving the full problem of Eq. 3.29 can be facilitated by formally integrating out the waveguide degrees of freedom, solving the master equation for the atomic part of the effective Hamiltonian which then only depends on the qubit operators and input field, and later recover the photonic degrees of freedom with input-output theory. This formal integration is carried out in Refs. [Can+15; Lal+13], and here only the relevant results are presented. The effective qubit Hamiltonian (without the driving term due to the input field a_{in}) reads:

$$H_{\text{eff}} = \hbar \sum_{j=1}^{N} \omega_{10}^{j} b_j^{\dagger} b_j + \frac{\alpha}{2} b_j^{\dagger} b_j^{\dagger} b_j b_j - i\hbar \frac{\Gamma_{1D}}{2} \sum_{j \neq l}^{N} \exp\left(i\omega_{10} d|j-l|/c\right) b_j^{\dagger} b_l \quad (3.30)$$

For this result the effective radiative relaxation rate $\Gamma_{1D} = 4\pi g^2/c$ was introduced and the Markov approximation was applied [Can+15]. Moreover, instead of Pauli operators the bosonic operators $b_j^{\dagger}$, b_j were introduced to describe the qubits. In order to prevent multiple excitation of the same qubit an interaction energy was introduced. The case of ideal two-level systems can be recovered in the limit $\alpha \to \infty$. Within the Markov approximation, ω_{10} is an average of all ω_{10}^{j}, around which the atomic dynamic is centered. The corresponding input-output relations are given by [Can+15]:

$$a_{\nu,\text{out}}(z,t) = a_{\nu,\text{in}}(t - \nu z/c) - i\sqrt{\frac{\Gamma_{1D} c}{2}} \sum_{j=1}^{N} b_j \exp(i\nu\omega_{\text{in}}(z - jd)/c) \quad (3.31)$$

The second term in Eq. 3.30 is the signature of an effective qubit-qubit coupling, which is of infinite range. Furthermore, the interaction is complex, making H_{eff} non-hermitian. The real-part ($\propto \sin(\omega_{10} d|j-l|/c)$) describes an exchange type

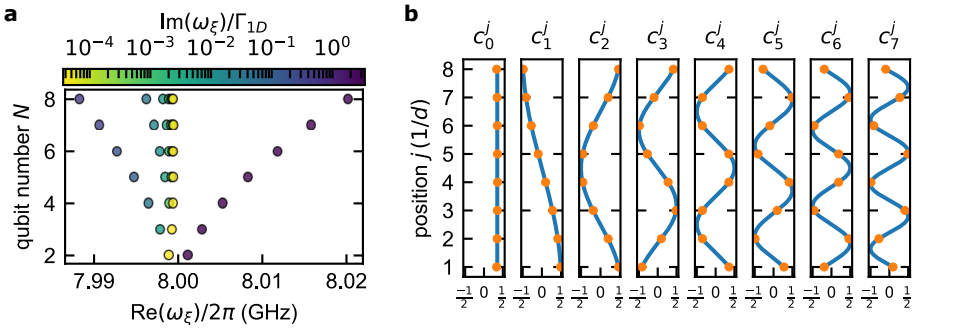

Figure 3.6: (a) Calculated eigenvalues based on Eq. 3.30 in the single-excitation manifold in dependence on the number of qubits N. Each eigenmode represents a polariton with radiative relaxation rate $\Gamma_\xi = 2\Im(\omega_\xi)$ and frequency $\Re(\omega_\xi)$. With increasing N, a band gap emerges between ω_{10} and the superradiant mode. (b) Coefficients c_ξ^j of the polariton wave-function for $N = 8$ obtained from the eigenvectors of Eq. 3.30 (orange points) and their analytic approximation of Eq. 3.32 (blue lines). Each polariton corresponds to a delocalized standing wave. Used parameters: $\omega_{10} = 8\,\mathrm{GHz}$, $d = 400\,\mu\mathrm{m}$, $\Gamma_{1D}/2\pi = 12.7\,\mathrm{MHz}$.

qubit-qubit coupling, while the imaginary part ($\propto \cos(\omega_{10} d|j-l|/c)$) describes cooperative emission into the waveguide [Lal+13]. Due to the periodic dependence of the interaction on the qubit separation ($d|j-l|$) a pure exchange type (dissipative) interaction is achieved for separations of $d|j-l|\omega_{10}/(c2\pi) = (2n+1)/4$ ($= n/2$). Whereas the exchange type interaction gives rise to a measurable frequency shift due to exchange of virtual photons, the dissipative interaction alters the dissipation rate by exchange of real photons [Loo+13]. This dependence of the interaction on inter-qubit distance was experimentally first shown in Ref. [Loo+13], using two transmon qubits coupled to a waveguide.

3.2.2 Eigenmode Analysis and Properties

Diagonalizing H_{eff} in Eq. 3.30 in the single excitation sector ($\alpha \to 0$) gives access to its N eigenvalues ω_ξ[1] and eigenvectors $|\psi_\xi\rangle = \sum_{j=1}^{N} c_\xi^j |1_j\rangle$, where $|1_j\rangle = b_j^\dagger |0\rangle^{\otimes N}$ is the excited state of the j-th qubit. Each eigenstate corresponds to a polariton formed by a collective excitation of the qubit chain [Ivc05]. Since the H_{eff} is non-hermitian, the obtained frequencies ω_ξ are complex, with their real part corresponding to the frequency of the associated polariton. The imaginary part of ω_ξ is proportional to the radiative polariton relaxation rate ($\Im(\omega_\xi) = \Gamma_\xi/2$). The distribution of the

[1] Here, the convention is used that the eigenvalues $\omega_0 ... \omega_{N-1}$ are sorted from brightest to darkest, meaning by decreasing $\Im(\omega_\xi)$

eigenvalues over the complex plane is strongly dependent on the qubit separation d. For the trivial case of $d \approx 0$, the interaction term of Eq. 3.30 is purely dissipative and its N eigenstates are degenerate with the bare qubit frequency ω_{10}. Furthermore $N-1$ eigenstates have a vanishing imaginary part and are therefore non-radiative and are thus referred to as *dark* or *subradiant states*. One mode however retains a finite line-width of $2\Im(\omega_\xi) = N\Gamma_{1D}$ and therefore radiates *superradiantly* compared to the individual qubits. The limit $d = 0$ thus reproduces the well known result of superradiance in the Dicke-Model, where all emitters radiate coherently into the same continuum [Alb+19; Dic54]. If $d > 0$, the degeneracy between the eigenstates is lifted and a non-degenerate polariton spectrum is obtained (compare Fig. 3.6(a)). Here, the relaxation rates range from strongly sub-radiant ($\Gamma_\xi < \Gamma_{1D}$) to superradiant ($\Gamma_\xi > \Gamma_{1D}$). With increasing qubit number N the polaritonic modes form two continuous bands, separated by a band gap without any allowed frequencies, which is discussed in detail in Sec. 3.2.3. It can generally be shown, that the radiative relaxation rate Γ_ξ of the most subradiant state fulfills a universal scaling with the qubit number N of $\Gamma_\xi \propto N^{-3}$, which even holds for multi-dimensional systems [TL08; Alb+19; Ase+17]. Analogously, the brightest of the subradiant modes fulfills a complementary scaling of $\Gamma_\xi \propto N^3$ ([Bre+21] and Appendix B.5). The calculated coefficients c^j_ξ of the eigenvector $|\psi_\xi\rangle$ of H_{eff} are shown in Fig. 3.6(b), for $N = 8$ resonant qubits. Apparently, the polariton eigenmodes of the qubit chain in the single excitation sector are delocalized and correspond to standing waves. Although the wavenumber k is only unambiguously defined in the infinite lattice limit [Ase+17], in a finite system the dominant wavenumber can be defined as $k \approx \xi\pi/dN$ and the effective coefficients can be approximated[2] as [Bre+21]:

$$c^j_\xi \approx \sqrt{\frac{2}{N}} \cos\left(\frac{\pi\xi}{Nd} d\left(j+\frac{1}{2}\right)\right) \quad \text{with} \quad \xi = \{1....N-1\}, \quad c^j_0 \approx \sqrt{\frac{1}{N}} \tag{3.32}$$

The mode profiles shown in Fig. 3.6(b) provide a simple explanation for their different radiative relaxation rates Γ_ξ: The larger the overlap η of the mode with the wave driving the system, the brighter it is. η is defined as:

$$\eta = \sum_{j=0}^{N-1} |E(jd) c^j_\xi|^2 \quad \text{with} \quad E(jd) = \sqrt{\frac{1}{N}} \exp(i\omega dj/c) \tag{3.33}$$

3.2.3 Transfer Matrix Approach

Solving the full Lindblad master equation associated with Eq. 3.29 quickly becomes unfeasible for larger numbers of qubits N, since the dimension of the Fock-Louiville

[2] In the relevant limit for this work: $d \ll \lambda$ and $Nd < \lambda$

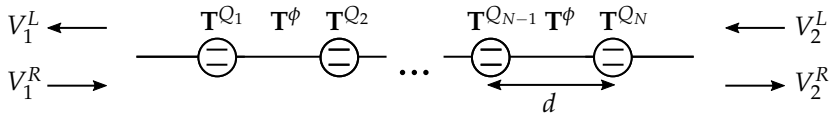

Figure 3.7: Schematic representation of the transfer matrix for a system of N qubits coupled to a waveguide. The inter qubit distance is given by d.

space scales exponentially with $2N$ [Man20]. In the regime of purely elastic scattering at low incident photon powers ($P \ll \hbar\omega_{10}\Gamma_{1D}$), which is here called *linear regime*, the optical response of a linear chain of qubits of almost arbitrary size can be calculated using the transfer matrix (T-matrix). This semi-classical approach is based on the steady state solutions of the Lindblad master equation of the individual qubits (Eqs. 3.11 and 3.26) and incorporates interference effects of light scattered between them. The transfer matrix connects the in- and outgoing fields of a two-port network in the following way [Ase+17]:

$$\begin{pmatrix} V_2^R \\ V_2^L \end{pmatrix} = \mathbf{T} \begin{pmatrix} V_1^R \\ V_1^L \end{pmatrix} \tag{3.34}$$

For a combined network of multiple subsystems in series, the T-matrix has the advantage compared to the S-matrix, that it is multiplicative, i.e. it can be written as the product of transfer matrices. For a system of N qubits coupled to a waveguide, separated by the distance d (compare Fig. 3.7), the total transfer matrix $\mathbf{T}_{\text{tot}}$ reads:

$$\mathbf{T}_{\text{tot}} = \mathbf{T}^{Q_N}\mathbf{T}^{\phi}\mathbf{T}^{Q_{N-1}}...\mathbf{T}^{\phi}\mathbf{T}^{Q_2}\mathbf{T}^{\phi}\mathbf{T}^{Q_1} \tag{3.35}$$

$\mathbf{T}^{Q_n}$ is the transfer matrix of the n-th qubit and is given by [Deu+95]:

$$\mathbf{T}^{Q_n} = \begin{pmatrix} \frac{1+2r}{1+r} & \frac{r}{1+r} \\ -\frac{r}{1+r} & \frac{1}{1+r} \end{pmatrix} \tag{3.36}$$

r denotes the reflection coefficient of a qubit in steady state given by Eq. 3.12 and $\mathbf{T}^{\phi}$ accounts for the propagation along a bare piece of transmission line in between two qubits:

$$\mathbf{T}^{\phi} = \begin{pmatrix} \exp(i\phi) & 0 \\ 0 & \exp(-i\phi) \end{pmatrix} \tag{3.37}$$

Here, the propagating field accumulates a phase of $\phi = kd = \frac{\omega}{c}d$ with length d and phase velocity c. Once the T-matrix is calculated, the transmission coefficient S_{21} and reflection coefficient S_{22}, as measured in the experiment, can be recovered from $\mathbf{T}_{\text{tot}}$ with the following relations (assuming $V_2^L = 0$ for transmission experiment and $V_1^L = 0$ for reflection experiment):

$$\frac{V_2^R}{V_1^R} = \frac{1}{T_{22}^{\text{tot}}} = S_{21} \qquad \text{and} \qquad \frac{V_2^R}{V_2^L} = \frac{T_{12}^{\text{tot}}}{T_{22}^{\text{tot}}} = S_{22} \tag{3.38}$$

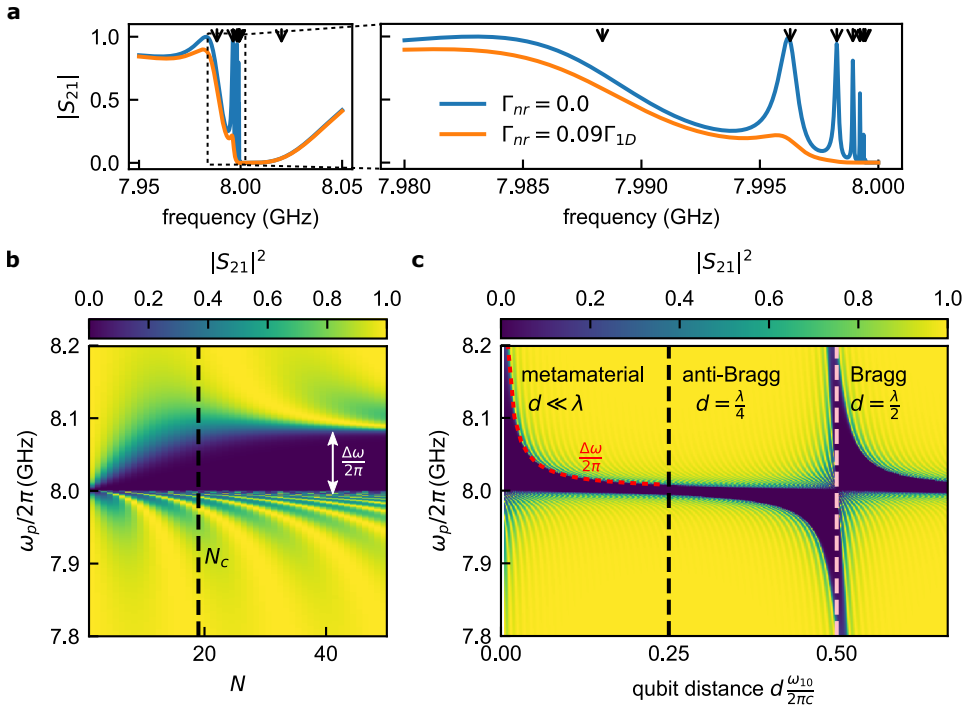

Figure 3.8: (a) Calculated transmission $|S_{21}|$ of 8 qubits coupled to a waveguide. Peaks of unity transmission are produced by Fano interference of polaritonic eigenmodes of the system. Black arrows mark calculated eigenfrequencies $\Re(\omega_\xi)$ from Eq. 3.30. For finite non-radiative qubit decoherence Γ_{nr} the modes are damped and only visible when $\Gamma_\xi/2 > \Gamma_{\mathrm{nr}}$. (b) Dependence of the transmission coefficient on the qubit number N. The width of the band gap saturates at $N_{\mathrm{c}} = 19$ to $\Delta\omega$. (c) Dependence of the transmission coefficient on qubit distance d. $\Delta\omega$ marks the expected width of the band gap, according to Eq. 3.41. Used parameters: $d = 400\,\mu\mathrm{m}$, $\omega_{10} = 8\,\mathrm{GHz}$, $\Gamma_{1\mathrm{D}}/2\pi = 12.7\,\mathrm{MHz}$.

It is easy to see from the definition in Eq. 3.34 that the T-Matrix itself is linear, meaning it has to be independent from the incoming field to retain its multiplicative property. Even though the transmission coefficient S_{21} of Eq. 3.12 can also be used in the non-linear regime of larger probe powers, it is therefore wrong to use this case also in the T-matrix method of several qubits in a linear chain. This would lead to the unphysical situation that all qubits experience the same drive strength Ω, which is, due to multiple scattering in the array, not necessarily the case. It is noted that the T-matrix method is not restricted to one-dimensional qubit chains made of identical qubits with equidistant spacing, but is capable of accounting for arbitrary individual qubit parameters and frequencies.

The calculated transmission coefficient for eight resonant qubits with a spacing of $d = 400\,\mu\text{m}$ is shown in Fig. 3.8(a). The transmission spectrum features several peaks corresponding to the collective polariton modes (see Sec. 3.2.2), where the line shape is created by Fano interference [HFS16; Bre+21; Lep+19]. This interference effect explains why the peaks do not exactly coincide with the calculated real parts of the eigenvalues $\Re(\omega_{\tilde{\xi}})$ of Eq. 3.30. The wide spectral region of suppressed transmission above the common resonance frequency ω_{10} is created by the superradiant mode and the gap between the latter and the subradiant modes. In the realistic case of finite non-radiative damping, only subradiant modes with $\Gamma_{\tilde{\xi}}/2 > \Gamma_{\text{nr}}$ are observable in the transmission spectrum. Excited darker modes decay in the qubits before they can be remitted into the waveguide and are therefore not visible. With the T-Matrix approach at hand, the dependence of the waveguide transmission $|S_{21}|$ on the number N of resonant qubits and their distance d can be further elaborated (see Fig. 3.8(b), (c)). Increasing N does not only increase the number of polariton modes and alters their lifetime (Fig. 3.6(a)), but increases the width of the band gap region until it saturates to a certain width $\Delta\omega$ (Fig. 3.8(b)) at a certain critical number of qubits N_{c}. Here it is phenomenologically found that $N_{\text{c}} \approx \lambda/2/d$. This is most likely due to partial constructive interference between the emitted light of individual qubits, which is only possible if they are not further apart than $\lambda/2$. When the distance d between neighboring qubits is varied between 0 and $\lambda/2$, several different physical regimes are crossed. A spacing comparable or larger than λ is considered as *photonic crystal regime* [SPW04]. The most relevant configurations in this regime are $d = \lambda/4$ ($d = \lambda/2$) or multiples thereof, where the structure behaves as a resonant anti-Bragg (Bragg) structure. The calculated transmission coefficient in Fig. 3.8(c) shows that transmission is indeed strongly enhanced for the anti-Bragg structure (except a narrow band gap of width $\Gamma_{1\text{D}}$ due to the local resonance of the qubits). Whereas for a Bragg structure, it is strongly suppressed in a large spectral region around ω_{10}, due to constructive interference in the direction of reflection. Therefore, qubit chains in the Bragg regime are often called atomic mirrors, which have been investigated in Refs. [Cha+12; Mir+19]. The intuitive explanation for Bragg and anti-Bragg structures is analogue to the either purely dissipative or exchange type interaction of Eq. 3.30. The structures realized in this work are in the limit, where the inter-qubit spacing is substantially smaller than the wavelength ($d \ll \lambda$), which is called the *metamaterial limit*. Due to the dense spacing, some of its features are similar to a Bragg structure, however its band gap appears close to the center of the Brillouin zone instead of at its edges. Moreover, and most importantly, the dense spacing allows for an effective medium description [SPW04].

For an infinite one-dimensional artificial lattice made of equally spaced and identical qubits, the full dispersion relation can be calculated based on the T-Matrix

[Deu+95]. The transfer matrix of a unit cell of such a lattice is given by $\mathbf{T}_\mathrm{U} = \mathbf{T}^\mathrm{Q}\mathbf{T}^\phi$. Since $\det \mathbf{T}_\mathrm{U} = 1$, it has necessarily the eigenvalues $\exp(\pm ikd)$, which is an analog statement to Bloch's theorem. Therefore, calculating the trace of $\mathbf{T}_\mathrm{U}$ yields due to the independence of the trace with respect to the chosen basis:

$$\cos(kd) = \frac{\mathrm{Tr}(\mathbf{T}_\mathrm{U})}{2} = \cos\left(\frac{\omega d}{c}\right) + i\frac{r}{1+r}\sin\left(\frac{\omega d}{c}\right) \tag{3.39}$$

Solving Eq. 3.39 for $\omega(k)$ gives full access to the dispersion relation as shown in Fig. 3.9(a). The discrete polaritonic modes, as discussed above, now form two continuous polariton branches, separated by a band gap. This is due to the significant hybridization of the bare waveguide modes and the qubits, caused by their interaction [Alb+19]. In the *metamaterial limit*, where $d \ll \lambda$, the ensemble of two-level systems behaves like an effective medium characterized by simple optical response functions like the permittivity $\epsilon(\omega)$ [Ivc05]. In this limit Eq. 3.39 simplifies to:

$$1 - \frac{(kd)^2}{2} \approx 1 - \frac{1}{2}\left(\frac{\omega d}{c}\right)^2 + i\frac{r}{1+r}\frac{\omega d}{c} \tag{3.40}$$

Using the reflection coefficient of Eq. 3.12 in the limit of vanishing probe strength Ω, the effective permittivity becomes:

$$\epsilon(\omega) = \left(\frac{ck}{\omega}\right)^2 \approx 1 + \frac{\Delta\omega}{\omega_{10} - \omega - i\Gamma_\mathrm{nr}} \quad \text{with} \quad \Delta\omega = \frac{\Gamma_\mathrm{1D} c}{\omega_{10} d} \tag{3.41}$$

The variable $\Delta\omega$ characterizes the regime, where $\Re(\epsilon)$ is negative and the corresponding refractive index $n = \sqrt{\epsilon}$ is purely imaginary, i.e. the width of the band gap. If instead of Eq. 3.12, the three-level case of Eq. 3.26 is used to calculate the band structure according to Eq. 3.39, it can be seen that it is modified drastically compared to the two-level case (see Fig. 3.9(b)): depending on the strength of the control tone Ω_c, a third band opens up in between the upper and lower polaritonic branches splitting up the band gap into two, both of which are signatures of the collective ATS. This can be understood in the dressed state picture of ATS. Instead of state $|1\rangle$ of the individual qubits, it is now the two dressed states $|\pm\rangle$ giving rise to two independent Bloch bands [WS10]. The collective ATS reveals the appealing property that the band structure of the artificial medium made of three-level qubits can be manipulated actively with the help of an external control parameter Ω_c.

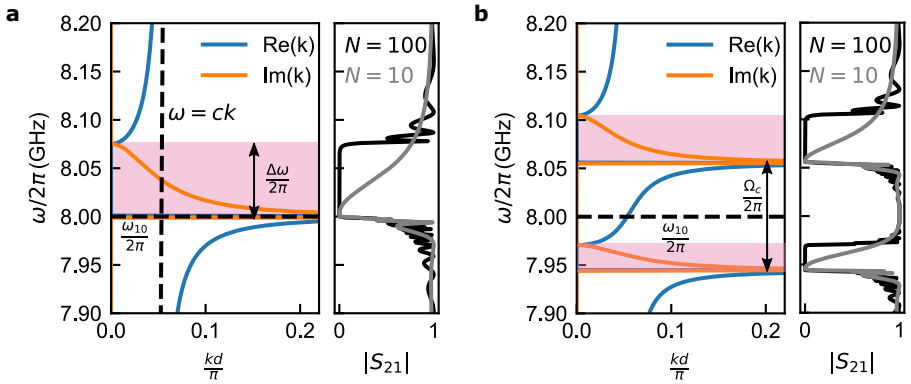

Figure 3.9: (a) Calculated band structure of an infinite chain of two-level systems coupled to a waveguide with dense qubit spacing, in the metamaterial limit ($d = 400\,\mu\text{m}$, $\phi = \omega_{10} d/c \approx 0.17$). The waveguide mode and the qubits at $\omega_{10}/2\pi = 8\,\text{GHz}$ hybridize into two polariton branches, separated by a band gap with width $\Delta\omega = \frac{\Gamma_{1D} c}{\omega_{10} d}$. The corresponding absolute transmission for $N = 100$ and $N = 10$ show strong suppression in the band gap region. (b) Band structure for the same chain of qubits under the conditions of the ATS with control strength $\Omega_c/2\pi = 111\,\text{MHz}$. Due to the presence of the dressed states of the ATS, a third central band with allowed transmission around ω_{10} emerges, sandwiched between two band gaps. Qubit coherence parameters for the numerical model: $\Gamma_{1D}/2\pi = \gamma_{10}/\pi = 12.7\,\text{MHz}$, $\gamma_{20} \approx 0\,\text{MHz}$.

3.2.4 Slow Light and Quantum Memories

A consequence of the quasi-flat central band around ω_{10} for an ensemble of qubits under EIT/ATS condition (compare Fig. 3.10) is the associated low group velocity v_g of light, which is of high practical relevance:

$$v_g = \left(\frac{\mathrm{d}k(\omega)}{\mathrm{d}\omega} \right)^{-1} = \frac{c_0}{n + \omega \dfrac{\mathrm{d}n}{\mathrm{d}\omega}} = \frac{c_0}{n_g} \tag{3.42}$$

Here c_0 is the vacuum speed of light, n the refractive index, and n_g the effective group index. As mentioned in Sec. 3.1.2, the advantage of an EIT resonance compared to a simple atomic resonance is that it does not only provide a strong dispersion, but at same time almost unity transmission. In the case of a medium showing perfect EIT ($\gamma_{20} = 0$) in the metamaterial limit, a simple expression for the expected group velocity v_g in the center of the transparency window at ω_{10} can be calculated. Rewriting Eq. 3.40 yields:

$$(kd)^2 \approx \phi^2 - 2\xi\phi \quad \text{with} \quad \xi = i\frac{r}{1+r}, \quad \phi = \frac{\omega d}{c} \tag{3.43}$$

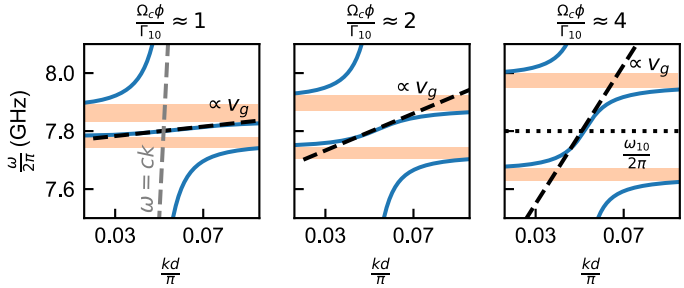

Figure 3.10: Calculated band structure of an infinite qubit array under ATS conditions. The slope of the central band around $\omega_{10}/2\pi = 7.8\,\mathrm{GHz}$ determines the group velocity v_g of light and can be tuned with the control tone strength Ω_c. Used parameters: $\Gamma_{1D}/2\pi = \gamma_{10}/\pi = 12.7$, $\gamma_{20} \approx 0\,\mathrm{MHz}$.

For $\phi > \xi$ (which is in the case of perfect EIT, meaning $r(\omega_{10}) = 0$, always true) this further simplifies to:

$$kd \approx \phi - \xi \tag{3.44}$$

Inserting Eq. 3.26 for the reflection coefficient in the limit of $\omega_c = \omega_{21}, \gamma_{20} = 0$ yields the expected group velocity v_g in the center of the transparency window:

$$\frac{1}{v_g} = \left.\frac{dk}{d\omega}\right|_{\omega=\omega_{10}} = \frac{1}{c} + \frac{2\Gamma_{1D}}{d\Omega_c^2} \quad \rightarrow \quad v_g \approx \frac{d\Omega_c^2}{2\Gamma_{1D}} \tag{3.45}$$

Therefore, by reducing Ω_c, the group velocity of light can be effectively reduced and eventually even stopped [FIM05] (Fig. 3.10). The more complicated scenario of non-vanishing γ_{20}, leading to a minimal value of v_g, is treated in Sec. 5.5. Experimentally, the slow light effect was observed in various cold atom systems, reaching ultra-slow group velocities up to $17\,\mathrm{m/s}$ [Hau+99]. A second important hallmark of the extreme group indices is that light pulses get spatially compressed inside the slow light medium. The origin of the slow light effect can be well explained in the dressed state picture of EIT/ATS [FIM05]. Diagonalizing Hamiltonian 3.18 in the limit of a two-photon resonance ($\omega_p - \omega_{10} = \omega_c - \omega_{21}$) yields:

$$|+\rangle = \sin(\theta)\sin(\beta)\,|0\rangle + \cos(\beta)\,|1\rangle + \cos(\theta)\sin(\beta)\,|2\rangle \tag{3.46}$$

$$|-\rangle = \sin(\theta)\cos(\beta)\,|0\rangle - \sin(\beta)\,|1\rangle + \cos(\theta)\cos(\beta)\,|2\rangle \tag{3.47}$$

$$|D\rangle = \cos(\theta)\,|0\rangle - \sin(\theta)\,|2\rangle \tag{3.48}$$

$$\tan(\theta) = \frac{\Omega_p}{\Omega_c} \qquad \tan(2\beta) = \frac{\sqrt{\Omega_p^2 + \Omega_c^2}}{\omega_{10} - \omega_p} \tag{3.49}$$

The states $|\pm\rangle$ always comprise a component of state $|1\rangle$, which decays radiatively, and are therefore always bright. $|D\rangle$ has no contribution from $|1\rangle$ and is therefore

considered as dark[3]. In the limit of $\Omega_p \ll \Omega_c$, the dark state is given by $|D\rangle = |0\rangle$ and in the opposing limit $\Omega_p \gg \Omega_c$ by $|D\rangle = -|2\rangle$. For a collective EIT-medium, $|D\rangle$ manifests itself as a dark-state polariton [FIM05]. Before an electromagnetic pulse enters the slow light medium, the first condition is fulfilled and the dark-state is given by $|D\rangle = |0\rangle$. As soon as the pulse penetrates the medium and its electric field starts to rise, $|D\rangle$ is rotated to have an admixture of the qubit state $|2\rangle$ or, in other words, an increasing amount of energy is transferred from electromagnetic photons into an atomic excitation. When the pulse leaves the medium, the whole process is reversed and the energy of the dark-state polariton is transferred back to the photon field. Therefore, by varying the control strength Ω_c, the *mixing angle* between photons and qubit excitation, and with it the effective group velocity, can be tuned.

One of the most prominent applications of the slow light effect is the realization of quantum memories, which are able to store and release arbitrary light pulses on demand. Here, a light pulse is send to an slow light medium with $\Omega_c \gg \Omega_p$. Inside the medium the pulse is slowed down and spatially compressed. As soon as the pulse has fully entered the medium, Ω_c is adiabatically ramped to zero, which rotates the dark-state polariton to a pure qubit excitation and thus stores the pulse. After a waiting time, the pulse is released on demand by ramping up the control again and transferring the spin excitation back to a photon field. Quantum memories were experimentally realized in atomic vapors at optical frequencies [Phi+01; Liu+01] and, more recently, with atoms coupled to nanofibers, allowing for several micro seconds of storage time [Gou+15].

[3] Strictly, this only true for Λ-type three-level systems. For ladder-type systems the state $|2\rangle$ is also radiative and therefore $|D\rangle$ is not perfectly dark.

4 Experimental Techniques

This chapter introduces the reader to the experimental methods used in this work, which includes the fabrication of the transmon qubits and the experimental apparatus needed to probe them in a controlled and protected environment. The section on fabrication depicts optical- and electron-beam lithography processes to pattern the qubits from thin aluminum films. Here, special focus is drawn on the reduction of parameter spread in the fabrication of the Josephson junctions using a *bridge-free* shadow evaporation procedure. In order to observe the quantum nature of the qubits, dissipation and thermal population has to be suppressed by cooling to millikelvin temperatures. In this work, these temperatures are achieved using a wet dilution cryostat. The chapter concludes by providing an overview of the microwave setup used to control and probe the qubits in spectroscopic and time-domain experiments.

4.1 Sample Fabrication

The samples used in this work were fabricated in the cleanroom facilities of the Nanostructure Service Laboratory (NSL) of the Center for Functional Nanostructures at Karlsruhe Institute of Technology.

As mentioned in the Introduction (Ch. 1), two main samples were investigated in this work: a short metamaterial comprising eight locally frequency-tunable transmon qubits (sample A) and a longer structure of 90 non-tunable qubits (sample B). The lack of local frequency control leads to two main design requirements: low spread of the critical currents of the qubits on one chip and strong coupling of the qubits to the waveguide (for details see Ch. 6). These requirements translate to high demands regarding the fabrication procedure, which differ from the processes used for sample A.

4.1.1 Thin Film Lithography

All samples in this work are made from thin evaporated aluminum films on 500 µm thick c-plane sapphire wafers with a permittivity of $\epsilon = 11.5$. It is under current debate, whether sapphire improves the coherence of microfabricated superconducting devices compared to other substrates like intrinsic silicon, since interface losses might be dominating [McR+20].

Prior to fabrication the used wafers are rinsed with piranha solution (sulfuric acid H_2SO_4 and hydrogen peroxide H_2O_2) to remove organic contaminations. For both samples (A and B) the transmon qubits are patterned in a first step, before any other structures are made (Fig. 4.1). This is done in order to deposit the qubits on the cleanest possible surface. From other works it is known that dirty interfaces between qubits and substrate, e.g. due to photo-resist residuals from prior fabrications steps, can significantly reduce the intrinsic qubit coherence without extensive cleaning [Qui+14]. After spincoating the wafer with a PMMA-MAA copolymer (EL-13) / PMMA (A-4) double photo resist stack, the qubits are patterned with electron-beam lithography using a 50 keV JEOL JBX-5500ZD. A thin gold layer ($\approx$ 5 nm) is sputtered on the resist stack to prevent charging of the sample in the e-beam writing process. The thin aluminum films which make up the qubits are thermally evaporated in a PLASSYS MEB550s shadow evaporator. More details on the bridge-free shadow evaporation process of the qubits are given in section 4.1.2.

For sample A this first e-beam step is followed by a positive optical lithography step, where all other structures on the chip (being flux-bias lines, groundplane and waveguide) are formed (compare Fig. 4.1(a)). This second step is necessary to save e-beam writing time for all structures where nanometer resolution is not required. Here, S1805 optical photo-resist is spincoated on the substrate with the ready-made qubits. The chip is aligned with an optical chromium mask (soda lime glass) in a Carl Suess MA6 maskaligner and exposed with 240 nm UV light. After development of the resist, 75 nm of aluminum are evaporated in the Plassys subsequently to an in-situ 20 s 5 sccm Ar/ 10 sccm O_2 *descum*. The fabrication of sample A is concluded with a lift-off process of the unexposed resist in N-Ethyl-2-pyrrolidon (NEP).

For sample B the fabrication procedure differs from sample A after the first qubit fabrication step. Here, the required large coupling capacitance ($C_c \approx 17$ fF) of the qubit to the waveguide with simultaneously compact qubit dimensions leads to a coupling distance of 500 nm (see Sec. 6.1). Therefore, an additional e-beam step with a EL-13/A-4 resist stack is required to ensure the needed resolution. Since this resolution is only needed in the vicinity of the coupling areas, solely the center strip of the coplanar waveguide and a 12.5 µm wide strip of the surrounding groundplane

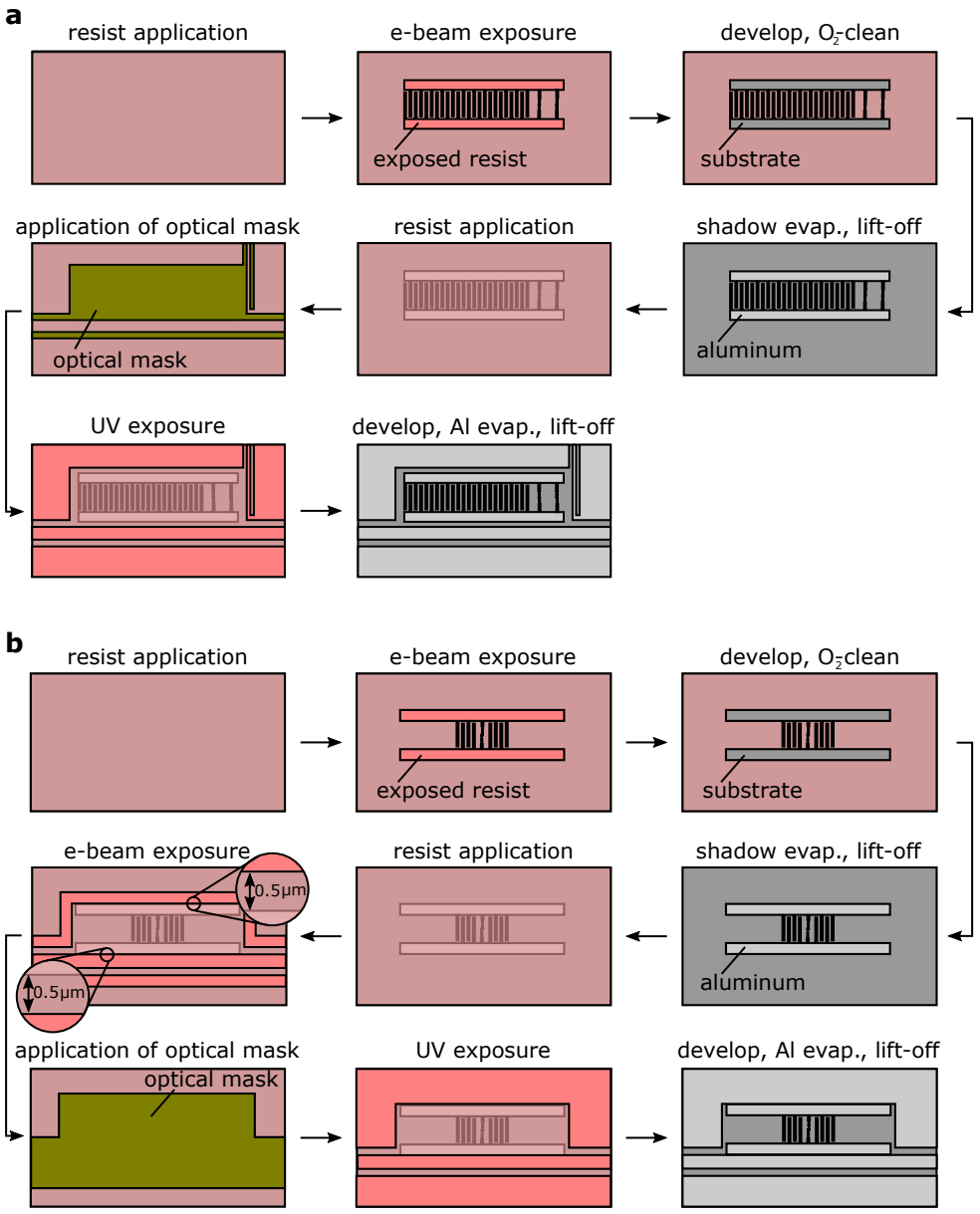

Figure 4.1: Process flow chart of the used fabrication techniques. (a) Fabrication steps for sample A. The qubits are patterned with e-beam lithography, whereas the waveguide and the metallic groundplane are made with optical lithography. (b) Fabrication steps for sample B. Here, the qubits are patterned with e-beam lithography, while the waveguide and groundplane is patterned with a hybrid of optical and e-beam lithography, due to the small gap of 0.5 µm between qubit and waveguide.

are written with the electron beam (see Fig. 4.1(b)). Before development, the exposed resist is covered with an optical silica glass mask in the maskaligner and the residual parts of the groundplane are flood exposed with 240 nm UV light for 35 min. Silica glass is needed because it is partially translucent for UV light, as required to expose the EL-13/A-4 resist stack. After this additional optical exposure, the resist is developed and the groundplane and waveguide are evaporated from aluminum in a lift-off process, similar to sample A. For a detailed description of the used fabrication recipes, see appendix A.

4.1.2 Josephson Junctions

Despite the trend for more streamlined fabrication processes in the field of superconducting qubits, involving non-angle dependent desposition of trilayer Josephson junctions [Ste+20; Wu+17] for large scale quantum-computing, angle-dependent shadow evaporation techniques are still widely spread due to their fast in-situ junction fabrication in a single lithography step. In this work, the Josephson tunnel barriers are fabricated from an $Al/AlO_x/Al$-stack in a bridge-free shadow-evaporation process [Lec+11] based on a PMMA-MAA copolymer (EL-13) / PMMA (A-4) double resist stack (see Fig. 4.2). After spincoating the two layers of resist ($\approx$ 850 nm EL-13 and $\approx$ 150 nm A-4), the junction geometry is written using e-beam lithography. Due to the different sensitivity of the resists it is possible to create overhangs, where only the lower resist is fully exposed and gets removed in the development process. The development is done in a cooled 6 °C mixture of 3:1 IPA:H_2O to improve contrast [OS06]. The developed resist stack (Fig. 4.2(b)) is first treated with 6 min of cleaning with an oxygen plasma and then mounted in the Plassys shadow evaporator. Here it is additionally cleaned with a 40 s 5 sccm Ar/ 10 sccm O_2 *descum*. The first (lower) 45 nm thick layer of aluminum is evaporated at a rate of 1.0 nm/s under an angle of $\theta = -30°$, followed by static in-situ oxidation for 10 min at an oxygen partial pressure of 10 mbar (for sample B slightly varying parameters were used, see appendix A). Thereafter, the second (top) 55 nm thick layer of aluminum is evaporated at a rate of 1.0 nm/s under an angle of $\theta = +30°$, followed by a lift-off in NEP.
In this work, the bridge-free fabrication technique is preferred over the widely spread Dolan-Niemeyer technique [NK76; Dol77], since the lack of an overhanging bridge comes with two advantages. First, the junction area of the developed resist stack is open and can be more effectively cleaned. Second, arbitrarily large junction areas can be fabricated [Lec+11]. Both of the latter are required to optimize the Josephson junctions for low spread in critical current across a wafer, as required for sample B.

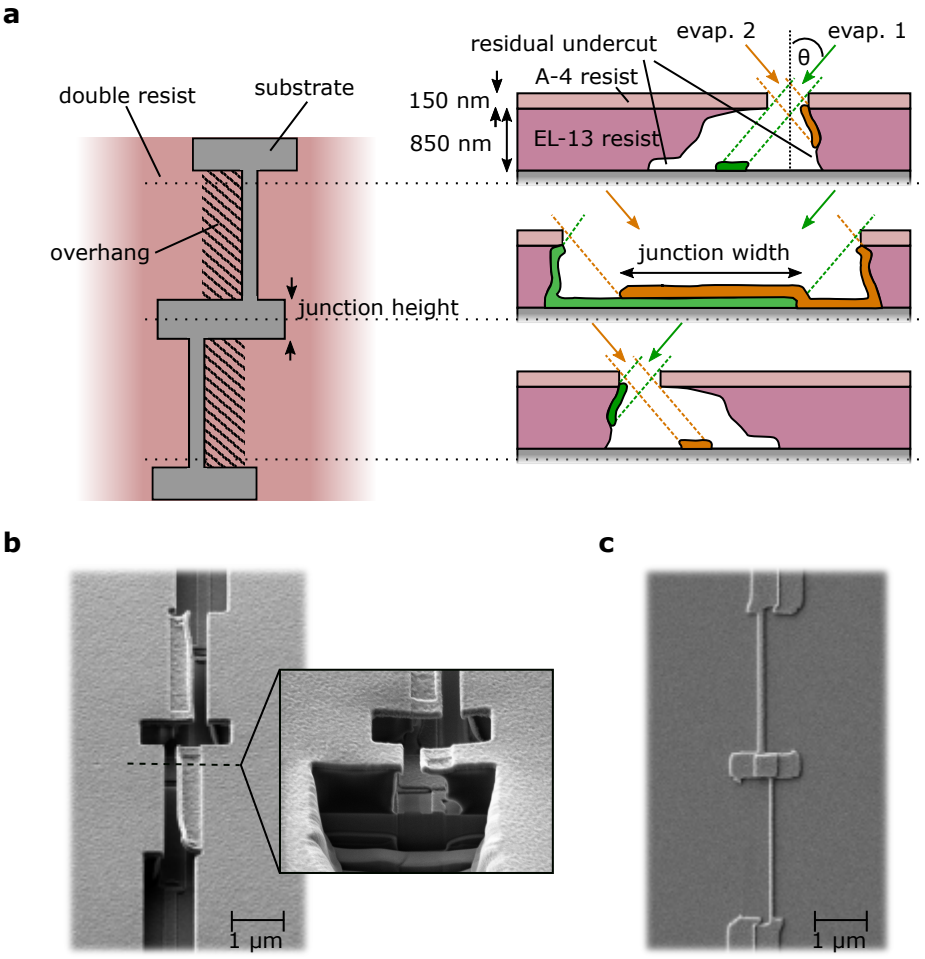

Figure 4.2: Fabrication of Josephson junctions using a bridge-free shadow evaporation process. (a) Left: top view of developed double resist stack after e-beam lithography. Right: cross-sections of junction connection wires (top, bottom) and the area of the Josephson contact (center) during two-angle evaporation of aluminum. Overhanging parts of the top resist cut the connection wires, which would short the contact. (b) SEM image of developed double resist stack after shadow evaporation. The inset shows a cross-section obtained with a focused ion beam (FIB) of the connection wires, depicting the overhang and the residual undercut. (c) SEM image of a completed Josephson junction after lift-off of the double resist.

The inhomogeneity of per design identical Josephson junctions across a wafer is mainly caused by [MBD99]:

1. junction area variations in the lithography process
2. thickness variations of the oxide barrier
3. diffusion processes in the oxide barriers (known as *aging*)
4. leakage currents through pinholes in the barrier

In this work, special focus is drawn on improving points 1.) and 3.). Junction area fluctuations across a wafer are caused by imperfections of the e-beam lithography process, being finite resolution, proximity effects, inhomogeneous development and local variations in the used resist stack. Since the amplitude of these fluctuations is to first order independent of the used junction area A_J, the spread in I_c can be decreased by increasing A_J. This comes however at the cost of increasing the amount of strongly coupled parasitic two-level systems (TLS) in the amorphous oxide in the junction barrier, which are known to reduce qubit coherence [Mar+05; MCL19]. Furthermore, the maximum A_J is limited by the maximal junction capacitance $C_\mathrm{J} \leq 60\,\mathrm{fF} \approx C_\Sigma$ for the desired transmon parameters. Here, the junction capacitance C_J is calculated by approximating the Josephson contact as a plate capacitor:

$$C_\mathrm{J} = \epsilon_0 \epsilon_\mathrm{r} \frac{A_\mathrm{J}}{d} \quad \text{with} \quad \epsilon_\mathrm{r}^{\mathrm{AlOx}} \approx 10,\ d \approx 2\,\mathrm{nm} \tag{4.1}$$

Table 4.1 summarizes the obtained spreads σ_{R_n}/R_n in normal resistance R_n of 64 identical test-contacts over an area of 5 mm×5 mm, fabricated with the bridge-free technique for different A_J. Even though sufficiently small spreads ($\sigma_{R_n}/R_n \approx 1\,\%$) can be reached, annealing the test-contacts (200 °C for 10 min) increases the spread and the normal resistance R_n by roughly 50 %. The process of annealing is similar to an accelerated aging process of the tunnel-barrier, where R_n increases due to diffusion processes of photo resist residuals into the AlO_x [Pop+12]. Therefore, for the junctions used in this work the developed double resist stack was additionally treated with an oxygen plasma for 6 min prior to shadow-evaporation, such that

Table 4.1: Spread in normal resistance $\sigma_{R_\mathrm{n}}/R_\mathrm{n}$ in dependence on junction area A_J. Measured for arrays of 64 test-junctions over an area of 5 mm × 5 mm.

A_J ($\mu\mathrm{m}^2$)	σ_{R_n}/R_n (%)	σ_{R_n}/R_n (after anneal) (%)	C_J (fF)
0.6 × 0.6	1.8	3.2	16
0.8 × 0.8	1-1.6	2.1-3.1	28
1.0 × 1.0	0.87	3.6	44

the junction area contains fewer resist residuals and the effect of aging can be partially mitigated [KVM07; Pop+12].

Table 4.2 summarizes the characteristics of the Josephson junctions used for sample A and B. The parameters were extracted from test-contacts fabricated on the same wafers as the used samples. Whereas for sample B large area junctions (0.8 µm × 0.8 µm) are used, sample A is based on smaller junctions (0.34 µm × 0.34 µm and 0.28 µm × 0.28 µm in a SQUID configuration), since high junction homogeneity is not needed because of the local frequency control. For the fabrication of both samples the additional O_2 plasma cleaning step was used. The full fabrication parameters are listed in appendix A.

Table 4.2: Josephson junction parameters of samples A and B. The qubits of sample A have two per design different junctions in parallel, forming a dc-SQUID. The normal resistance spread σ_{R_n}/R_n of the Josephson junctions of sample B is measured on 64 test contacts fabricated in the same batch as the sample.

Device	A_J ($\mu\mathrm{m}^2$)	I_c[1] (nA)	σ_{R_n}/R_n (after anneal) (%)	C_J (fF)
Sample B	0.8×0.8	27	2.2	28
Sample A	0.34×0.34	39	-	5
Sample A	0.28×0.28	31	-	3

4.1.3 Sample Housing

In order to interface the on-chip structures to the microwave coaxial cables and to thermally anchor the chip to the base plate of the cryostat, the sample is embedded into an aluminum sample holder. Simultaneously, the superconducting holder shields it from outer magnetic fields, mechanical damage and provides a highly coherent electromagnetic environment for the qubits [Lie+19]. This is achieved by designing the geometry of the sample holder, such that its own electromagnetic modes don't fall into the relevant frequency range of $5 - 10\,\mathrm{GHz}$ and provide an additional decay channel for the qubits [Lie+19].

The completed chips after lithography are diced from a larger wafer to their final form (sample A 5 mm × 5 mm, sample B 10 mm × 5 mm) using a wafer dicing saw (DISCO DAD3350). The chips are glued with GE-varnish or silver conducting paste into their sample holder together with printed circuit boards (copper on

[1] Derived from measured normal-state resistance R_n and the Ambegaokar-Baratoff relation (Eq. 2.19)

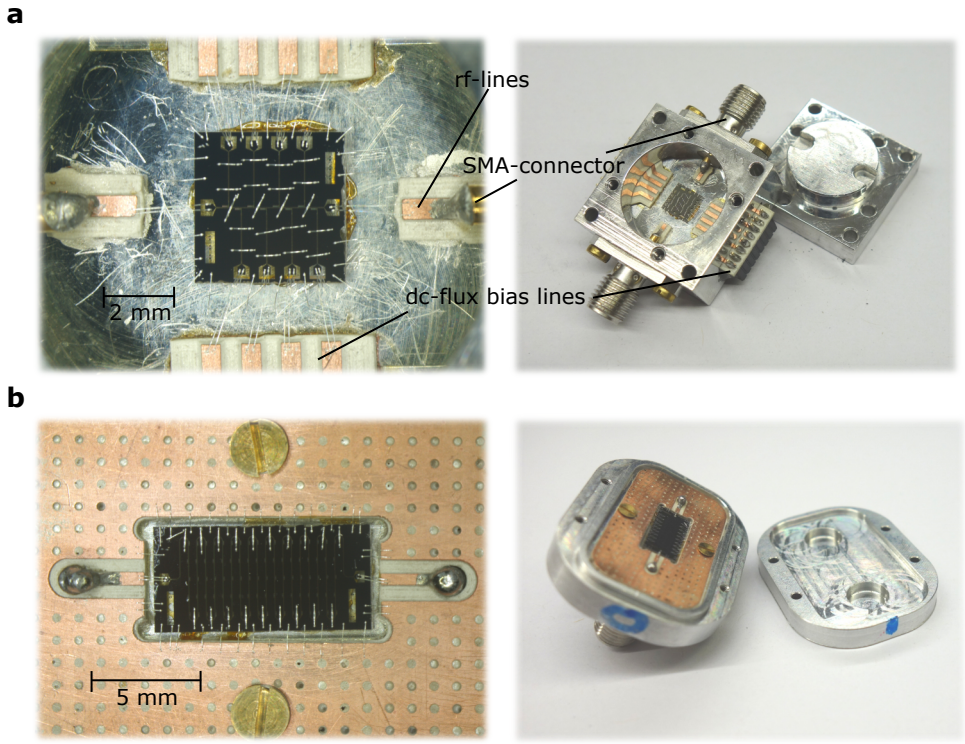

Figure 4.3: Sample housings for shielding and thermally anchoring the chips. (a) Housing for sample A. The qubit chip is glued with GE-varnish to the aluminum housing. On-chip wires are wire bonded to custom copper printed circuit boards, which provide the connection to coaxial rf and dc cables in the cryostat. (b) Sample housing for sample B. Due to the lack of local flux tunability, only rf connections are needed.

TMM10 dielectric), which are soldered to microwave SMA connectors and dc-cables to connect the samples from outside the holders (see Fig. 4.3). The connection between circuit boards and on-chip structures is made with aluminum bond wires. In addition several on-chip bond wires are placed, shorting different parts of the ground plane, to reduce the number of spurious on-chip modes and therefore to increase qubit coherence. Due to the different dimensions of sample A and B, as well as the need for eight additional dc-control lines for sample A, two different designs of sample holders were used (compare Fig. 4.3).

4.2 Cryogenic Setup

Millikelvin temperatures are required to reach the *quantum regime* with superconducting qubits, meaning their energy-level separation is larger than their linewidth due to dissipation and thermal excitations are sufficiently suppressed [VD17]. Although superconductivity is already reached at significantly higher temperatures ($T_c^{Al} \approx 1.2\,K$ [CM58]), the limiting factor for the qubit coherence at nonzero-temperatures are dissipation due to superconducting quasi-particles and thermal population of higher qubit states. Reducing the thermal population of the first excited qubit state below $0.05 \approx \exp\left(-\frac{hf_{10}}{k_B T}\right)$ at a typical level splitting of $f_{10} = 5\,GHz$ requires a temperature of $T = 80\,mK$. Whereas cryogenic temperatures of $1.5 - 4.2\,K$ ($> 300\,mK$) are typically reached with evaporative cooling of liquid ^4He (^3He) at different vapor pressures, temperatures below 300 mK require adiabatic demagnetization or $^3He/^4He$ dilution refrigerators [Pob07].

In this work, the qubits are cooled down to temperatures of $10 - 20\,mK$ with a wet custom build $^3He/^4He$ dilution refrigerator as depicted in Fig. 4.4. "Wet" means here, that the cryostat has two reservoirs of liquid nitrogen and liquid helium, shielding and pre-cooling the colder parts of the cryostat by evaporative cooling. Both of the reservoirs have to be refilled periodically to keep the cryostat cold. An outer vacuum chamber (OVC) decouples the reservoirs and the other cold parts of the cryostat from the room temperature environment. The main cooling unit of a $^3He/^4He$ dilution refrigerator is based on a phase separation of a mixture of the helium isotopes ^3He and ^4He into a diluted phase of both isotopes and a phase of pure ^3He below temperatures of 867 mK [Pob07]. A cooling effect is achieved by exothermically forcing ^3He-atoms from the pure phase into the diluted phase. It is crucial for the process that even for temperatures below 100 mK the fraction of ^3He in the diluted phase does not drop below 6.6 %, ensuring a large molecular flow of ^3He between the two phases.

As shown in Fig. 4.4, in a cryostat this effect is exploited in the following way: the $^3He/^4He$ mixture is used in a closed cycle, driven by a ^3He-pump, allowing to obtain continuous cooling power. Central element is the mixing-chamber, which is thermally anchored to the base plate at 20 mK of the cryostat and contains both phases of the mixture. The pure ^3He is floating on top of the diluted phase due to its lower density. A continuous transfer of ^3He into the diluted phase is realized by pumping on the diluted phase in the still at 600 mK. Since at this temperature the vapor pressure of ^3He is significantly larger than of ^4He, only

[2] Picture taken from [Sch19] with permission of S. Schloer.

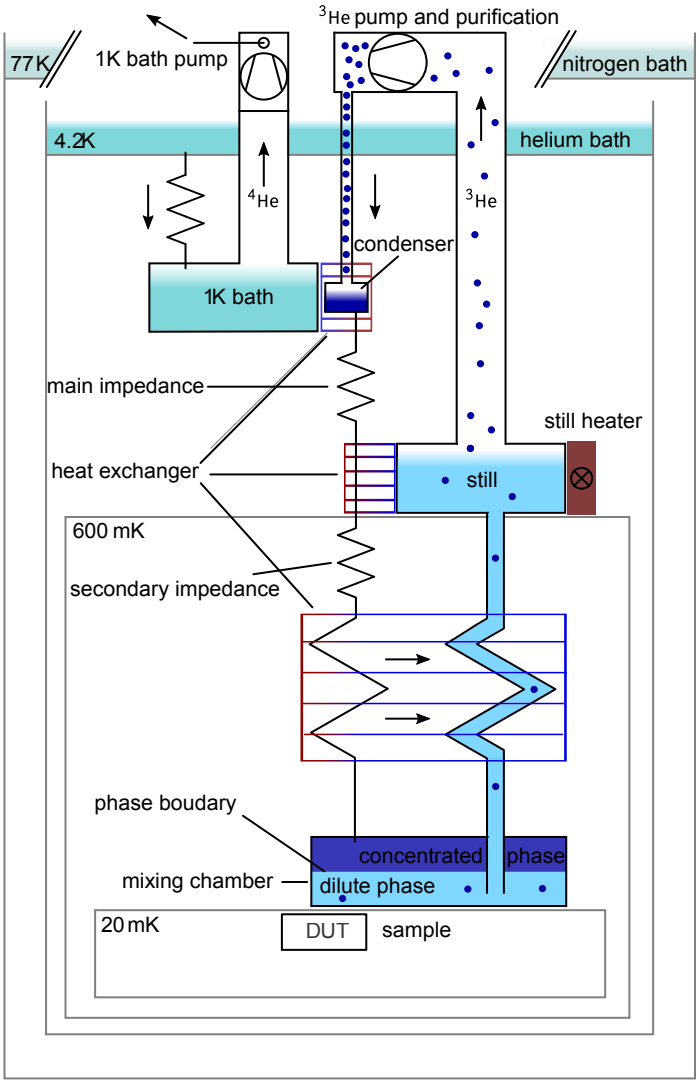

Figure 4.4: Working principle of a ^{3}He/^{4}He dilution refrigerator[2] as used in the experiments for this work. The cooling is based on a phase separation of the ^{3}He/^{4}He mixture into a diluted phase of both isotopes and a concentrated ^{3}He-phase. Here, a "wet" cryostat is used, relying on liquid nitrogen and helium baths to shield and precool the lower temperature stages. The qubit samples are mounted with their housing to the base plate of the cryostat at $10 - 20\,\mathrm{mK}$.

^{3}He gets removed from he diluted phase. Due to osmotic pressure there is a constant flow of ^{3}He between mixing chamber and still. The ^{3}He-vapor gets recondensed in the condenser by heat exchange with the 1K-Pot, a separate ^{4}He-evaporation cooler at 1.5 K. On the way back to the mixing chamber the liquid ^{3}He passes several impedances, which establish the needed pressure in the condenser. Simultaneously it passes several heat-exchangers to get further cooled by the diluted phase counterpropagating to the still. Because of the closed-cycle design a dilution refrigerator can, if necessary, be run for several months.

4.3 Microwave Setup

The electronics used for experiments with superconducting qubits is divided in radio-frequency (rf) and direct-current (dc) components, as well as in cryogenic and room temperature components. The rf-components are in the microwave frequency range of $4 - 8$ GHz to drive and probe the qubits around their transition frequency. The dc-components are used to flux-bias frequency-tunable qubits.

4.3.1 Cryogenic Microwave Setup

The samples mounted to the base plate of the cryostat are connected to the microwave electronics at room temperature (see Sec. 4.3.2) via 50 Ω coaxial cables. Since thermal noise from room temperature is known to strongly contribute to qubit dephasing [Yeh+17], special care has to be taken to attenuate, to filter and to thermalize the coaxial cables [Kri+19]. The thermal noise of a resistor R at temperature T, is known as Johnson-Nyquist noise. Its two-sided power spectral density is given by [GZ04]:

$$S_{\text{th}}(T,\omega) = 2R\hbar\omega n_{\text{BE}}(T,\omega) \quad \text{with} \quad n_{\text{BE}}(T,\omega) = \frac{1}{\exp\left(\frac{\hbar\omega}{k_{\text{B}}T}\right) - 1} \tag{4.2}$$

In order to prevent this noise from room temperature ($T_{\text{RT}} = 300\,\text{K}$) reaching the sample, three 20 dB microwave attenuators (attenuation $A_i = 100 = 20\,\text{dB}$), thermalized at the helium bath ($T_{4\text{K}} = 4.2\,\text{K}$), intermediate stage ($T_{\text{IM}} \approx 50\,\text{mK}$) and base plate ($T_{\text{B}} = 20\,\text{mK}$) are inserted into the coaxial cables (see Fig. 4.5). Therefore, the mean noise photon occupation number $n_i(T,\omega)$ at stage $i \in \{\text{RT, 4K, IM, B}\}$ is given by [Kri+19]:

$$n_i(T_i,\omega) = \frac{n_{i-1}}{A_i} + \frac{A_i - 1}{A_i} n_{\text{BE}}(T_i,\omega) \tag{4.3}$$

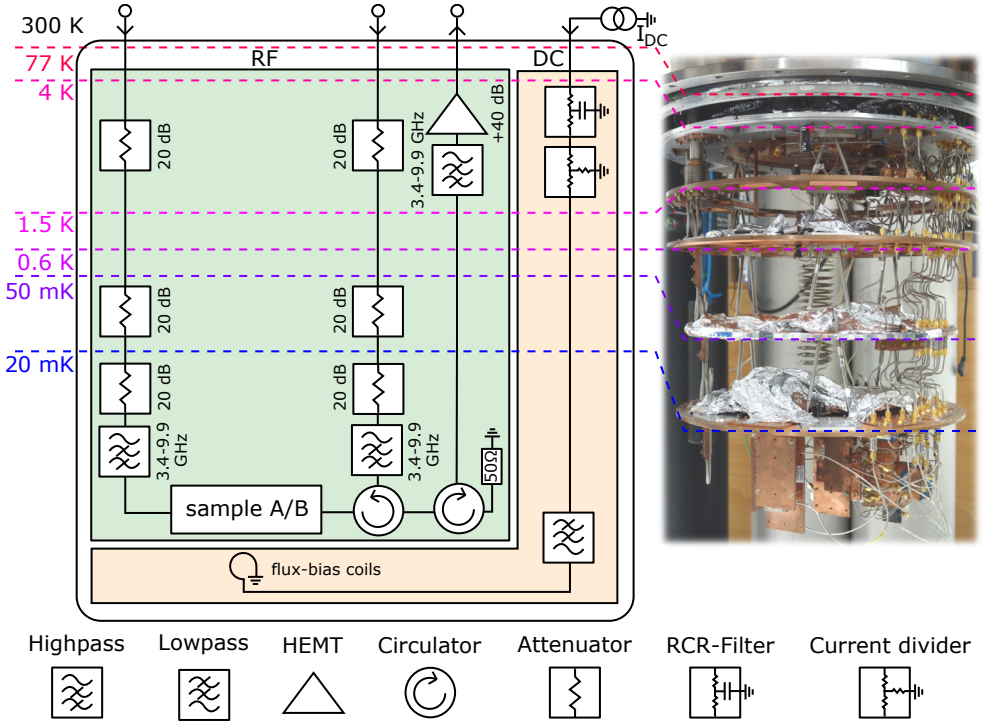

Figure 4.5: Cryogenic radio-frequency (light green) and direct-current (light orange) setup with indicated temperature stages. Two coaxial rf input lines are used for transmission and reflection experiments, while for the output signal always the same amplification line is used.

The first term of Eq. 4.3 accounts for the attenuated noise from the stage above, whereas the second term accounts for its own noise contribution due to its finite temperature. With three cascaded attenuators the mean noise photon occupation number at the base plate is reduced to $n_B \approx 0.002$ at a typical frequency of $\omega/2\pi = 6\,\text{GHz}$, meaning only 0.002 photons of thermal noise are added per signal photon. By dividing the total attenuation of 60 dB in separate 20 dB attenuators, the noise coming from stage $i-1$ is roughly reduced to the intrinsic thermal noise of stage i. Any further attenuation would thus not significantly improve the noise reduction. At the same time it is ensured that the major part of the power is dissipated at the 4K-stage, which has sufficient cooling power. As shown in Fig. 4.5, additional high pass filters are used at the base plate to shield the sample from frequency components outside of the used frequency band ($4-8\,\text{GHz}$). Stainless-steel coaxial cables are used for all ingoing rf-signals to the sample, since they provide good thermal decoupling of the temperature stages of the cryostat and

their slightly increased resistive losses ($\approx 10 - 25\,\mathrm{dB}$ from room temperature to base, depending on the frequency) are not harmful as described above.

In this work, typical on-chip single photon powers are $P \approx -128\,\mathrm{dBm}$, which corresponds to voltages of $0.1\,\mu\mathrm{V}$. Since the electronics for detection of the scattered microwave signals is typically sensitive for voltages $1\,\mathrm{mV} - 1\,\mathrm{V}$, the microwave signals have to be strongly amplified before detection. Here, a cascaded system of a cryogenic high electron mobility transistor (HEMT, Low Noise Factory LNC4 8C s/n 200A) and room temperature amplifiers (see Sec. 4.3.2) is used. For the effective noise-temperature T_{eff} of such a system Friis formula applies [Fri44]:

$$T_{\mathrm{eff}} = T_1 + \frac{T_2}{G_1} + \frac{T_3}{G_1 G_2} + \cdots \tag{4.4}$$

T_i and G_i are noise-temperature and gain of the i-th amplifier. As can be seen from Eq. 4.4, the noise performance of the first amplifier is dominating the overall noise performance of the chain. Here, the noise temperature of the used HEMT is 2 K. It is noted that the noise performance of the amplification setup could be further improved by resorting to near quantum noise limited amplifiers as first elements in the amplification chain [RD16; Mac+15]. To improve the signal to noise ratio and prevent signal loss before amplification, superconducting cables are used from the sample to the HEMT amplifier. Additional high pass filters and microwave circulators (Quinstar CTH1392KS) are employed to shield the sample from HEMT noise radiated backwards. In the used configuration, the circulators also allow for measurements of signals reflected from the sample (Fig. 4.5). In this work, the reflected signals are always probed on the right side of the sample (defined here as port 2 of the two-port networks of samples A and B, corresponding to $S_{22}(\omega)$), whereas transmission is probed from left to right (port 1 to 2, corresponding to $S_{21}(\omega)$).

Following the principle of noise reduction as explained above for the coaxial lines, thermal noise in the dc-flux bias lines gets reduced by 14:1 current dividers and RCR lowpass T-filters at the 4 K stage. Copper-powder lowpass filters at the base plate are used to further reduce high-frequency noise and to thermalize the wires before reaching the sample [LU08].

4.3.2 Room Temperature Microwave Setup

In this work, two main classes of microwave experiments are conducted: spectroscopic and time-resolved measurements. Depending on which technique is used, the employed microwave room temperature setup varies (see Fig. 4.6). Both setups share a common microwave frontend, which is directly attached to the cryostat. For

incident signals it provides, in dependence on the experiment, variable additional attenuation and offers the possibility to combine the signals with an additional drive or control microwave tone using a directional coupler. For outgoing signals, the frontend additionally amplifies the signal with a pair of room temperature amplifiers (Mini-Circuits ZVA-213+, $+26\,\mathrm{dB}$ gain) before detection.

In spectroscopic measurements, the steady state scattering response of the sample under investigation is probed by using a commercial vector-network analyzer (VNA, Agilent E5071C). With a VNA the complex matrix elements of the scattering matrix $S(\omega)$ (Eq. 3.2) can directly be accessed. Its working principle is based on sending sinusoidal microwaves with varying frequency to the sample, followed by a narrow-band heterodyne detection of the scattered signal [Poz11]. By comparing the detected signal to a reference, changes in phase and amplitude or in-phase and quadrature components can be measured.

In time-domain measurements microwave pulses with varying envelope and carrier frequency are generated, sent to the sample and the full time dependent response by means of the scattered light is detected. To cover the full dynamics of the system a large detection bandwidth is required. The central element of the setup is a Xilinx ZCU111 evaluation board featuring an RFSoC architecture. This combines CPUs, an FPGA, DACs and ADCs for signal generation and detection on a single chip. The system is operated with custom firmware and an effective sampling rate of 1 GS/s [Geb+20a; Geb+20b]. Since to this date there are no fast enough DACs to synthesize arbitrary microwave signals in the desired band ($4-8\,\mathrm{GHz}$) directly, a heterodyne setup based on single-sideband mixing with IQ-mixers is used (see Fig. 4.6). This means the DACs generate the desired pulse shapes modulated with an intermediate frequency $f_{\mathrm{IF}} = 115\,\mathrm{MHz}$. The in-phase and quadrature component of the signal are created independently. In the IQ-mixer the pulses at intermediate frequency get mixed with a local oscillator at frequency f_{LO} (in the GHz range) and are therefore up-converted to radio-frequency $f_{\mathrm{rf}} = f_{\mathrm{LO}} + f_{\mathrm{IF}}$. It is noted that the corresponding mirror-frequency $f'_{\mathrm{rf}} = f_{\mathrm{LO}} - f_{\mathrm{IF}}$, which normally is created in a mixing process, destructively interferes in the IQ-mixer. Thus, only the single upper-sideband at f_{rf} is send to the cryostat after the IQ-mixer. In contrast to a homodyne setup (where $f_{\mathrm{IF}} = 0$ and $f_{\mathrm{rf}} = f_{\mathrm{LO}}$) the heterodyne technique mitigates the effect of local oscillator leakage through the mixer, since it is detuned from the frequency of the sample (f_{rf}). Here, additional low-pass filtering directly after the DACs is used to remove parasitic high frequency components due to the finite sampling rate. The detection of scattered microwave pulses is realized analogously to the up-conversion process: a second IQ-mixer is used to down-convert the incoming rf signal with the local-oscillator to intermediate frequency, separated in

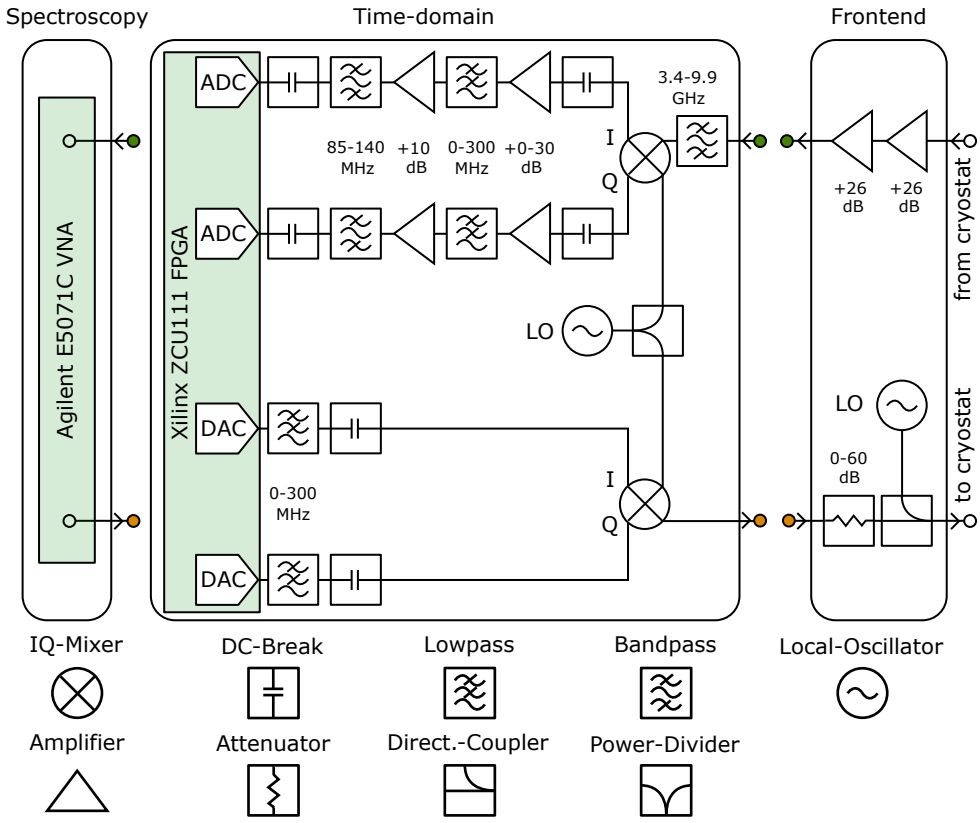

Figure 4.6: Sketch of the used room temperature microwave electronics. For spectroscopic measurements a commercial vector network analyzer is used, while time resolved experiments are conducted with a custom build FPGA-based heterodyne setup. For both types of measurements a common microwave frontend is used: signals first pass variable attenuators and are optionally combined with an additional microwave tone, before being sent into the cryostat. Incoming signals are further amplified by a pair of room temperature amplifiers before detection.

in-phase and quadrature component. Additional low-and bandpass filters are used to remove amplifier noise outside of the frequency band of interest.

5 Waveguide Band Gap Engineering with a Qubit Metamaterial

This chapter provides the results on the experiments with an eight qubit waveguide quantum electrodynamics (wQED) system featuring local frequency control. After providing some general information on the circuit layout, qubit characterization and the calibration of magnetic crosstalk, the effective qubit-qubit interaction is addressed. The collective polariton excitations in the single excitation sector are spectroscopically probed. By consecutively tuning the qubits to a common resonance frequency, insights into the dependence of polariton lifetimes on the number of participating qubits and the emergence of a band gap are obtained. Furthermore, collective non-linear properties as saturation and collective Autler-Townes splitting (ATS) are studied. The latter effect is then used to demonstrate with pulsed experiments in the time-domain slow light in the eight qubit metamaterial, where the group velocity of light is reduced by a factor of 1500. Furthermore, using the frequency control, tailored band structures with an engineered dispersion profile are used to obtain a similar effect. In the last section of this chapter experiments on artificial frequency disorder are presented which might serve as a useful tool to study Anderson localization in one-dimensional photonic systems.

5.1 Design Considerations

Fig. 5.1 shows an overview of sample A as used for the experiments presented in this chapter. Here, the wQED system is formed by eight locally frequency tunable transmon qubits side-coupled to a coplanar waveguide. Its circuit layout was chosen based on the following design requirements:

1. **Metamaterial limit**: a dense spacing between adjacent qubits of $d = 400\,\mu\text{m}$ is chosen to fulfill the metamaterial limit of sub-wavelength dimensions, which is at all accessible frequencies ($\approx 3 - 8\,\text{GHz}$) significantly smaller than the corresponding wavelength λ. The phase drop between neighboring

qubits is $\phi = \frac{2\pi}{\lambda} d \approx 0.05 - 0.16$[1]. Furthermore, the transmon qubits are designed as compact as possible to mitigate the effect of a phase drop over the spacial extend of the qubit. Due to the dense spacing, the effective qubit-qubit interaction of Eq. 3.30 between neighboring qubits is by a factor of ≈ 10 dominated by the cooperative dissipation term.

2. **Strong coupling**: large Purcell factors or extinction coefficients (this requires radiative decoherence to dominate the non-radiative intrinsic decoherence $\Gamma_{1D}/2 \gg \Gamma_{nr}$) close to unity are desirable since they increase the subradiant state visibility (see Sec. 3.2.3). This can be best satisfied with a large coupling capacitance C_c of the qubit to the waveguide (Eq. 3.15). Simultaneously, the corresponding qubit lifetime $T_1 \approx 1/\Gamma_{1D}$ has to be large enough that time-dependent qubit dynamics can be resolved with the given microwave electronics (see Sec. 4.3.2). Here, $C_c \approx 7\,\mathrm{fF}$ is used, which leads to $1/\Gamma_{1D} \approx 25\,\mathrm{ns}$ at a qubit frequency of $8\,\mathrm{GHz}$.

3. **Local frequency control**: individual qubit frequency control is required to tune the qubits to a common resonance frequency and to alter the number of resonant qubits N. The qubit frequency is tunable via magnetic flux which controls the Josephson energy of the qubit's split Josephson junction (SQUID). Each SQUID is inductively coupled to an individual on-chip flux coil that consists of a dc-current biased transmission line which is terminated at the common ground plane (see Fig. 5.1, right inset). Magnetic crosstalk between the lines and non-adjacent qubits is calibrated out by using a crosstalk-compensation scheme (see Sec. 5.2).

4. **No direct qubit-qubit coupling**: The model Hamiltonian of Eq. 3.30 does not account for additional direct qubit-qubit interactions via a mutual cross-capacitance. The qubit-qubit capacitance was calculated using a finite-element solver ANSYS Maxwell for the used spacing d (not reported here), and turned out to be negligible compared to the qubit-transmission line capacitance C_c.

The experimentally obtained parameters of the individual qubits are listed in table 5.1 of Sec. 5.3.1.

[1] The employed coplanar waveguide has an effective speed of light of $c = 1.2 \cdot 10^8\,\mathrm{m/s}$ and an impedance of $Z_0 = 50\,\Omega$ for the used geometry and materials (center conductor width: $14.4\,\mu\mathrm{m}$, gap width: $7.7\,\mu\mathrm{m}$, sapphire substrate). The value was obtained in a numerical simulation using TX-Line [Cad].

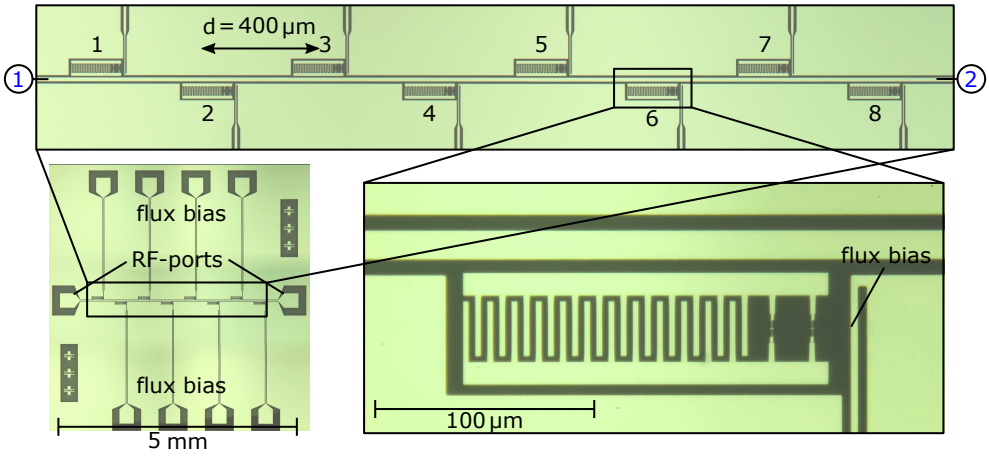

Figure 5.1: Microscopic images of the eight qubit metamaterial (sample A) consisting of transmon qubits capacitively side-coupled to a common coplanar waveguide. Local dc flux bias lines ensure individual qubit frequency control. The spacing between adjacent qubits is $d = 400\,\mu\text{m}$, which is at all accessible qubit frequencies smaller than the corresponding wavelength λ ($d \ll \lambda$). The qubits are numbered from left to right in the direction of the transmission measurement (ports of the two-port microwave network are indicated with blue numbers).

5.2 Flux Tunability and Crosstalk Calibration

As shown in Sec. 2.2.3, the energy splitting of a qubit can be tuned with a magnetic flux penetrating its SQUID. The flux Φ_i used to tune qubit i is generated by applying a dc-current I_i (given as current provided by the current source at room temperature and not as on-chip current) to its corresponding on-chip bias coil. Quantitatively, the frequency of the $1 \rightarrow 0$-transition f_{10} in dependence on the magnetic flux Φ of the bias coils is given by (Eqs. 2.29 and 2.40):

$$\begin{aligned} f_{10}(\Phi) &= \frac{\sqrt{8E_\mathrm{J}(\Phi)E_\mathrm{C}} - E_\mathrm{C}}{h} = \frac{\sqrt{8\frac{\Phi_0}{2\pi}I_{\mathrm{c,eff}}(\Phi)E_\mathrm{C}} - E_\mathrm{C}}{h} \\ &= \frac{\sqrt{8\frac{\Phi_0}{2\pi}(I_{\mathrm{c,a}} + I_{\mathrm{c,b}})\cos\left(\frac{\pi\Phi}{\Phi_0}\right)\sqrt{1 + m^2\tan^2\left(\frac{\pi\Phi}{\Phi_0}\right)}E_\mathrm{C}} - E_\mathrm{C}}{h} \end{aligned} \tag{5.1}$$

Here, m is the asymmetry between the critical currents ($I_{\mathrm{c,a}}$, $I_{\mathrm{c,b}}$) of the two Josephson junctions constituting the SQUID (see Eq. 2.29). Fig. 5.2 shows the measured frequency dispersion of qubit 1. In good agreement with Eq. 5.1, the qubit can be periodically tuned between its upper- and lower sweet spot ($f_{10}^{\min}$ and $f_{10}^{\max}$). The extracted sweet spot frequencies and junction asymmetries for all eight qubits are listed in Tab. 5.1 of the following section. The tuning precision is limited by the

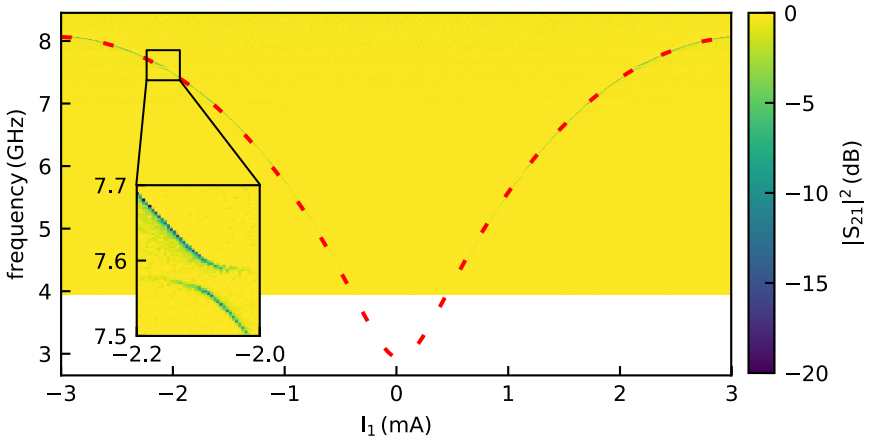

Figure 5.2: Frequency tunability of qubit 1 with applied current I_1 in its corresponding flux bias coil between $f_{10}^{\min}$ and $f_{10}^{\max}$. Due to the per design asymmetric Josephson junctions in the SQUID, the qubit dispersion obtains a lower sweet spot. The red dashed line is a fit to the expected qubit dispersion of Eq. 5.1. The inset shows an avoided-level crossing of the qubit with a strongly coupled TLS.

resolution of the DAC, used to set the currents, to 0.1 µA. This translates in the frequency range $7 - 8$ GHz close to the upper sweet spot, where all experiments of this work are conducted, to a frequency precision of < 100 kHz. Stability measurements over 15 h (not shown) indicate that current drifts are negligible. However, depending on the operating frequency, the qubits feature strongly coupled parasitic TLS in their spectrum, which are visible as avoided level crossings in the qubit spectrum (see inset in Fig. 5.2) [Mar+05; Bil+21]. Due to the large coupling strength these TLS are believed to reside in the amorphous oxide of the Josephson junction and are known to strongly reduce the qubit coherence [Bil+20]. Furthermore, TLS can lead to time dependent fluctuations in qubit frequency and coherence times [Bre+17; Sch+19; Kli+18].

Due to close proximity of the qubits and their flux bias coils in sample A (see Fig. 5.1), magnetic crosstalk can not be completely suppressed with circuit design. In this work, a calibration scheme of Ref. [Yan+20] is used to compensate for this effect and to allow for independent and individual frequency control. The following description of the scheme is taken from [Bre+21].

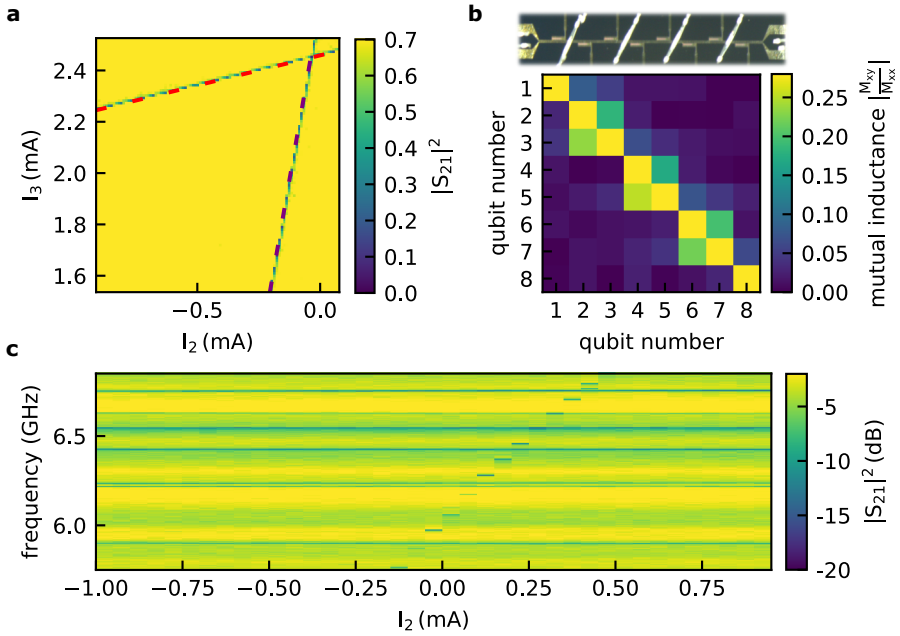

Figure 5.3: (a) Transmission $|S_{21}|^2$ at 6 GHz, while I_2 and I_3 are changed. Slopes of the measured qubit traces are proportional to M_{23}^{-1} and M_{32}^{-1}. (b) Mutual inductance matrix $\mathbf{M}$ between the bias coils and the qubits. The placement of the on-chip bondwires explains why only every second neighbours have large crosstalk. (c) Transmission measurement with qubit 2 being tuned, while crosstalk calibration is used. Horizontal lines are the other 7 qubits, not changing their frequency.[2]

The fluxes ($\Phi_1 ... \Phi_8$) applied to the SQUIDs are related with the applied currents via the mutual inductance matrix $\mathbf{M}$:

$$\begin{pmatrix} \Phi_1 \\ \Phi_2 \\ \Phi_3 \\ \Phi_4 \\ \Phi_5 \\ \Phi_6 \\ \Phi_7 \\ \Phi_8 \end{pmatrix} = \begin{pmatrix} M_{11} & M_{12} & M_{13} & M_{14} & M_{15} & M_{16} & M_{17} & M_{18} \\ M_{21} & M_{22} & M_{23} & M_{24} & M_{25} & M_{26} & M_{27} & M_{28} \\ M_{31} & M_{32} & M_{33} & M_{34} & M_{35} & M_{36} & M_{37} & M_{38} \\ M_{41} & M_{42} & M_{43} & M_{44} & M_{45} & M_{46} & M_{47} & M_{48} \\ M_{51} & M_{52} & M_{53} & M_{54} & M_{55} & M_{56} & M_{57} & M_{58} \\ M_{61} & M_{62} & M_{63} & M_{64} & M_{65} & M_{66} & M_{67} & M_{68} \\ M_{71} & M_{72} & M_{73} & M_{74} & M_{75} & M_{76} & M_{77} & M_{78} \\ M_{81} & M_{82} & M_{83} & M_{84} & M_{85} & M_{86} & M_{87} & M_{88} \end{pmatrix} \begin{pmatrix} I_1 \\ I_2 \\ I_3 \\ I_4 \\ I_5 \\ I_6 \\ I_7 \\ I_8 \end{pmatrix} \tag{5.2}$$

The mutual inductance matrix elements M_{xy} can be extracted by observing the transmission through sample A at a fixed frequency. Simultaneously, the frequency of two qubits x and y are sweeped through this observation frequency by tuning

[2] Subfigures (b) and (c) are adapted from Ref. [Bre+21].

the currents I_x and I_y (Fig. 5.3(a)). The observation frequency of 6 GHz is chosen such that the qubits have a steep flux-dispersion. It is assumed that the qubit frequencies are proportional to the flux in their coils, which is satisfied for not too large frequency changes. Eq. 5.2 gives:

$$\text{const} = \Phi_x = M_{xx} I_x + M_{xy} I_y \quad \rightarrow \quad I_y = -\frac{M_{xx}}{M_{xy}} I_x + \frac{\Phi_x}{M_{xy}} \tag{5.3}$$

$$\text{const} = \Phi_y = M_{yy} I_y + M_{yx} I_x \quad \rightarrow \quad I_x = -\frac{M_{yy}}{M_{yx}} I_y + \frac{\Phi_y}{M_{yx}} \tag{5.4}$$

Therefore, by fitting the slopes of the two qubit lines visible in this measurement, the mutual inductance matrix elements $\frac{M_{xy}}{M_{xx}}$ and $\frac{M_{yx}}{M_{yy}}$ can be extracted. In case of an 8-qubit chip, all 28 possible combinations between two coils have to be measured and fitted. The extracted mutual inductance matrix (with each element normalized to the diagonal element of its line) for the 8-qubit chip is shown in Fig. 5.3(b). The figure shows that only the nearest neighbor coupling goes beyond 10% of the self-inductance. The crosstalk is only large for every second pair of neighbors, due to the specific placement of the on-chip bond-wires on this sample. As soon as the mutual inductance matrix is known, the crosstalk can be compensated by setting a compensation current to all seven other coils, while one qubit is effectively tuned. If, for example, qubit 2 is effectively tuned, the compensation currents for all other coils can be calculated by solving the following system of linear equations:

$$\begin{pmatrix} 0 \\ 0 \\ 0 \\ 0 \\ 0 \\ 0 \\ 0 \end{pmatrix} \stackrel{!}{=} \begin{pmatrix} \Phi_1 \\ \Phi_3 \\ \Phi_4 \\ \Phi_5 \\ \Phi_6 \\ \Phi_7 \\ \Phi_8 \end{pmatrix} = \begin{pmatrix} M_{11} & M_{12} & M_{13} & M_{14} & M_{15} & M_{16} & M_{17} & M_{18} \\ M_{31} & M_{32} & M_{33} & M_{34} & M_{35} & M_{36} & M_{37} & M_{38} \\ M_{41} & M_{42} & M_{43} & M_{44} & M_{45} & M_{46} & M_{47} & M_{48} \\ M_{51} & M_{52} & M_{53} & M_{54} & M_{55} & M_{56} & M_{57} & M_{58} \\ M_{61} & M_{62} & M_{63} & M_{64} & M_{65} & M_{66} & M_{67} & M_{68} \\ M_{71} & M_{72} & M_{73} & M_{74} & M_{75} & M_{76} & M_{77} & M_{78} \\ M_{81} & M_{82} & M_{83} & M_{84} & M_{85} & M_{86} & M_{87} & M_{88} \end{pmatrix} \begin{pmatrix} I_1^{\text{comp}} \\ I_2 \\ I_3^{\text{comp}} \\ I_4^{\text{comp}} \\ I_5^{\text{comp}} \\ I_6^{\text{comp}} \\ I_7^{\text{comp}} \\ I_8^{\text{comp}} \end{pmatrix} \tag{5.5}$$

Figure 5.3(c) shows the applied compensation procedure. While only qubit 2 is effectively tuned, all seven other qubits don't change their frequency. The residual crosstalk is estimated to be below 0.1 %.

5.3 Qubit Characterization

5.3.1 Extraction of Γ_{1D} and γ_{10}

The decoherence and relaxation rates (Γ_{1D}, γ_{10}, Γ_{nr}) of the individual qubits are obtained by measuring their resonance fluorescence at a certain frequency ω_{10},

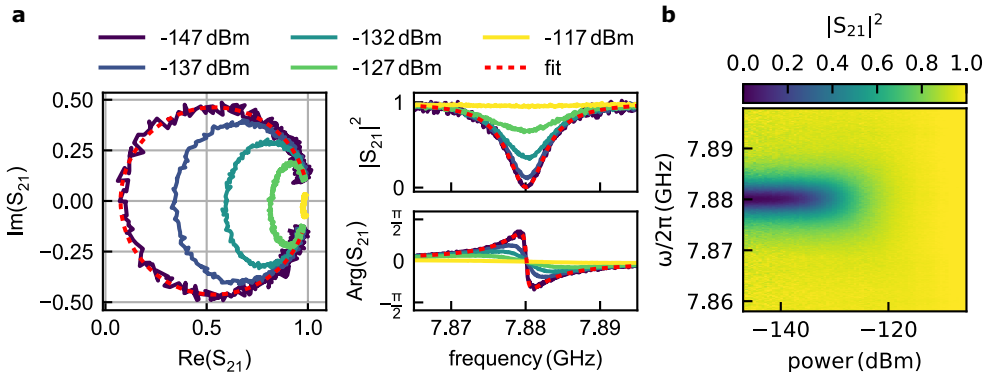

Figure 5.4: Measured resonance-fluorescence of qubit 1 at different probe powers P. (a) Red dashed line is a best fit of Eq. 3.11 to the measured complex S_{21} at low powers, giving access to the qubit decoherence rates. The asymmetry in the line shape of the single qubit resonance due to interference with the microwave background is removed following the procedure in Ref. [Pro+15]. (b) Saturation of qubit 1 with increasing powers.

Table 5.1: Summary of individual qubit parameters of sample A.

Parameter	Q1	Q2	Q3	Q4	Q5	Q6	Q7	Q8
$f_{10}^{\max}$ (GHz)	8.097	7.900	8.088	8.114	8.115	7.95	8.066	8.136
$f_{10}^{\min}$ (GHz)	3.029	3.091	2.912	2.986	2.970	2.936	2.588	2.484
m (%)	15.6	17.0	14.5	15.0	14.9	15.3	11.8	10.7
$\frac{\alpha}{2\pi}$ (MHz)	-283	-279	-273	-275	-267	-281	-273	-276
$\frac{E_J}{E_C}$ [3]	110	107	117	116	123	107	117	116
$\Gamma_{1D}/2\pi$ (MHz) [4]	5.8	7.1	7.1	8.0	7.23	5.8	5.7	4.6
$\gamma_{10}/2\pi$ (MHz) [4]	3.1	3.8	3.8	4.5	4.0	3.3	3.3	2.9
$\Gamma_{nr}/2\pi$ (MHz) [4]	0.24	0.31	0.29	0.48	0.38	0.45	0.48	0.56
Ext. Coeff. (%) [4]	99.4	99.4	99.4	98.7	99.1	98.2	97.9	96.2

while the other seven qubits are far detuned. The experimentally observed transmission coefficient S_{21} shown in Fig. 5.4 is in good agreement with Eq. 3.11. In the limit of low probe powers (here $P \approx -147\,\mathrm{dBm}$) far below the single photon regime ($\hbar\omega_{10}\Gamma_{1D} \approx -126\,\mathrm{dBm}$), a circle fitting routine of Ref. [Pro+15] is used to fit the measured complex transmission data to Eq. 3.11. This gives direct access to the rates Γ_{1D}, γ_{10} and Γ_{nr}, which are listed in detail in Tab. 5.1. On average $\Gamma_{1D}/2\pi \approx 6.4\,\mathrm{MHz}$, $\gamma_{10}/2\pi \approx 3.6\,\mathrm{MHz}$ and $\Gamma_{nr}/2\pi \approx 400\,\mathrm{kHz}$ are found at frequencies close to the upper sweet spot of the qubits, which corresponds to extinction coefficients of $\approx 99\,\%$.

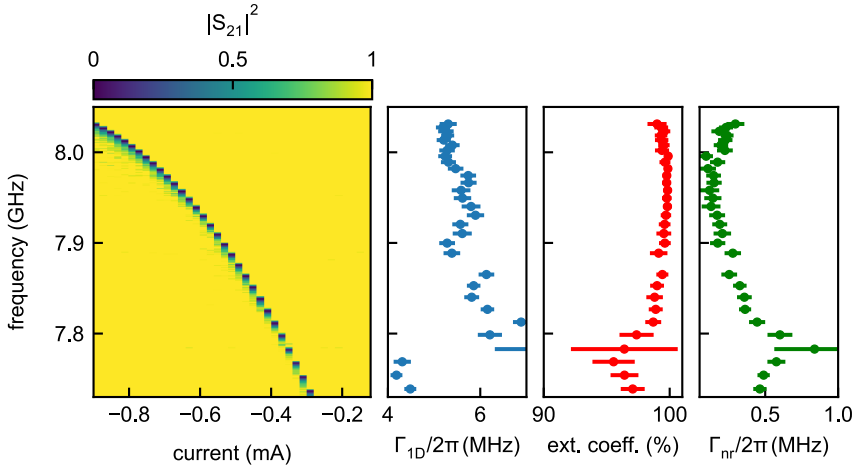

Figure 5.5: Frequency dependence of decoherence rates Γ_{1D} and Γ_{nr} of qubit 1 close to the upper sweet spot, where all experiments of this work are conducted. The frequency dependence of Γ_{1D} is caused by standing waves in the cryostat, resulting in frequency dependent coupling strengths of the qubit. The non-radiative decoherence Γ_{nr} (or the according extinction coefficient) increases (decreases) for qubit frequencies further away from the sweet spot, due to increasing susceptibility to flux-noise [Hut+17].

Fig. 5.5 shows the frequency dependence of the qubit decoherence and relaxation rates in the upper part of the qubit dispersion close to the upper flux sweet spot. With decreasing frequency, the flux dispersion becomes steeper, which results in an increased non-radiative decoherence rate Γ_{nr} (or decreasing extinction coefficient), due to increased susceptibility to flux noise [Hut+17]. Therefore, all of the following experiments are performed at frequencies close to the upper sweet spot. The radiative relaxation rate Γ_{1D} shows a strong frequency dependence, which is however not in agreement with the theoretical scaling $\Gamma_{1D} \propto \omega_{10}^2$ of Eq. 3.15. The observed behavior is most likely caused by standing waves in the microwave background of the cryostats wiring, which lead to frequency and spacially dependent variations of the qubit-waveguide coupling strength [Loo14].

5.3.2 Calibration of Absolute Power and Extraction of γ_{20}

To quantitatively evaluate the measured data, it is crucial to know how much of the applied power of the microwave sources at room temperature reaches the qubits

[3] Measured at the upper sweet spot f_{10}^{max}.
[4] Here, the listed coherence rates are obtained for all qubits at 7.898 GHz.

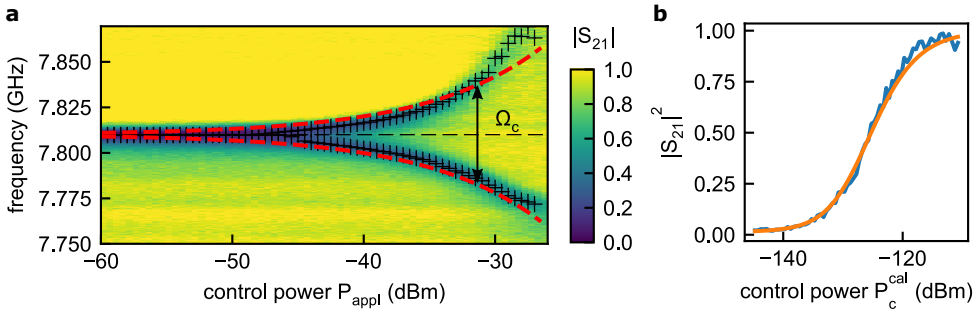

Figure 5.6: (a) The Autler-Townes splitting of qubit 2 is used for calibration of absolute power. P_{appl} is the power set at the microwave generator, driving the $2 \rightarrow 1$-transition of the qubit. Black crosses mark the center of the dressed state resonances. The red dashed line is a fit of the splitting to $\Omega_c = a\sqrt{P_{\text{appl}}}$, which is used to calibrate the on-chip power P_c. (b) $|S_{21}|^2$ on resonance with the $0 \rightarrow 1$-transition of qubit 2 in dependence on the control power P_c^{cal}. The orange line is a fit to Eq. 5.11, giving access to γ_{20}.

at the base plate of the cryostat. A rough estimate of the total attenuation of the microwave line going to the sample can be made by measuring it with a VNA when the cryostat is not in use and at room temperature (here $\approx -85\,\text{dB}$ from $3 \times 20\,\text{dB}$ attenuators and additional cable and insertion losses, compare Sec. 4.3.1). This value might however change significantly when the cryostat is cold and at the same time the simple measurement scheme of the attenuation is not applicable anymore. To resolve this issue, typically the qubit itself is used as a power-sensor. Here, a calibration protocol is used, employing the Autler-Townes splitting (ATS) [Hön+20], which is analogous to the ac-Stark shift calibration in cQED [Sch+05].

The measured ATS of qubit 2 is shown in Fig. 5.6. Since the splitting between the dressed states is exactly given by the Rabi strength of the control tone Ω_c, it can be used for calibration of the power P_c. Generally, the Rabi strength Ω_{j+1j} of the $j+1 \rightarrow j$-transition of a transmon coupled to a single mode is given by (compare Sec. 2.3.3):

$$\hbar\Omega_{j+1j} = \mu_{j+1j} V = 2e\frac{C_c}{C_\Sigma} \langle j+1|\hat{n}|j\rangle \, V \approx 2e\frac{C_c}{C_\Sigma}\sqrt{j+1}\left(\frac{E_J}{8E_c}\right)^{1/4} V_{\text{rms}} \tag{5.6}$$

The dipole moment of the corresponding transition is denoted by μ_{j+1j}, $V_{\text{rms}} = V/\sqrt{2}$ is the root-mean square voltage of the incoming wave, and $P_{j+1j} = \frac{V_{\text{rms}}^2}{Z_0} = \frac{V^2}{2Z_0}$ is the corresponding power. The rate of incoming photons in the transmission line is given by:

$$\nu = \frac{P_{j+1j}}{\hbar\omega_{j+1j}} = \frac{V_{\text{rms}}^2}{Z_0\hbar\omega_{j+1j}} = \frac{\hbar\Omega_{j+1j}^2}{Z_0\omega_{j+1j}2\mu_{j+1j}^2} \tag{5.7}$$

With the relaxation rate Γ_{1D} of Eqs. 3.15, 3.16, this can be written as:

$$\nu = \frac{\Omega_{j+1j}^2}{2(j+1)\Gamma_{1D}} \tag{5.8}$$

In case of the ATS, the $2 \rightarrow 1$-transition is driven with a control tone. For this specific case, the control Rabi-strength Ω_c is associated with Ω_{21} and following connection between the latter and the incident power P_c holds:

$$P_c = \frac{\Omega_c^2}{4\Gamma_{1D}}\hbar\omega_{21} \tag{5.9}$$

By measuring and fitting the single-qubit ATS, as shown in Fig. 5.6(a) with a simple $\Omega_c = a\sqrt{P_{appl}}$ law, the calibration factor b between applied power P_{appl} and the correct incident on-chip power P_c ($P_c = bP_{appl}$) is then given by:

$$b = a^2\frac{\hbar\omega_{21}}{4\Gamma_{1D}} \tag{5.10}$$

It is noted that the obtained calibration constants for the power are only valid at the specific qubit frequency, which was also used in the calibration. This is due to the fact that the radiative decay rate Γ_{1D} of the qubit depends on frequency (see Sec. 5.3.1). In the following experiments, calibrated powers are marked with the index *cal*. For all experiments where exact knowledge of power is not needed, the power is estimated with the approximate attenuation of the microwave cables of $-85\,\mathrm{dB}$.

Once the power is calibrated, the decoherence rate γ_{20} of the $2 \rightarrow 0$-transition can be extracted by using the same ATS measurement. If the control and probe tone are both on resonance with the transitions, the transmission coefficient of Eq. 3.26 for a three-level system simplifies to:

$$S_{21}(\omega_{10}) = 1 - \frac{\frac{\Gamma_{1D}}{2\gamma_{10}}}{1 + \frac{\Omega_c^2}{4\gamma_{20}\gamma_{10}}} = 1 - \frac{\frac{\Gamma_{1D}}{2\gamma_{10}}}{1 + \frac{4\Gamma_{1D}}{4\gamma_{20}\gamma_{10}\hbar\omega_c}P_c} \tag{5.11}$$

When Γ_{1D} and γ_{10} are known, fitting Eq. 5.11 to the measured trace gives an estimate for γ_{20} (Fig. 5.6(b)). As discussed in Sec. 3.1.2 and Appendix. B.3, the decoherence rate γ_{20} has got a lower limit even the absence of pure dephasing and non-radiative relaxation, as well as $\Gamma_{20} = 0$, which is set by the radiative relaxation rate Γ_{2D} of the $2 \rightarrow 1$-transition ($\gamma_{20} \geq \Gamma_{2D}/2$). Combined with the scaling of the radiative relaxation rates of Eq. 3.16, this implies $\gamma_{20} \geq \Gamma_{1D}$. The measured rates for γ_{20} (see Tab. 5.2) for Sample A partially don't fulfill this theoretical limit. This can be explained with the strong frequency dependence of the radiative relaxation rates $\Gamma_{j\mathrm{D}}$, which is observed experimentally (Sec. 5.3.1).

5.4 Metamaterial Properties

The results on the collective properties of the 8 qubit metamaterial which are presented in this section follow Ref. [Bre+21].

5.4.1 Spectroscopy of Polariton Excitations

In order to investigate the mode properties of the 8 qubit metamaterial in the single excitation sector and their dependence on the number N of resonant qubits, first the qubits are consecutively tuned to a common resonance frequency ω_{10}. The probe power is kept well below the single photon regime ($P \ll \hbar\omega_{10}\Gamma_{1D}$) to avoid saturation of the qubits and multiple excitations in the metamaterial. Here, the frequency $\omega_{10}/2\pi \approx 7.898\,\mathrm{GHz}$ is used, which corresponds to the upper sweet spot of qubit 2. Among the other qubits it has got the smallest frequency. Choosing ω_{10} to be as close as possible to the upper sweet spot is beneficial to minimize non-radiative decoherence rates Γ_{nr} of the qubits due to flux-noise (see Sec. 5.3.1). The measured transmission coefficient $|S_{21}|$ is shown in Fig. 5.7. While for $N = 1$ only a single resonance is observed (see Sec. 3.1.1), the system becomes multi-mode for $N > 1$ and the super- and subradiant polariton modes start to emerge. The subradiant polariton modes are visible as peaks in the transmission spectrum below ω_{10} created by Fano-type interference (see Sec. 3.2.3, [HFS16; Bre+21]). The superradiant mode is manifested as a wide dip above ω_{10}. The frequency of the modes is in agreement with the real part of the eigenfrequencies $\Re(\omega_\xi)$ obtained from H_{eff} (see Eq. 3.30 and Fig. 5.7(b)). It is noted that the calculated frequencies do not perfectly coincide with the peaks due to the Fano interference, which shifts the maximum of the peak slightly away from the actual resonance frequency [Lep+19]. For $N < 6$ only the brightest of the subradiant modes is visible, because darker modes with $\Gamma_\xi/2 < \Gamma_{nr}$ decay in the qubits before their excitation can be remitted into the waveguide and be detected. For $N \geq 6$ also the second brightest subradiant mode is visible in the transmission spectrum. Fig. 5.7(b) shows that an area of strongly suppressed transmission emerges ($|S_{21}|^2 < -25\,\mathrm{dB}$) between ω_{10} and the superradiant mode with increasing N. This stop band is the signature of an emerging polaritonic band gap, where the refractive index becomes purely imaginary as expected for any kind of periodic resonant structures [Ivc05; TL08]. For $N = 8$ the width of the bandgap is $\Delta\omega \approx 1.9\Gamma_{1D}$. Compared with the expected bandgap of $\Delta\omega = \Gamma_{1D}c/(\omega_{10}d) \approx 6.3\Gamma_{1D}$ (Eq. 3.41) of an infinite metamaterial, this places the 8 qubit array in the intermediate regime between a single atom and a fully extended crystal.

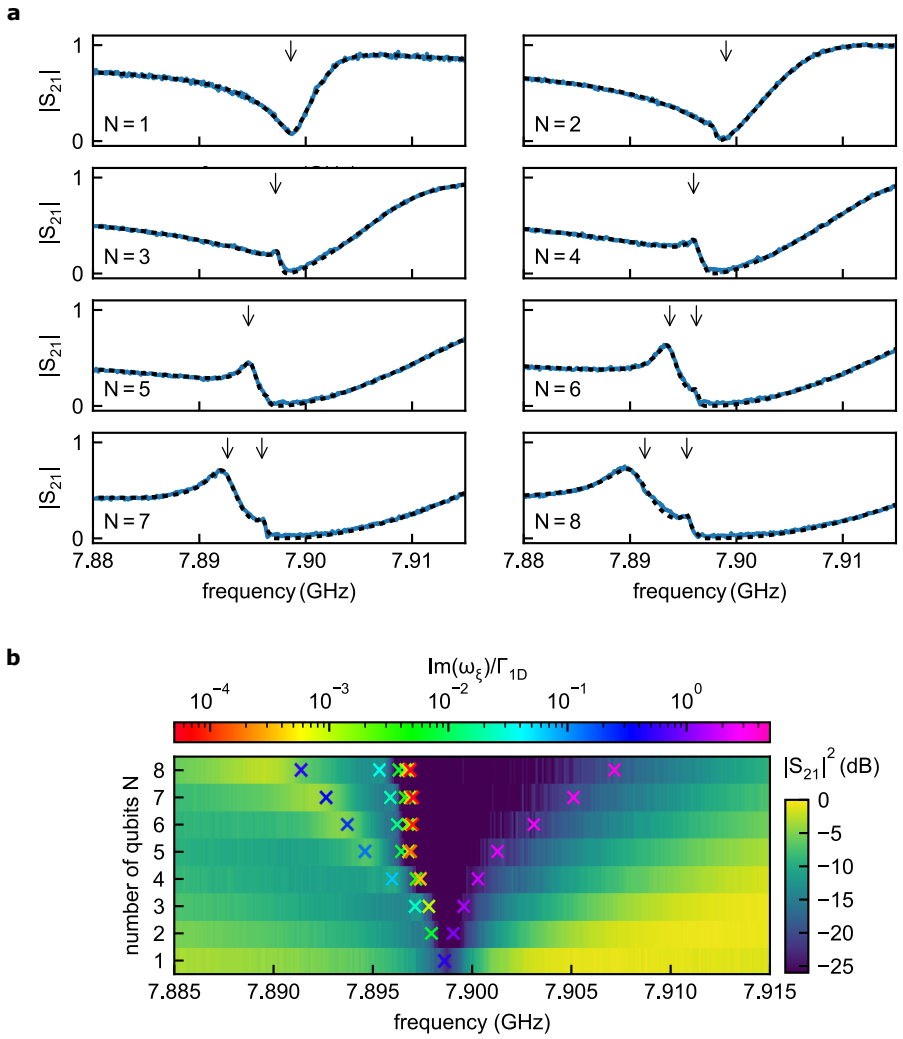

Figure 5.7: (a) Transmission coefficient $|S_{21}|$ at low powers for N resonant qubits at $\omega_{10}/2\pi \approx 7.898\,\mathrm{GHz}$. Starting from $N = 2$, a second peak emerges, associated with a subradiant polariton mode. For $N \geq 6$ also the second brightest polariton mode is visible. The black dashed line is a fit to the corresponding T-matrix model of Eq. 5.13. Black arrows mark the real part of the relevant eigenfrequencies of H_{eff} (Eq. 3.30). (b) Measured $|S_{21}|^2$ and overview of all calculated eigenfrequencies and radiative decoherence rates (here without non-radiative decay). With increasing N, an area of strongly suppressed transmission is opening up between the superradiant mode and the subradiant modes, which is a manifestation of the emerging band gap.

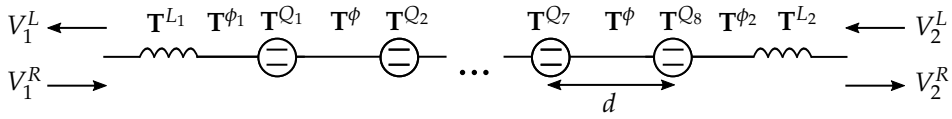

Figure 5.8: Schematic representation of the transfer matrix for a system of 8 qubits coupled to a waveguide with distance d between neighbouring qubits. An additional cable resonance is introduced to account for the asymmetric line shape as measured in the experiment. $\mathbf{T}^{L_i}$ introduce partial reflectance due to impedance mismatches from inductances in the waveguide.

The overall line-shape of the observed resonances is asymmetric due to interference with standing waves, caused by impedance mismatches in the cabling of the cryostat [Kha+12]. In order to fit the observed transmission coefficient of Fig. 5.7(a) to a T-matrix model (see Sec. 3.2.3), the cable resonance has to be incorporated. This is done by introducing two inductances acting as semi-transparent mirrors before and after the qubit array (compare Fig. 5.8). In the cryostat they could represent impedance mismatches of the bond wires between the qubit chip and the cryostats wiring. The T-Matrix $\mathbf{T}^L$ of an inductance reads:

$$\mathbf{T}^L = \begin{pmatrix} 1 + \frac{i\omega L}{2Z_0} & \frac{i\omega L}{2Z_0} \\ \frac{-i\omega L}{2Z_0} & 1 - \frac{i\omega L}{2Z_0} \end{pmatrix} \tag{5.12}$$

The total inductance matrix of the 8 qubit system is therefore given by:

$$\mathbf{T}_{\text{tot}} = \mathbf{T}^{L_2}\mathbf{T}^{\phi_2}\mathbf{T}^{Q_8}\mathbf{T}^{\phi}...\mathbf{T}^{\phi}\mathbf{T}^{Q_2}\mathbf{T}^{\phi}\mathbf{T}^{Q_1}\mathbf{T}^{\phi_1}\mathbf{T}^{L_1} \tag{5.13}$$

All other T-matrices are defined in Sec. 3.2.3. In order to reduce the number of free parameters in the model, all qubits are assumed to have the same frequency and decoherence rates. The fits of the T-matrix model to the measured transmission coefficient for N resonant qubits is shown in Fig. 5.7(a). For $N = 8$ the best fit to the experimental data provides the radiative relaxation rate $\Gamma_{1\text{D}}/2\pi = 6.4\,\text{MHz}$ and decoherence rate $\gamma_{10}/2\pi = 3.4\,\text{MHz}$, which is in good agreement with the average of all individual rates of Tab. 5.1.

5.4.2 Lifetime Scalings of Subradiant Polariton Modes

When probed in reflection, the subradiant modes are visible as dips (compare Fig. 5.9). It can be generally shown that the lineshape around each polariton resonance is described by a Lorentzian function [TL08; Ase+17]. Here, an additional *skew* is introduced in the Lorentzian function $L(\omega)$ to account for the asymmetric background:

$$L(\omega) = a + b(\omega - \omega_0) - \frac{c}{1 + \frac{4(\omega-\omega_0)^2}{(\Gamma_\xi + 2\Gamma_{\text{nr}})^2}} \tag{5.14}$$

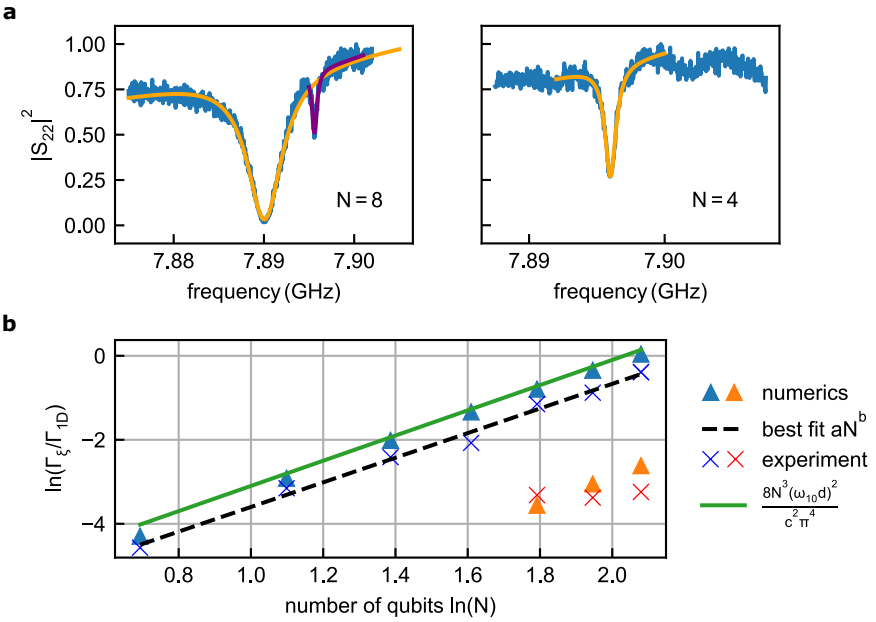

Figure 5.9: (a) The measured reflectance data $|S_{22}|^2$ shows the subradiant polariton modes as pronounced dips. Lorentzian fits are used to extract their radiative relaxation rates Γ_ξ (here shown exemplary for $N = 8, 4$). (b) Extracted Γ_ξ for all visible subradiant modes. The brightest subradiant mode shows a scaling $\Gamma_\xi \propto N^3$ with the number of resonant qubits. A best fit to the experimental data gives a power law with the exponent $b = 2.93 \pm 0.13$ and therefore confirms the predicted scaling of Ref. [Bre+21].

By fitting the observed dips to Eq. 5.14, the radiative relaxation rate Γ_ξ of the visible polaritons can be accessed. Some exemplary fits are shown in Fig. 5.9(a). All extracted rates of the brightest and second brightest subradiant modes are shown in Fig. 5.9(b). The rates are in agreement with the rates obtained from the eigenvalues $2\Im(\omega_{10})$ of H_{eff}. Small deviations are caused by imperfect qubit tuning and interference with the microwave background. Furthermore, the brightest of the subradiant states follows the analytically obtained scaling $\Gamma_\xi = 8N^3(\omega_{10}d)^2/(c^2\pi^4)$ (see Appendix B.5 and Ref. [Bre+21]). A fit to a power law $\propto N^b$ gives an exponent of $b = 2.93 \pm 0.13$ and thus confirms the predicted scaling. The obtained scaling of the brightest subradiant mode with N is the complementary asymptotic of the extensively discussed universal $\Gamma_\xi \propto N^{-3}$ scaling of the most subradiant state [TL08; Alb+19; Ase+17; DHB20]. A remarkable property of this scaling is that it is independent how the wQED system is physically realized (e.g. one dimensional or three dimensional open space). It occurs universally in so called 1D boundary dissipation models, where dissipation happens only at the ends of the qubit chain [Alb+19].

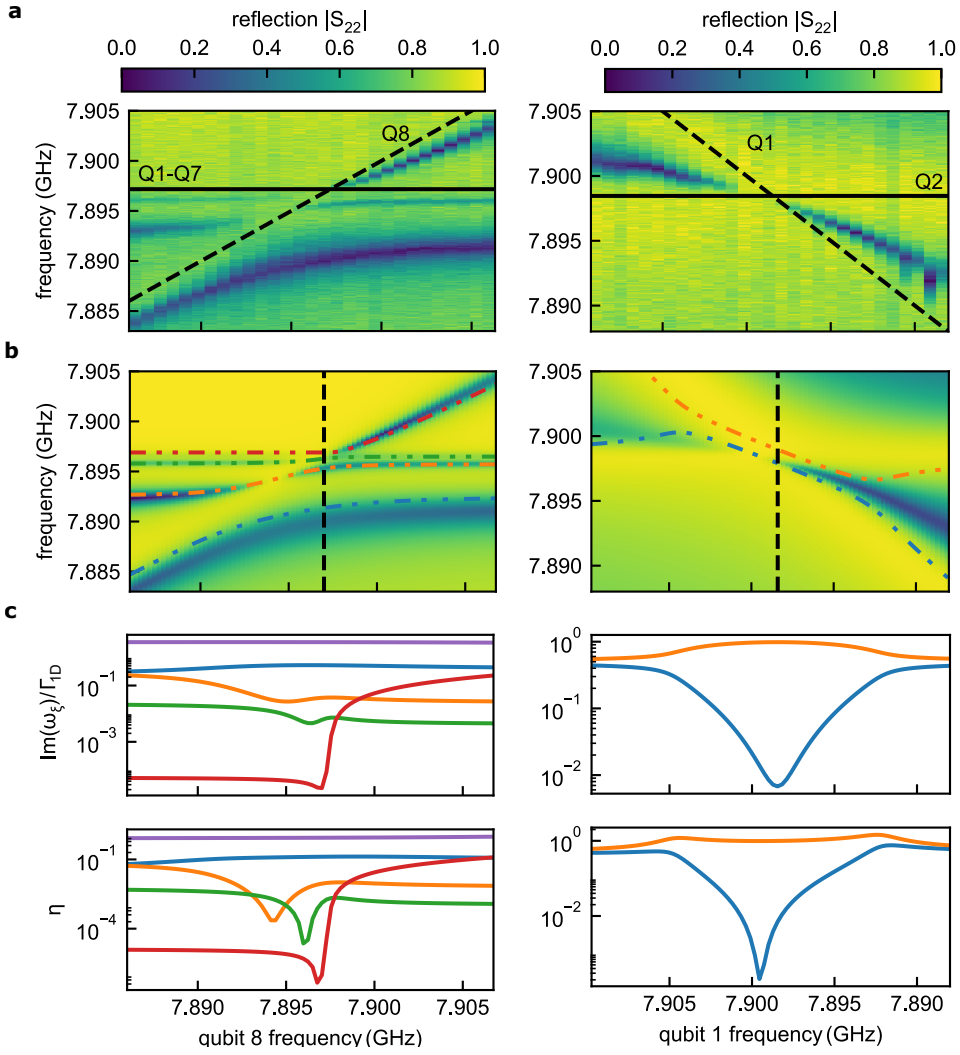

Figure 5.10: (a) Measured reflection coefficient $|S_{22}|$ for the off-resonant situation, where qubit 8 is tuned through the collective resonance of qubit 1 to 7 at $\omega_{10} = 7.897\,\mathrm{GHz}$ (right column: qubit 1 is tuned through qubit 2). The subradiant polariton modes are visible as dips in $|S_{22}|$. (b) The corresponding T-matrix calculation reproduces the measured reflection coefficient. Colored lines mark the relevant calculated eigenfrequencies $\Re(\omega_\xi)$ of Eq. 3.30. (c) Calculated decoherence rates $\Im(\omega_\xi)$ and mode-overlap η (Eq. 3.33) explain the visibility of the subradiant modes in the reflection experiment.

5.4.3 Mode Visibility and Off-resonant Qubit Frequencies

The mode-spectrum in the single excitation regime can be further elaborated by studying the off-resonant situation, where the qubits have a finite detuning. Fig. 5.10(a) shows the measured reflection coefficient $|S_{22}|$ when an individual qubit (at frequency ω_0) is tuned through an ensemble of already resonant qubits ($\omega_{10}/2\pi \approx 7.897\,\mathrm{GHz}$), using the qubits tunability. For large detunings $|\omega_{10} - \omega_0| \gg \Gamma_{1D}$ (not shown in Fig. 5.10(a)) the polariton modes of the ensemble and the mode of the qubit are not hybridized. For smaller detunings an additional partially hybridized subradiant mode appears, which becomes for zero detuning the brightest of the subradiant modes. The level repulsion between the observed collective states is caused by the residual exchange type interaction between the qubits, due to their finite distance d. The measured results are in good agreement with the T-matrix model and the calculated eigenvalues ω_ξ from H_{eff} (compare Fig. 5.10(b)). The subradiant states in Fig. 5.10(a) show several blind spots, where they turn completely dark. This occurs when the frequency of the detuned qubit matches the frequency $\Re(\omega_\xi)$ of an eigenstate of the full system. This can be explained by the Fano-like interferences between the detuned qubit resonance and the modes of the resonant qubits, which are analyzed in more detail in the Appendix B.6. Additionally, for the blind spots close to the common resonance ω_{10}, the overlap η (Eq. 3.33) between the wave driving the qubit chain and the polariton mode vanishes and therefore turns them completely dark (compare Fig. 5.10). Similar observations have been made also in cavity QED with two interacting qubits via a cavity bus [Fil+11].

5.4.4 Power Saturation and Collective Autler-Twones Splitting

As indicated in Sec. 3.1.1, the elastic scattering properties of light in the single excitation sector alone does not allow for a discrimination between two-level systems and harmonic oscillators. Also for multiple qubits, the elastic scattering in the single excitation sector as observed above is similar to an array of coupled harmonic oscillators [Mir+18]. The simplest way to experimentally establish a discrimination between them is to increase the probe power beyond the single photon regime (see Fig. 5.11). Analogous to the single qubit case (treated in Sec. 3.1.1), the collective resonance of several qubits saturates with increasing power (Fig. 5.11(a)). It is highlighted that in fact all spectroscopic features are saturable, including the polariton modes and the band gap, in agreement with the prediction of saturability of materials made of qubits [Ast+10a]. Whereas for a single qubit the saturation is well described by Eq. 3.11 (see Fig. 5.11(b)), to the best of the author's knowledge no such analytical solution exists to describe the

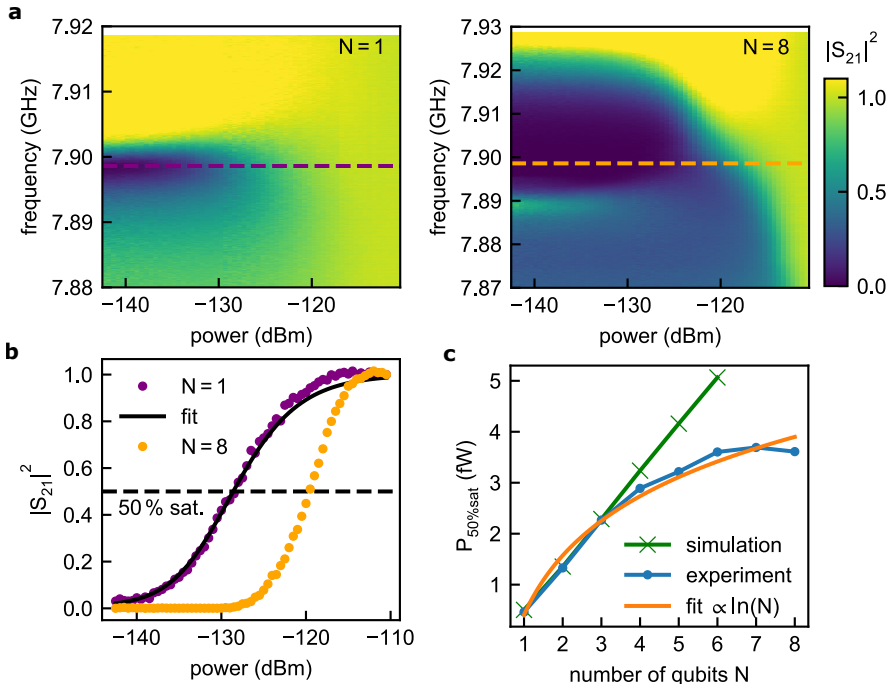

Figure 5.11: (a) Left: saturation of qubit 1 with power. Right: saturation of the $N = 8$ collective resonance. All features are saturable, including the super- and subradiant modes and the band gap. (b) Saturation of the transmission coefficient at the collective resonance frequency $\omega_{10}/2\pi \approx 7.898\,\mathrm{GHz}$. For the $N = 8$ qubit resonance, more power is needed to saturate the array. The $N = 1$ saturation is well described by Eq. 3.11, whereas to the best of the author's knowledge for the $N = 8$ data no analytical solution exists. (c) Scaling of the power required to saturate $|S_{21}|^2$ to 50% with qubit number N. The measured scaling is best described by $\propto \ln(N)$, whereas the numerical model of Ref. [Lal+13] predicts a linear scaling.

saturation of N qubits. It is found, that in general the power needed to saturate N resonant qubits grows monotonously with N. Here, $P_{50\%\,\mathrm{sat}}$ is introduced as figure of merit to quantify the saturation power needed to saturate the transmission $|S_{21}|^2$ to 0.5. Fig. 5.11(c) shows the measured scaling of $P_{50\%\,\mathrm{sat}}$ with N, which is best described by $\ln(N)$. This experimental result is in conflict with a numerical master equation simulation of an array of N two-level systems based on Ref. [Lal+13], which predicts a linear scaling. Due to an exponentially growing Fock-Liouville space with N, this simulation was on a desktop computer only feasible up to $N = 6$. A potential reason for the failure of the numerical model is the approximation of the qubits as perfect two-level systems, wheras the used transmon qubits are in fact only weakly anharmonic. Thus, multi-photon transitions to higher qubit levels could have significant contributions to the observed saturation [Bra+15].

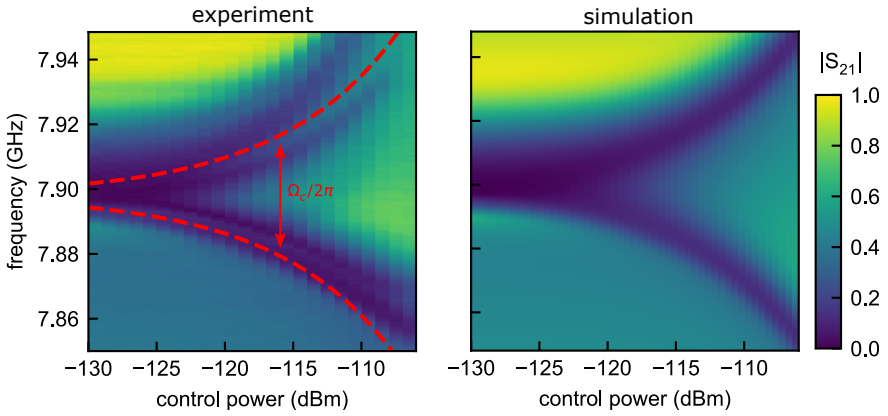

Figure 5.12: Left: measured collective $N = 8$ Autler-Townes splitting. With increasing control-power, the band gap splits and a band with finite transmission is opening up around the common resonance frequency, demonstrating active control over the band structure. The red-dashed line is a fit to the splitting given by the Rabi-strength Ω_c of the control-tone. Right: a T-matrix simulation reproduces the measured collective ATS. Small deviations arise due to imperfections in the qubit tuning and slightly differing qubit anharmonicities. Used parameters: $\frac{\omega_{10}}{2\pi} = 7.898\,\text{GHz}$, $\Gamma_{1D}/2\pi = 6.4\,\text{MHz}$, $\gamma_{10}/2\pi = 3.4\,\text{MHz}$, $\gamma_{20}/2\pi = 11.1\,\text{MHz}$.

Beyond saturation with power, the quantum non-linearity of the qubit metamaterial can be unambiguously shown by demonstrating the collective Autler-Townes splitting (ATS). As discussed in detail in Sec. 3.1.2 and 3.2.3, this effect necessarily requires an anharmonic three-level system. In order to observe it for N resonant qubits, they are first tuned to a collective resonance frequency $\omega_{10}/2\pi \approx 7.898\,\text{GHz}$. Then, an additional microwave control tone with frequency $\omega_{10} + \alpha$ is applied to drive the $1 \rightarrow 2$-transition of the qubits. For the anharmonicity $\alpha/2\pi = -275\,\text{MHz}$ is used, corresponding to an average of the values for α listed in Tab. 5.1. Similar to the single qubit ATS (compare Fig. 5.6(a)), here the collective ATS is observed for up to $N = 8$ (see Fig. 5.12). Again, the splitting between the two dressed collective resonances is given by the Rabi-strength Ω_c of the control tone. As shown in Fig. 5.12, the observed collective ATS is in good agreement with the calculation based on the T-matrix of Eqs. 5.13, 3.26. Minor deviations are caused by the slightly differing anharmonicities between the qubits (compare Tab. 5.1). In the band structure picture it is the two dressed states $|\pm\rangle$ (Eq. 3.28) of the individual qubits giving rise to two independent Bloch bands of the collective ATS [WS10]. The collective ATS provides a useful tool to actively control the band structure and with it the optical response of the qubit metamaterial via an external microwave control tone. To the best of the author's knowledge, this is the first demonstration of a collective ATS in superconducting wQED. A direct application of the presented collective ATS is an extension of the single-photon router of Ref. [Hoi+11] to

the few-photon domain: due to the demonstrated higher saturation powers of the collective qubit resonance, the band gap region is even in the few photon limit still perfectly reflecting. Moreover, the collective resonance has a strongly enhanced extinction coefficient and can thus compensate for reduced extinction coefficients, which reduce the routing performance in the single qubit case. Due to the enhanced width of the band gap compared to the single qubit line width, it is also possible to route microwave pulses with a larger spectral width. Another even more relevant application of the collective ATS is the creation of slow light and quantum memories which will be discussed in the next section.

5.5 Slow Light

Controlling the speed of light in artificially structured media, slowing it down and eventually stopping it, has recently gotten into the focus of quantum information processing. It is crucial for controlling and synchronizing the flow of information [Kro+19] and for the realization of long living quantum memories [LST09]. As introduced in Sec. 3.2.4, a reduction of the group velocity of light v_g can be generally achieved by engineering steep dispersion profiles (or conversely flat bands in the band structure). Simultaneously, it is desirable to have a large bandwidth at high transmittance and low group velocity dispersion in the spectral region of slow light [Bab08].

Here two approaches to create slow light are realized with the eight qubit metamaterial: first, the collective ATS, which can be controlled by a microwave tone, is used to demonstrate the effect. It is in close resemblance to EIT-based slow light, which has been extensively studied with cold atoms (including a reduction of v_g to 17 m/s [Hau+99] and atoms coupled to nano-fibers [Gou+15]). However, this effect is not realized in superconducting wQED to this date. Second, the slow light effect is achieved by using the qubits as tunable dispersive elements and arranging them in detuned collective resonances as proposed in Ref. [She+07]. By doing so, a similar band-structure as in the ATS case can be engineered [Yan+04]. Even though this effect is purely classical, it can be shown that analogously to EIT, slow light and quantum memory protocols can be realized [She+07; YF04]. This approach is similar to classical slow light photonic crystal waveguides, where the steep dispersion near the photonic bandgap is exploited [Bab08] or it is introduced with local resonant elements [MF19]. This approach was used in superconducting circuits to realize a slow-light waveguide based on an array of superconducting resonators [Mir+18].

Table 5.2: Measured[5] individual qubit properties around 7.812 GHz. All other relevant qubit parameters are listed in Tab. 5.1

Parameter	Q1	Q2	Q3	Q4	Q5	Q6	Q7	Q8
$\Gamma_{1D}/2\pi$ (MHz)	7.3	9.5	11.3	13.9	14.5	14.6	12.1	11.9
$\gamma_{10}/2\pi$ (MHz)	4.2	5.3	6.7	8.4	8.1	8.1	6.7	7.2
$\Gamma_{nr}/2\pi$ (MHz)	0.52	0.56	1.0	1.36	0.83	0.83	0.65	1.3
$\gamma_{20}/2\pi$ (MHz)[6]	8.7	8.3	-	6.7	5.6	6.2	-	5.7
Ext. Coeff %	98.4	98.9	97.7	97.4	99.0	99.0	99.1	96.8

5.5.1 Dressed State based Slow Light

The collective ATS, as presented in Sec. 5.4.4, gives in the infinite lattice case rise to a band structure, which is shown in Fig. 3.10. In the following the effect of the flat band around the $1 \rightarrow 0$-transition on the group velocity v_g is probed.

The data presented in this section was measured in a separate cooldown compared to the data shown in Sec. 5.4. Due to the specific appearance of strongly coupled TLS in the qubit spectrum, in the cooldown for the slow light experiment it was not possible to find a common TLS-free resonance frequency for all 8 qubits near the upper flux sweet spot. Therefore, the following experiment was conducted with a maximum of $N = 7$ (qubits 1-7) around a common resonance frequency of $\omega_{10}/2\pi \approx 7.812\,\text{GHz}$. The relevant qubit coherence rates at this frequency are listed in Tab. 5.2.

The $N = 7$ collective ATS is shown in Fig. 5.13. In contrast to the ideal case of vanishing $2 \rightarrow 0$-decoherence, the transmission $|S_{21}|$ around ω_{10} is smaller than unity. The finite decoherence rate $\gamma_{20}/2\pi \approx 6.8\,\text{MHz}$ suppresses the quantum interference between the excitation pathways in the three-level system and thus dampens the effect of EIT. This is most dramatic in the limit of low control tone strengths ($\Omega_c < \beta\gamma_{10}$[7], considered as EIT regime). This indicates that the observed transparency window and its dispersive feature in Fig. 5.13 is mainly caused by the collective resonances of the ATS and quantum interference effects from EIT are only playing a secondary role. In contrast to experiments with Λ-type three-level systems, which can show almost perfect EIT [Hau+99], the comparably large

[5] Data measured after a thermal cycle of the cryostat compared to the slow light measurements.

[6] γ_{20} was not accessible for all qubits at the given frequency, due to spurious TLS distorting the single qubit ATS.

[7] $\beta\gamma_{10} = (N^2 - 1)\phi\gamma_{10}/3$ is the approximate width of the band gap for the N qubit resonance. $\beta\gamma_{10}$ is used as an approximation for the line width of the dressed resonances of the collective ATS which is in the single qubit case just given by Γ_{1D}.

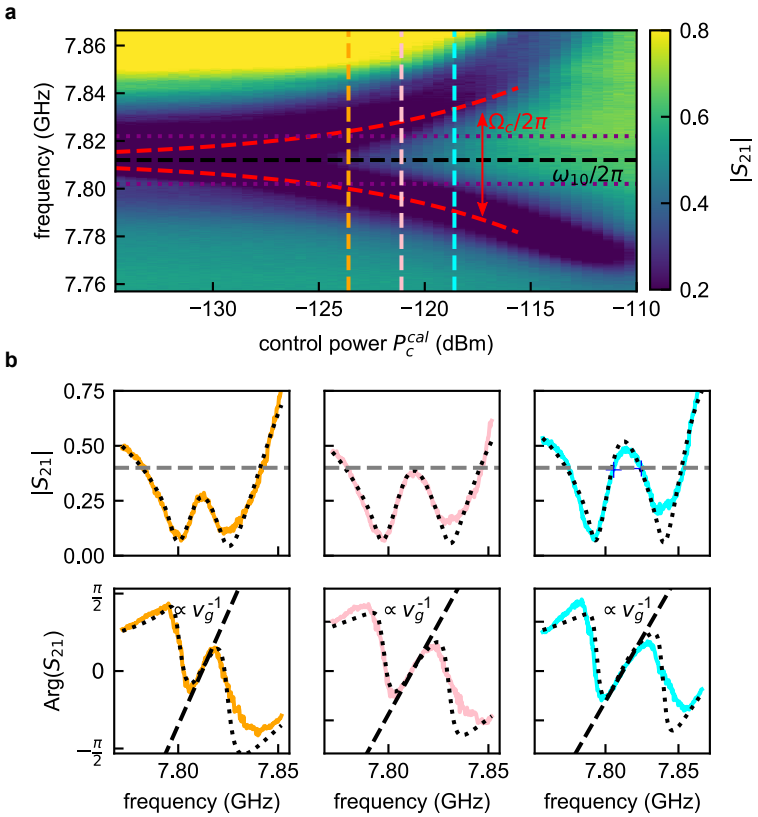

Figure 5.13: (a) Measured collective ATS for $N = 7$. With increasing control tone power P_c^{cal}, the dressed collective resonances are split by the corresponding Rabi-strength Ω_c. Vertical dashed purple lines mark a spectral width of 20 MHz of the transparency window. (b) Absolute transmission $|S_{21}|$ and phase $\mathrm{Arg}(S_{21})$ of the $N = 7$ collective ATS for selected control powers. For small control powers quantum interference from EIT is suppressed and with it also the transmission around ω_{10} due to finite $2 \to 0$-decoherence ($\gamma_{20}/2\pi \approx 6.8$ MHz). In agreement with Eq. 5.15, the slope of the phase roll-off in the transparency window, controlled by Ω_c, dictates the expected group velocity v_g. Black dotted lines represent best fits to the T-matrix model. Vertical grey dashed lines mark transmission threshold according to $|S_{21}| \approx \exp(-1/2)|S_{21}^{max}(\omega_{10})|$, used for the determination of the transparency window bandwidth.

decoherence rate γ_{20} is a consequence of the ladder-type level structure of the used transmon qubits (see section 3.1.2 and Appendix B.3), which can therefore only show incomplete EIT [YRZ01]. To quantitatively discriminate between ATS and EIT in the observed splitting, the information theoretic method based on Akaike's information criterion (AIC) as proposed in Ref. [ADS11] can be used. However, the method can here not directly be applied to the experimental data since it is asymmetric due to interference with the microwave background. Moreover, even under ideal circumstances the collective ATS shows intrinsic asymmetric features due to internal reflectance and interference effects. If applied to a calculated single qubit ATS, based on Eq. 3.26 and an average of the measured qubit parameters in Tab. 5.2, the AIC yields that the transmission is described by almost 100 % certainty by the ATS[8].

The phase of the transmission signal $\mathrm{Arg}(S_{21})$ in the center of the transparency window features a steep roll-off which indicates low group velocities (compare Fig. 5.13(b)). Quantitatively, the expected group velocity can be calculated from the measured phase-gradient [Ase+17; LS12]:

$$v_\mathrm{g} = \left(\frac{1}{(N-1)d} \frac{d\mathrm{Arg}(S_{21}(\omega))}{d\omega} \right)^{-1} \Bigg|_{\omega=\omega_{10}} \tag{5.15}$$

The inferred time delays $\tau = (N-1)d/v_\mathrm{g}$ (traversal times) from Eq. 5.15 and the experimental data from the $N = 7$ ATS of Fig. 5.13 are plotted in Fig. 5.14(c). In agreement with a numerical T-matrix calculation, it can be seen that the expected traversal time, or similarly the effective group index n_g[9], can be tuned over a large range with the applied control power $P_\mathrm{c}^\mathrm{cal}$. Contrary to the textbook case of EIT in the limit of $\gamma_{20} \approx 0$, where $\tau \propto 1/\Omega_\mathrm{c}^2$ diverges for small Ω_c (compare Eq. 3.45), it can be seen that τ is approaching a maximum of 15 ns ($n_\mathrm{g} \approx 1900$) at $P_\mathrm{c}^\mathrm{cal} \approx -124\,\mathrm{dBm}$ before it starts to decrease again for even lower control tone strengths. Similar behaviors were observed in room temperature vapor of ^{4}He [Gol+09]. In order to obtain an analytical expression for v_g in the limit of finite γ_{20}, Eq. 3.43 can be approximated in the limits for large and small control tone strengths Ω_c, translating to $\phi \gg \xi$ and $\phi \ll \xi$. For the first case Eq. 3.43 simplifies to:

$$k \approx (\frac{\omega}{c}) - \frac{ir}{1+r}\frac{1}{d} \tag{5.16}$$

$$\frac{dk}{d\omega} \approx \frac{1}{c} - \frac{1}{d}\frac{d}{d\omega}\left(\frac{ir}{1+r}\right) \tag{5.17}$$

[8] In the relevant control power range for the slow light experiment: $P_\mathrm{c}^\mathrm{cal} = -130... - 110\,\mathrm{dBm}$

[9] The group index n_g is given with respect to the vacuum speed of light $c_0 \approx 3 \cdot 10^8\,\mathrm{m/s}$ and not with respect to the bare waveguide speed of light ($c \approx 1.2 \cdot 10^8\,\mathrm{m/s}$)

For the second case, i.e. $\phi \ll \xi$, Eq. 3.43 simplifies to:

$$k^2 \approx -\frac{2\phi\xi}{d^2} \tag{5.18}$$

$$\frac{dk}{d\omega} \approx \frac{d\xi}{d\omega}\frac{\sqrt{-\phi/2}}{\sqrt{\xi}d} \tag{5.19}$$

The expected time delay τ for a traversal of an N qubit metamaterial in the center of the transparency window can then be computed by:

$$\tau = \frac{(N-1)d}{v_g} = (N-1)d\Re\left(\left.\frac{dk}{d\omega}\right|_{\omega=\omega_{10}}\right) \tag{5.20}$$

Inserting Eqs. 5.17 and 5.19 in 5.20 then gives:

$$\tau(\omega_{10},\Omega_c) \approx \begin{cases} \frac{(N-1)\Gamma_{1D}(2\Omega_c^2-8\gamma_{20}^2)}{(4\Gamma_{nr}\gamma_{20}+\Omega_c^2)^2} & \phi \gg \xi \\ \frac{(N-1)\Gamma_{1D}(2\Omega_c^2-8\gamma_{20}^2)}{(4\Gamma_{nr}\gamma_{20}+\Omega_c^2)^{3/2}}\sqrt{\frac{\phi}{8\Gamma_{1D}\gamma_{20}}} & \phi \ll \xi \end{cases} \tag{5.21}$$

In the limit of $\gamma_{20} \approx 0$, the limit $\phi \gg \xi$ is always fulfilled and the corresponding expression in Eq. 5.21 reduces to the formula of textbook EIT (see Eq. 3.45). As shown in Fig. 5.14(c), the asymptotic for $\phi \gg \xi$ matches the measured time delays accurately. In the opposing limit for $\phi \ll \xi$, only qualitative agreement is found, which is most likely caused by the fact that Eq. 5.21 is derived based on a band structure calculation but the experimental system is finite. Nevertheless, the calculation accurately predicts the existence of a maximum in τ and its corresponding control power P_c^{cal}.

To test the spectroscopically inferred time-delays τ in Fig. 5.14(c), pulsed measurements in the time-domain are required. Here, an FPGA based heterodyne microwave setup is used to generate and detect the pulses (see Sec. 4.3.2). The used pulses have a Gaussian envelope $A(t)$ with a temporal width of $\sigma = 50\,\text{ns}$:

$$A(t) = A\exp\left(-\frac{(x-\mu)^2}{2\sigma^2}\right) \tag{5.22}$$

To avoid saturation of the qubits, the amplitude A of the pulses is chosen such that the power corresponding to the maximum A of the pulse is still well below the single photon regime $P < \hbar\omega_{10}\Gamma_{1D} \approx -124\,\text{dBm}$. Fig. 5.14(a) shows a measured reference pulse with a center frequency of $\omega_{10}/2\pi = 7.812\,\text{GHz}$, which is sent through the 8 qubit metamaterial with all qubits far detuned. The pulse is detected by the measurement electronics separately in its I and Q component, which is at that point still modulated with the intermediate frequency ($f_{IF} = 115\,\text{MHz}$). Thereafter, the complex signal is digitally down-converted to dc, lowpass-filtered with a 5th order

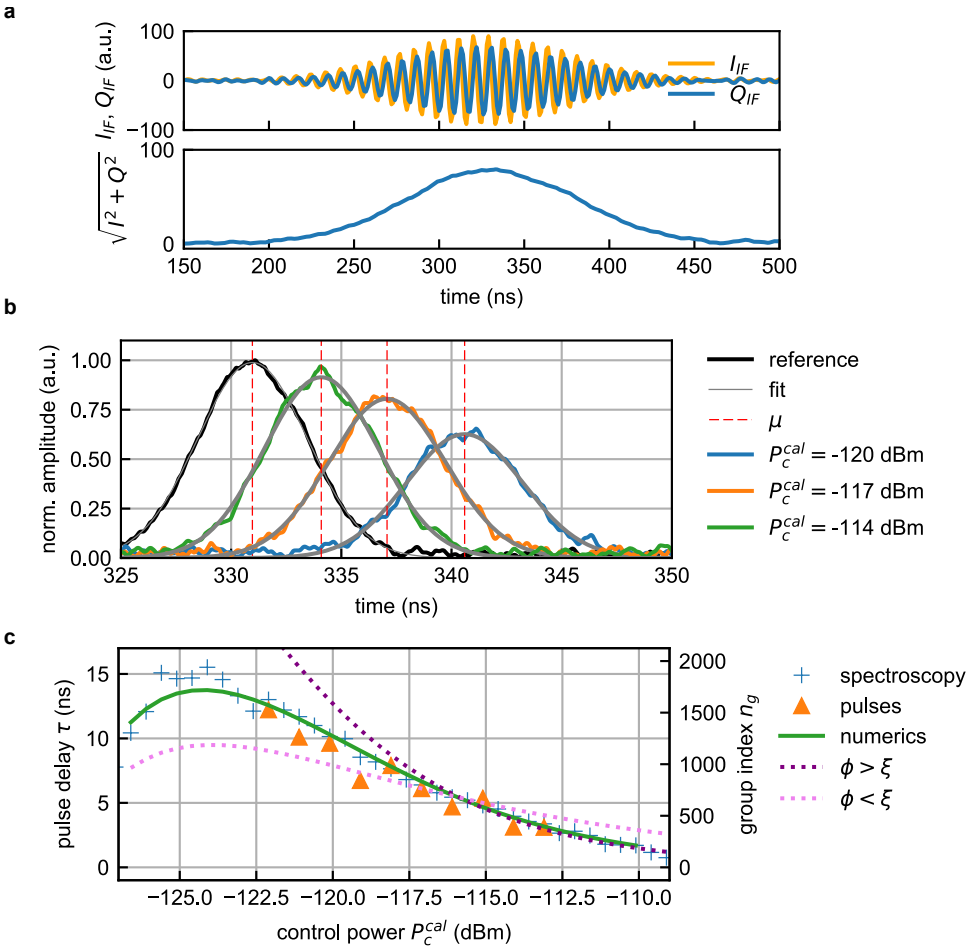

Figure 5.14: (a) Top: detected Gaussian pulse in the I and Q quadrature at the intermediate frequency of $f_{\mathrm{IF}} = 115\,\mathrm{MHz}$. Bottom: digitally down-converted and low-pass filtered amplitude of the pulse. (b) Measured pulses after propagation through the transparency window of the collective ATS with $N = 7$ for different control tone powers $P_{\mathrm{c}}^{\mathrm{cal}}$. With decreasing $P_{\mathrm{c}}^{\mathrm{cal}}$, the pulses get more delayed compared to a reference pulse with far detuned qubits. For better visibility, the pulses are compressed by a factor of 20, with their maximum at time μ staying at the original position. (c) Measured pulse delays τ compared to the reference. The obtained delays of pulsed time-resolved measurements agree with the delay derived from the spectroscopic data of Fig. 5.13 and with the numerical simulation based on the T-matrix method. Purple and pink lines indicate the two asymptotes of Eq. 5.21 in the limit of a strong and weak control tone.

Butterworth filter with 115 MHz cutoff and its amplitude is computed[10](compare Fig. 5.14(a)). Following the reference measurement, the experiment is repeated for the $N = 7$ collective ATS at different control powers (Fig. 5.14(b)). The pulses have again a center frequency of $\omega_{10}/2\pi = 7.812\,\mathrm{GHz}$, corresponding to the center of the transparency window. The time delay τ of the measured pulses is extracted by the difference of their temporal center μ (extracted by a fit of the detected pulse amplitude to Eq. 5.22) and the one of the reference measurement. The extracted time delays (Fig. 5.14(c)) agree with the numerical model and the spectroscopically inferred delays. Due to the finite spectral width of the used pulses ($1/\sigma = 20\,\mathrm{MHz}$, see purple lines in Fig. 5.13(a)) and the width of the transparency window, the minimal accessible control tone power is limited to $P_\mathrm{c}^\mathrm{cal} \approx -122.5\,\mathrm{dBm}$. This leads to a maximal accessible delay of $\tau \approx 12\,\mathrm{ns}$ ($n_\mathrm{g} \approx 1500$) in the time-resolved measurements.

As shown in Fig. 5.14(b), the amplitude of the detected pulses decreases for increasing delay τ. This is in agreement with the measured transmission coefficient in Fig. 5.13 and is caused by the finite $2 \to 0$-decoherence rate γ_{20}, spoiling the quantum interference of EIT [FIM05]. Following Ref. [NWX11], a coefficient ι can be calculated to characterize the efficiency of the slow light effect. It is defined as an energy ratio of the incoming and outgoing pulse, which reduces for Gaussian pulses to their squared amplitude ratio:

$$\iota = \frac{E_\mathrm{out}}{E_\mathrm{in}} = \frac{A_\mathrm{out}^2}{A_\mathrm{in}^2} \tag{5.23}$$

At maximal delay ($P_\mathrm{c}^\mathrm{cal} \approx -122.5\,\mathrm{dBm}$) an efficiency of $\iota = 16\,\%$ is found. Furthermore, a delay-bandwidth product (DBP) can be defined, which is given by the product of the time delay τ and the bandwidth of the transparency window[11]. The DBP measures how well a light pulse fits spatially inside the metamaterial [Ase+17]. For the $N = 7$ ATS, a DBP of 0.2 is found, indicating that a general on-demand storage and retrieval memory can not be efficiently realized. Nevertheless, the demonstrated slow light effect can be used as a tunable pulse retarder or fixed-delay quantum memory [Ras+19] at the given efficiency ι.

[10]It is noted that the complex detection in terms of I and Q components is not necessarily required for the experiments shown here, because only the amplitude of the signal is used. A separate digital down-conversion on I and Q is used to compensate for oscillating components in the signal amplitude due to imperfections in the IQ-Mixer.

[11]The bandwidth is measured between the frequencies above and below ω_{10}, where the transparency decreases to $|S_{21}| \approx \exp(-1/2)|S_{21}^\mathrm{max}(\omega_{10})|$ (see Fig. 3.9(b)). $|S_{21}^\mathrm{max}(\omega_{10})|$ is the maximal value of the transmission in the center of the transparency window for large P_c, which is here smaller than 1 due to interference with the microwave background.

While the presented experiment marks the first demonstration of EIT/ATS-based slow light in a superconducting wQED system, it is limited in its performance by the large decoherence rate γ_{20}, which is inherently large for ladder-type three-level systems [YRZ01] (see also Sec. 3.1.2 and Appendix B.3). Dramatic improvements can therefore be expected by using Λ-type three-level systems, such as flux or Fluxonium qubits, biased far from flux degeneracy [Joo+10].

5.5.2 Dispersion Engineered Slow Light

As pointed out in Refs. [She+07; Yan+04; YF04] an EIT-like band structure can also be engineered by using the qubits directly as dispersive elements without the need for a third level or an additional microwave control tone. In order to realize the required band structure, again a one-dimensional metamaterial realized by an array of densely spaced qubits is used. However now, a unit cell consists (in contrast to the case in Eq. 3.39) of two qubits at frequencies f_1 and f_2 (compare Fig. 5.15(a)). In the infinite lattice limit, this results in a similar band structure to the ATS/EIT-metamaterial shown in Fig. 3.9(b). As derived in Refs. [She+07; Yan+04; YF04], this gives not only rise to slow light because of a flat central band, but also allows for quantum memory protocols and even negative group indices. Instead of using a second microwave control tone to regulate the slope of the central band and the group velocity v_g, it is now the detuning between qubits f_1-f_2, changed with the local flux bias lines.

Fig. 5.15(b) shows the measured transmission coefficient S_{21} for qubits 2,4,6,8 being tuned to frequency $f_2 = 7.882\,\mathrm{GHz}$ and qubits 1,3,5,7 being tuned to a varied frequency f_1. The measured S_{21} resembles that of the collective ATS resonance (Fig. 5.13): a transparency window with a steep phase roll-off, sandwiched between two resonances. In good agreement with the T-matrix calculation, both collective four qubit resonances show their brightest subradiant state as pronounced peaks a few Megahertz below f_1 and f_2. Using Eq. 5.15, the expected time-delay τ and group index n_g in the center of the transparency window ($(f_1 + f_2)/2$) can be derived from $\mathrm{Arg}(S_{21})$ (see Fig. 5.15(c)). Analogously to the previous section, pulsed measurements with $\sigma = 50\,\mathrm{ns}$ pulses are used to validate the inferred delays in the time domain. In agreement with numerics, delays up to $\tau = 17\,\mathrm{ns}$ ($n_g = 1850$) are found, which can be tuned with the detuning between f_1 and f_2. For a group index of $n_g \approx 1500$, where in the ATS-case an efficiency of $\iota = 16\,\%$ was measured, here an efficiency of $\iota = 50\,\%$ is found. The over three times higher efficiency is possible since γ_{20} is not reducing the transmittivity of the transparency window. The numerical T-matrix model furthermore suggests, that for smaller detunings

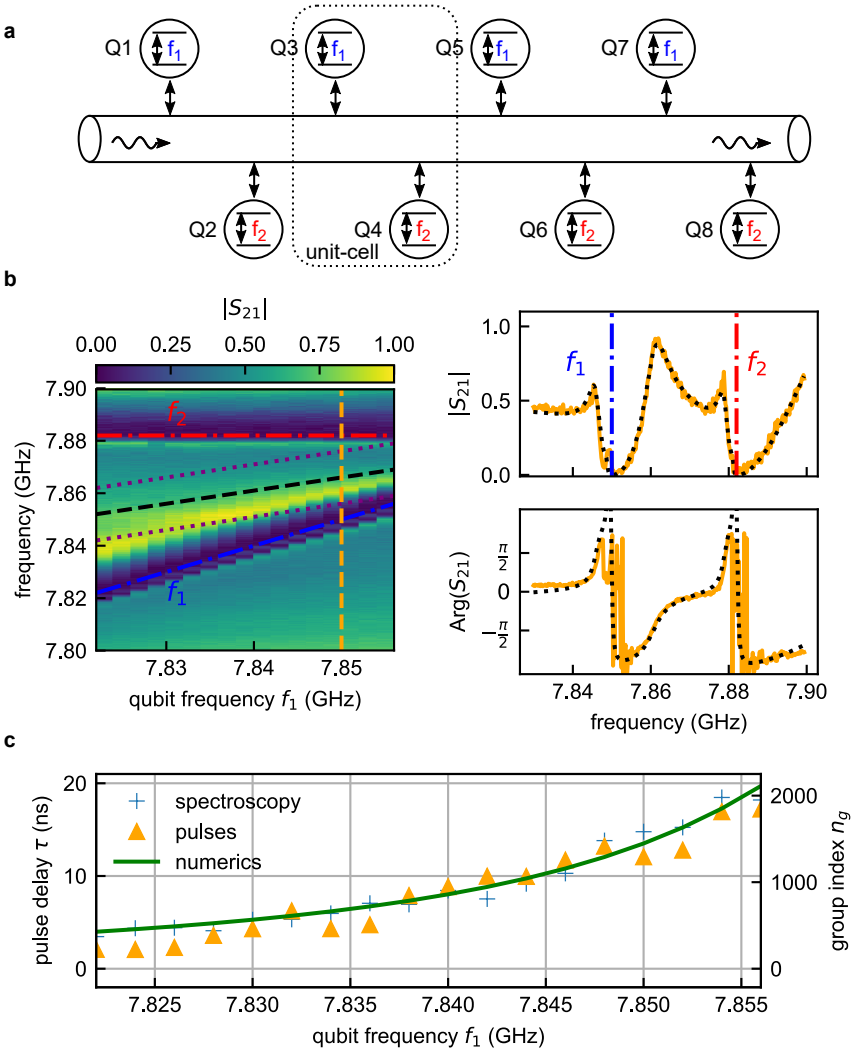

Figure 5.15: (a) Sketch of the used qubit configuration for the dispersion engineered slow light. Every second qubit is tuned to a frequency f_1 and every other second to f_2, creating an ATS like band structure. (b) Left: transmission $|S_{21}|$ for a pair of detuned collective four qubit resonances at frequencies f_1 and f_2. The black dashed line indicates the center frequency of the transparency window and the purple dotted lines show a corresponding bandwidth of 20 MHz as required by 50 ns pulses. Right: $|S_{21}|$ for a detuning of $f_2 - f_1 = 32$ MHz. Similar to the ATS, the phase $\mathrm{Arg}(S_{21})$ features a steep roll-off between the two resonances, indicating a strongly reduced group velocity v_g. The black dashed line marks the best fit to the corresponding T-Matrix. (c) Both, time-resolved pulsed measurements and spectroscopy data indicate in agreement with numerics pulse delays up to 17 ns. This corresponds to extreme effective group indices of $n_g \approx 1850$.

$f_1 - f_2$ than shown in Fig. 5.15, time delays of up to 46 ns ($n_g \approx 5000$) can be reached with the dispersion engineering method and the 8 qubit metamaterial.

Since only the first two qubit energy levels are used, the demonstrated slow light effect with an engineered dispersion partially mitigates the problem of damping and is therefore of higher efficiency as in the EIT/ATS case. Even though the realization of a quantum memory is theoretically possible in dispersion engineered media [She+07], it is experimentally significantly harder to realize since it requires fast control of multiple qubits simultaneously. This is in contrast to the EIT case, where the memory can be controlled with just an additional microwave control tone. The dispersion engineering approach however offers a much wider variability and more complicated band structures can be created readily. For example instead of only a flat center band, several bands with tailored group velocities can be engineered, which route on demand pulses at different frequencies, resembling the ideas of multi-color EIT [Wan+14].

5.6 Artificial Disorder and Anderson Localization

As discussed in the previous sections, the resonant situation is the most relevant for practical applications of qubit metamaterials like quantum memories [LS12], multi-port photon routers [Hoi+13], and the generation of non-classical light [FZB14]. In sample A 8 qubits can easily be brought to resonance with the demonstrated near crosstalk-free individual qubit control. If however large scale metamaterials with hundreds of qubits should be realized, local frequency control might not be feasible anymore. In contrast to atomic qubits, non-tunable superconducting qubits will unavoidably show a certain degree of frequency disorder [Kre+20]. The random scattering in disordered materials is known to give rise to an exponential suppression of transmission as soon as the disorder is greater than a certain critical value, known as Anderson localization [And58]. The exponential decay of transmission is described by the dimensionless Anderson localization length ζ, which is defined in an N qubit array as [MS18]:

$$\frac{1}{\zeta} = -\frac{\langle \ln(|S_{21}|^2) \rangle}{N} \tag{5.24}$$

The brackets $\langle\rangle$ denote an average over different realizations of disorder. First experiments demonstrated Anderson localization with the scattering of light in semiconductor powders [Wie+97]. More recent publications showed that Anderson localization is also expected in wQED systems with either disorder in qubit frequency or position [HFS16; WS10; Mir+18; MS18].

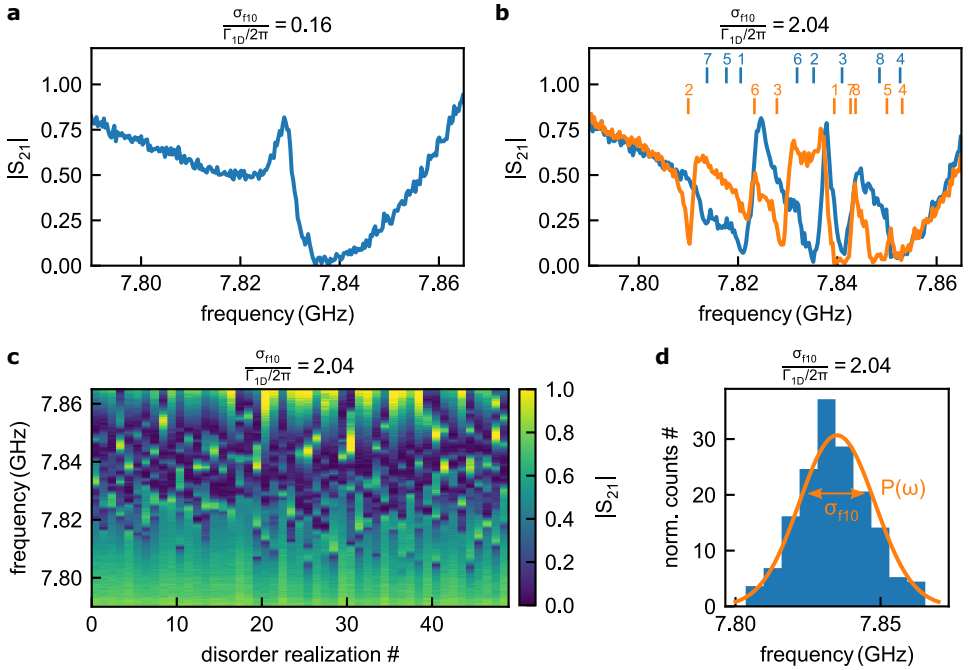

Figure 5.16: (a) Transmission $|S_{21}|$ for a random disorder realization with very small frequency spread $\sigma_{f10}/(\Gamma_{1D}/2\pi) = 0.16$, showing the features of the perfectly ordered case. (b) $|S_{21}|$ for two random disorder realizations with large frequency spread $\sigma_{f10}/(\Gamma_{1D}/2\pi) = 2.04$. Vertical numbered dashes represent the frequency of the corresponding qubit in the disorder realization. (c) Overview of 50 disorder realizations as used for the disorder averaging. (d) Histogram of all (8×50) random qubit frequencies of the data show in (c) and the corresponding Gaussian probability distribution $P(\omega)$.

Here, the frequency tunability of the eight qubit metamaterial is used to artificially introduce frequency disorder into the system to study its effect on the transmission of light and the emergence of localization effects. The experiments follow the idea of *tunable localization* as presented in Ref. [WS10]. In the following experiments always all eight qubits are used and tuned to different random frequencies ω_{10}^{i}, which are picked according to a Gaussian probability distribution $P(\omega)$:

$$P(\omega) = \frac{1}{\sqrt{2\pi}\sigma_{f10}} \exp\left(-\frac{(\omega/2\pi - f_c)^2}{2\sigma_{f10}^2}\right) \quad \text{with} \quad f_c = 7.835\,\text{GHz} \tag{5.25}$$

The strength of frequency disorder is therefore given by the frequency standard deviation σ_{f10}. Fig. 5.16 shows the measured transmission coefficient $|S_{21}|$ for different random realizations of disorder. For weak disorder ($\sigma_{f10}/(\Gamma_{1D}/2\pi) = 0.16$, Fig. 5.16(a)) the measured transmission does not differ significantly between different disorder realizations and the resonant case (Fig. 5.7). For strong disorder

($\sigma_{f10}/(\Gamma_{1D}/2\pi) = 2.04$, Fig. 5.16(b)) the line shape of the collective resonance is completely scrambled for each disorder realization. In agreement with the results of Ref. [MS18], a numerical calculation based on the T-matrix method shows that $|S_{21}|^2$ indeed decays exponentially with N as soon as frequency disorder is introduced (Fig. 5.17(d)). This is an indication of Anderson localization and motivates the computation of a corresponding localization length ζ according to Eq. 5.24. As derived in Ref. [Mir+18], it is however not only disorder giving rise to an exponential decay of the transmission coefficient with coherence length ζ_{disor}, but also the non-vanishing imaginary part of the wave vector $\Im(k)$ associated with coherence length ζ_{loss}. The latter has two main contributions: intrinsic non-radiative qubit decay $\Gamma_{\text{nr}} > 0$ (red line in Fig. 5.16(d)) and a large contribution of $\Im(k) > 0$ in the region of the polaritonic bandgap, where the metamaterial is reflective (Fig. 3.9). The measured localization length ζ is therefore given by [Mir+18]:

$$\frac{1}{\zeta} = \frac{1}{\zeta_{\text{disor}}} + \frac{1}{\zeta_{\text{loss}}} \tag{5.26}$$

Outside of the band gap region, especially in the lower polariton branch close to f_c, and for the given amount of non-radiative damping in the eight qubit metamaterial ($\Gamma_{\text{nr}}/\Gamma_{1D} \leq 0.1$), the localization length is expected to be strongly dominated by ζ_{disor} ($\zeta \approx \zeta_{\text{disor}}$).

In order to calculate the effect of localization from the created frequency disorder according to Eq. 5.24, the logarithmic average over an ensemble of disorder realization is required. For each value of σ_{f10}, 50 different disorder realizations are measured (Fig. 5.16(c) and (d)). The resulting measured dependence of ζ on disorder strength σ_{f10} is shown in Fig. 5.17(a),(b). A T-matrix simulation based on the parameters of the experiment shows qualitative agreement with the measured localization length (Fig. 5.17(c)). At low frequency disorder, significant localization[12] is only present in the region of the band gap above the center qubit frequency $f_c = 7.835\,\text{GHz}$. However, with increasing disorder σ_{f10}, ζ is also reduced in the frequency regions above and below the band gap. In the infinite lattice case in these regions $\Im(k)$ is close to zero, the observed reduction of ζ is expected to be dominated by Anderson localization [Mir+18].

To the best of the author's knowledge it was to the point of this work not rigorously shown, whether this argument still holds for short structures as in the case of the 8 qubit metamaterial. In the experiment (Fig. 5.17(b)), the most significant reduction of ζ (from $\zeta \approx 18$ to $\zeta \approx 2$) happens close to f_c at $\omega/2\pi = 7.828\,\text{GHz}$, the position of the brightest of the sub-radiant polariton modes (see Sec. 3.2.2). At

[12]Since ζ is defined by $|S_{21}|^2 \propto \exp(-N/\zeta)$, localization is considered as *strong* if $\zeta \ll 8$.

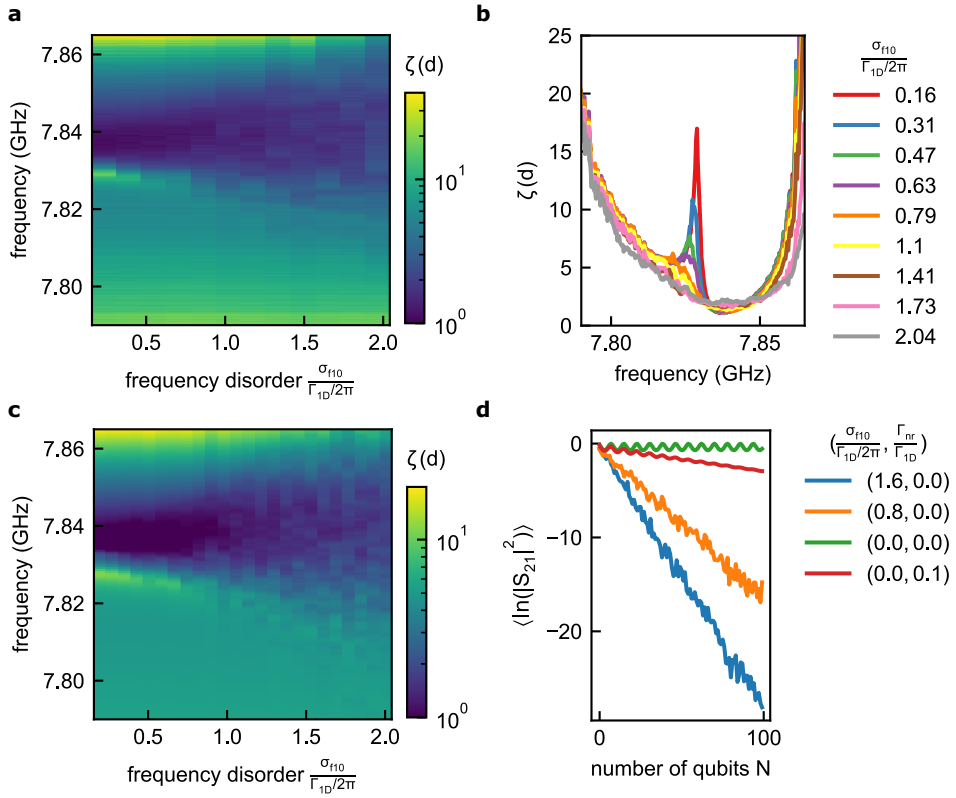

Figure 5.17: (a), (b) Measured localization length ζ for increasing frequency disorder. Each trace is based on an average over 50 different random disorder realizations. With increasing disorder the transmission below the center frequency of $\omega/2\pi = 7.835\,\mathrm{GHz}$ gets strongly suppressed. (c) Simulation based on the T-matrix reproduces the observed features of the experiment. (d) Calculation based on the T-matrix shows that the transmission is exponentially suppressed as soon as disorder is introduced, being an indication of Anderson localization (here at a frequency of $\omega/2\pi = 7.828\,\mathrm{GHz}$). Non-radiative decay $\Gamma_{\mathrm{nr}} > 0$ of the qubits introduces an additional exponential decay due to losses. Used parameters: $\Gamma_{1\mathrm{D}}/2\pi = 6.4\,\mathrm{MHz}$.

the current state of this work, it is unknown whether the suppression of single modes in finite metamaterials is a manifestation of Anderson localization or just caused by the averaging over different disorder configurations and needs further theoretical investigation. If the arguments above do also hold for short structures, which is supported by the numerics (Fig. 5.17(d)), the presented experiment is a demonstration of tunable Anderson localization as introduced in Ref. [WS10].

6 Towards Large Scale wQED Systems

This chapter provides first experimental results on a large scale wQED system consisting of 90 non-tunable transmon qubits coupled to a waveguide. Due to its size, this system is much closer to the *continuum* limit of an infinitely extended structure, than the 8 qubit metamaterial discussed in the previous section. The experimental efforts to dramatically increase system size is motivated by theoretical proposals comprising quantum metamaterials with large (infinite) qubit numbers [Rak+08; Asa+15] and the realization of an efficient quantum memory [Ase+17]. Since local frequency control is at the current state of technology not feasible for the given number of qubits, necessarily some disorder in the qubit transition frequencies is present. Therefore, first the design and fabrication requirements are addressed to minimize the amount of disorder in the metamaterial below a critical threshold to still be able to observe cooperative effects. Even though these requirements could not be fully met experimentally, the presented metamaterial features a broad band gap. Using spectral hole burning techniques [Put+16; PV09], it is shown that the latter is caused by partial homogenous broadening due to cooperative effects.

6.1 Design Considerations

Fig. 6.1 shows an overview of sample B, a metamaterial consisting of 90 transmon qubits as used for the experiments presented in this chapter. At the current state of technology, local flux control of individual qubits as used for sample A is not feasible. Using non-tunable qubits with only a single Josephson junction instead of a SQUID, introduces a spread in frequency σ_{f10}[1] between different qubits on the same chip due to varying critical currents I_c (see Sec. 4.1.2 for a detailed discussion). If the qubits are much further detuned than their linewidth Γ_{1D}, no cooperative

[1] Here, a normal distribution with standard deviation σ_{f10} for the qubit frequencies is assumed.

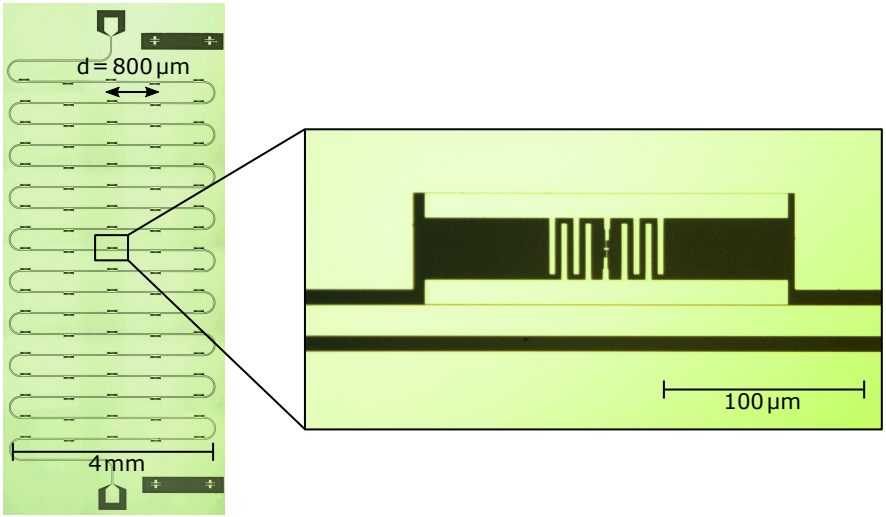

Figure 6.1: Microscopic image of sample B, consisting of 90 non-tunable transmon qubits coupled to a coplanar waveguide. The spacing between neighbouring qubits is significantly smaller than the wavelength λ, corresponding to the qubits transition frequency $d/\lambda \approx 0.033$. The overall length of the metamaterial is given by $90d \approx 3\lambda$. The qubits are spaced in close vicinity (500 nm) to the waveguide and the groundplane in order to realize the desired effective coupling capacitance $C_C \approx 17$ fF.

interaction between them is expected (see Sec. 5.4.1). Thus, the qubit linewidth Γ_{1D} sets an upper threshold for the tolerable frequency spread σ_{f10}: $\sigma_{f10} < \Gamma_{1D}/2\pi$. Using Eqs. 2.19 and 2.40, the spread σ_{f10} is related with the spread in normal state resistance σ_{R_n} by:

$$\sigma_{f10} = \sqrt{\frac{|\alpha|/(2\pi)\Delta}{4R_n e^2}}\sigma_{R_n}/R_n \tag{6.1}$$

In order to be able to observe collective effects, it is therefore desirable to decrease σ_{R_n} as far as possible and increase Γ_{1D} by strong qubit waveguide coupling (for strategies and results in decreasing σ_{R_n} see Sec. 4.1.2). Here, a realistic value for the coupling of $1/\Gamma_{1D} = 10$ ns is targeted, which translates into a relative normal resistance spread of 0.6 %. At a qubit frequency of $\omega_{10}/2\pi \approx 5$ GHz, this coupling strength results in a coupling capacitance of $C_c \approx 17$ fF (Eq. 3.15). Furthermore, to reduce the impact of disorder, the anharmonicity α of the transmon qubits is intended to be large, translating into small ratios of $E_J/E_C \approx 30$.

Similarly to sample A, a dense qubit spacing of $d = 800$ µm is chosen to have a sub-wavelength qubit spacing of a metamaterial. Despite being in the sub-wavelength limit, a twice as large value for d is chosen compared to sample A, to extend the

Table 6.1: Summary of individual qubit parameters of sample B, measured on a separate individual qubit, which was fabricated on the same wafer as sample B. The values were extracted analogously to the procedure in Sec. 5.3.1.

parameter	value
f_{10} (GHz)	4.885
$\frac{\alpha}{2\pi}$ (MHz)	-343
$\frac{E_\mathrm{J}}{E_\mathrm{C}}$	29
$\Gamma_{1\mathrm{D}}/2\pi$ (MHz)	8.6
$\gamma_{10}/2\pi$ (MHz)	5.6
$\Gamma_\mathrm{nr}/2\pi$ (MHz)	1.2
Ext. Coeff. (%)	95

total length of the structure to multiple wavelengths ($90d \approx 3\lambda$). To fit the whole metamaterial of sample B on one chip, a chip size of 10 mm $\times$5 mm is used. The waveguide is arranged in a meander shape, in order to fit all of the employed qubits to this chip size.

6.2 90 Qubit Metamaterial

In order to get an estimate for the individual parameters of the qubits used in the 90 qubit metamaterial, a single qubit coupled to a waveguide, which was fabricated on the same wafer, is characterized first. Using the same methods as in Sec. 5.3.1, the parameters listed in Tab. 6.1 are found. Moreover, the relative spread in normal resistances of the Josephson junctions is found to be $\sigma_{R_\mathrm{n}}/R_\mathrm{n} \approx 2.2\,\%$[2] (Tab. 4.2). Since these values do not meet the design goals of $\sigma_{R_\mathrm{n}}/R_\mathrm{n} < 0.6\,\%$ and $1/\Gamma_{1\mathrm{D}} = 10\,\mathrm{ns}$, the qubits in the metamaterial are expected to only partially overlap in frequency space and show cooperative effects.

The measured transmission coefficient $|S_{21}|^2$ [3] of sample B is shown in Fig. 6.2. It features a $\Delta\omega/2\pi \approx 260\,\mathrm{MHz}$ wide stop band of suppressed transmission around a center frequency of $\omega_{10}/2\pi \approx 5\,\mathrm{GHz}$. With increasing microwave power, the band gap is saturable, indicating that it is indeed created by the non-linear qubits (see

[2] The used test junctions where fabricated in the same process as sample B.

[3] It is noted that the transmission of sample B is for frequencies far away from the band gap suppressed by $\approx -15\,\mathrm{dB}$, which indicates a non-conducting interrupt of the cpw-waveguide or of the on chip bondwires. This offset is removed in the data shown in Fig. 6.2 by normalizing to the transmission at high microwave powers. Numerical simulations based on the T-Matrix indicate that the interrupt (modelled as a capacitance) does not have a large influence on the overall lineshape.

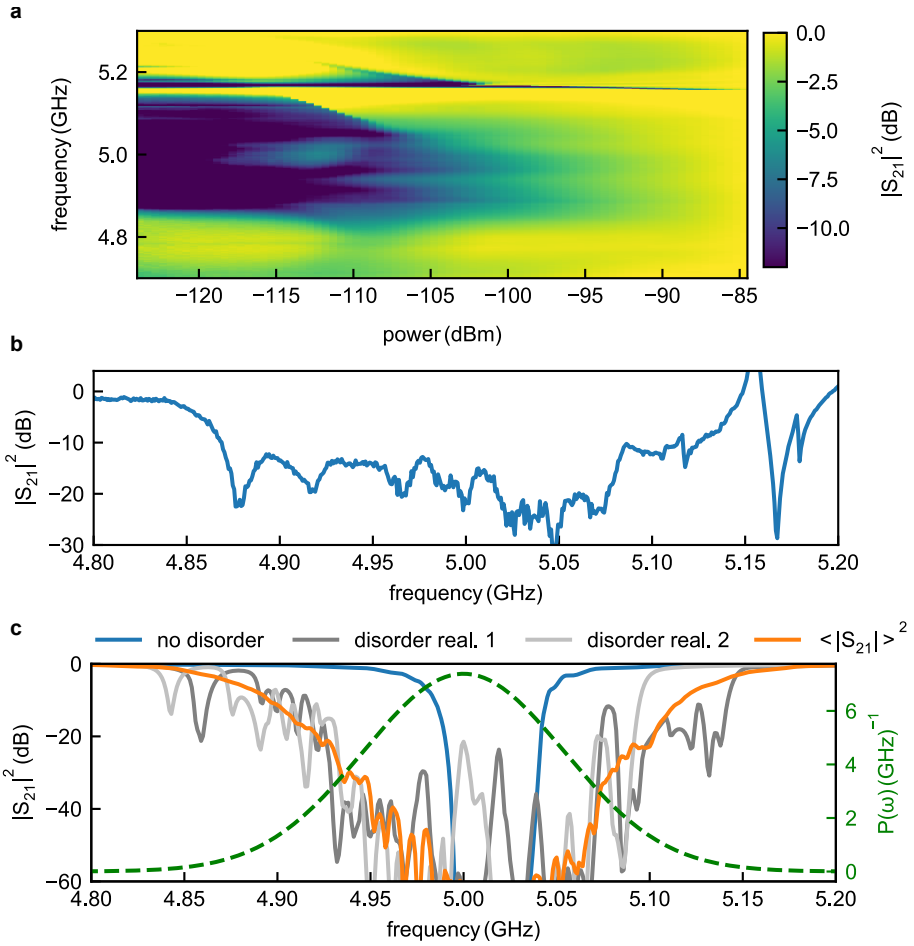

Figure 6.2: (a) Measured transmission coefficient $|S_{21}|^2$ of the 90 qubit metamaterial, featuring a $\approx$ 260 MHz wide band gap of suppressed transmission around the average qubit frequency $\omega_{10}/2\pi \approx 5$ GHz. The band gap shows saturation with increasing microwave power due to the qubits non-linearity. The non-saturable resonance below 5.2 GHz is a classical parasitic slotline mode. (b) Low power transmission ($P \approx -124$ dBm). (c) Calculated transmission of the 90 qubit metamaterial based on the T-matrix approach. Random qubit frequency disorder, according to a Gaussian probability distribution $P(\omega)$, is included. The orange line is an average over 100 different disorder realizations, indicating strong localization in the vicinity of the band gap of the perfectly ordered case (blue). The overall spectral region of suppressed transmission is broadened to the width of $P(\omega)$, compared to the ideal case. Used parameters: $\sigma_{f10} = 54$ MHz, decoherence rates are taken from Tab. 6.1.

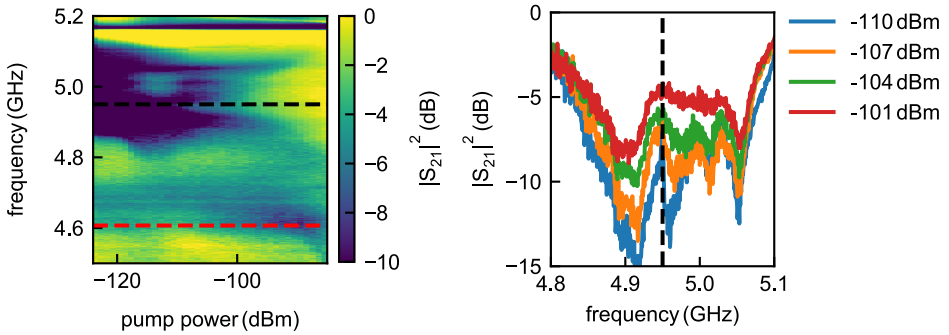

Figure 6.3: Spectral hole burning experiment. A pump microwave tone is applied in the center of the band gap at $\omega/2\pi \approx 4.95\,\mathrm{GHz}$ (black dashed line), while a weak probe tone is continuously monitoring the transmission $|S_{21}|^2$. With increasing pump power, the band gap gets partially and evenly saturated over a much wider spectral region than a single qubit linewidth $\Gamma_{1D}/2\pi \approx 8.6\,\mathrm{MHz}$. This indicates that the band gap is a partially homogenously broadened feature due to cooperative effects. For pump powers $P > -100\,\mathrm{dBm}$ the $1 \rightarrow 2$-transition is directly visible as a dip in $|S_{21}|^2$ around $\omega_{21}/2\pi \approx (\omega_{10} + \alpha)/2\pi = 4.607\,\mathrm{GHz}$ (red dashed line).

Sec. 5.4.4). Below 5.2 GHz an additional classical resonance is visible, which is not saturable with power. It is most likely caused by a parasitic slotline mode, which is created by imperfect on chip grounding [Wen+11]. The observed band gap is significantly larger than the theoretical value of $\Delta\omega/2\pi = \Gamma_{1D}c/(d\omega_{10}2\pi) \approx 41\,\mathrm{MHz}$ (Eq. 3.41), which is a consequence of the frequency disorder. To reproduce this observation, the transmission coefficient of the 90 qubit metamaterial is calculated using the T-matrix method (see Fig. 6.2(c)). Frequency disorder is included by randomly choosing the qubit frequencies according to a Gaussian probability distribution $P(\omega)$ with standard deviation $\sigma_{f10} = 54\,\mathrm{MHz}$ (derived from Eq. 6.1 and the measured relative normal resistance spread $\sigma_{R_\mathrm{n}}/R_\mathrm{n} \approx 2.2\,\%$) and center frequency of 5.0 GHz. In agreement with the experiment, the calculated transmission coefficients show a much wider region of suppressed transmission compared to the case of no disorder, which is a consequence of localization (see Sec. 5.6). The width of the disorder-broadened band gap is approximately given by the width of the probability distribution $P(\omega)$. In contrast to the disorder experiment in Sec. 5.6, here an averaging over several different disorder realizations is not possible to compute the localization length ζ. In order to discriminate between a homogeneously broadened band gap due to collective interactions between the qubits and inhomogeneous broadening induced by the random frequency spread, spectral hole burning is used (Fig. 6.3). The latter is a two-tone spectroscopy technique, where *holes* are burned selectively into the spectrum of inhomogeneously broadened emitters [Put+16; PV09]. Here, a weak probe tone is continuously probing the transmission, while a second pump is applied at a certain frequency in the

band gap region ($\omega/2\pi \approx 4.95\,\mathrm{GHz}$). If the band gap was an inhomogeneously broadened feature, for large enough pump powers, a *hole* of width Γ_{1D} would be burned into the band gap where transmission is increased[4]. However, if the band gap is a homogeneously broadened feature, it is expected to saturate as a whole. As visible in Fig. 6.2, with increasing pump power, the band gap region does not saturate completely collectively. However, a region around $\omega/2\pi = 4.95\,\mathrm{GHz}$ saturates with a much larger bandwidth than Γ_{1D}. This indicates that the observed band gap is not purely inhomogeneously broadened, but shows partial collective behavior.

In summary, the first realization of a 90 qubit metamaterial features a broad band gap in transmission measurements, which shows partial collective behavior. Due to an optimized Josephson junction fabrication procedure, the qubit frequency was reduced to an extend that most of the 90 qubits are found in a 260 MHz wide frequency range. The presented experiment demonstrates that the realization of large quantum metamaterials with collective interactions is within reach, even without the possibility of local frequency control. Recent results on reducing the critical current spread of Josephson junctions show that reaching homogeneities of $\sigma_{R_n}/R_n < 1\,\%$ is possible [Kre+20] and an overlap of a majority of qubits in frequency space could be ensured.

[4] For even larger powers, the *hole* of large transmission broadens since also neighbouring qubits get saturated.

7 Conclusion

The working objective of this thesis was to realize a quantum metamaterial formed by a one-dimensional waveguide loaded with a periodic array of qubits. The presented work extends previous experiments with one and two qubits towards a large scale waveguide quantum electrodynamics (wQED) system and is a crucial effort to increase system size in order to study cooperative effects. Our work was motivated by the benefits a realization of such systems would entail for the fundamental study of metamaterials and the field of quantum information processing.

In the first part of this work, we realized a quantum metamaterial comprising a densely spaced array of eight locally tunable transmon qubits [Bre+21]. In calibration measurements we extracted the full mutual inductance matrix between the qubits and the flux-bias lines and developed an active crosstalk compensation scheme allowing for true individual qubit control. In spectroscopic measurements we brought the qubits one by one to a common resonance frequency and observed the emergence of super- and subradiant collective polariton modes and the emergence of a polaritonic band gap. Since the number of resonant qubits N could be varied, we were able to extract a scaling of the radiative relaxation rate of the brightest sub-radiant state $\propto N^3$. The scaling is the complementary asymptotic of a widely discussed universal scaling in wQED of the darkest subradiant state following $\propto N^{-3}$. We probed the quantum non-linearity of the system by increasing the power beyond the single photon limit and observed that the polariton modes and the band gap are saturable. Furthermore, we used the first three quantum levels of the transmon qubits to demonstrate a collective Autler-Townes splitting (ATS) for up to eight resonant qubits. This also showcases active control of the band structure via an external control parameter. The collective ATS is of high relevance in terms of applications of the metamaterial in the field of quantum information processing and could be used for quantum memories, slow light and photon switches. Concluding the first part, we presented an experiment where artificial frequency disorder was introduced into the metamaterial. Although this experiment still needs a more thorough theoretical analysis, preliminary numerical simulations indicate that the observed suppression of transmission with disorder

is caused by Anderson localization and its strength can be controlled with the amount of added disorder.

In the second part we used the eight qubit metamaterial to demonstrate slow light. The reduction of the group velocity of light was achieved by employing two different techniques: first, the collective ATS was used to engineer a quasi-flat band, which is associated with the slow group velocity. We demonstrated in spectroscopic and time-resolved pulsed measurements a reduction of the latter by a factor greater than 1500 with respect to the vacuum speed of light. Moreover, we showed that we can control the effective group velocity by changing the strength of the microwave drive, which controls the ATS. The efficiency and maximal achievable delay of this approach was limited by the ladder-type level structure of the transmon qubits, which intrinsically dampens the quantum interference of electromagnetically induced transparency. Second, we engineered a similar band structure with a flat band based on two detuned collective 4 qubit resonances. Using this approach we observed similar retardations at three times larger efficiency and demonstrated that the group velocity can be tuned through the qubit detuning. The presented experiments are a first demonstration of slow light in superconducting wQED, where the qubits are directly used as dispersive elements and set a solid foundation towards the implementation of a quantum memory.

Finally, we presented first experiments on a scaled up metamaterial with 90 non-tunable qubits. Since the non-tunability comes at the cost of a random frequency spread between the qubits, we optimized the fabrication procedure of Josephson Junctions to mitigate this effect. Using a bridge-free fabrication procedure we reached low spreads in normal state resistance of 2.2 %. In spectroscopic measurements we found that the metamaterial features a disorder broadened and saturable band gap. Employing a spectral hole burning technique, we showed that the latter is partially homogeneously broadened due to cooperative qubit interactions. Our experiments provide a first indication that cooperative effects in disordered metamaterials are possible and motivate further studies with improved device parameters.

Outlook

Based on the foundation of this work, several further effects and applications can be investigated. In the following we suggest three tangible experiments with increasing complexity.

1. **Non-classical light**: collective quantum behavior of a multi-qubit wQED system is expected to be observed when measuring the second order cor-

relation function $g^2(\tau)$ of the reflected or transmitted light. As derived in Refs. [ZB13; FZB14], interference effects between the polaritonic eigenmodes lead to *quantum beats* in $g^2(\tau)$, meaning the temporal fluctuation between bunched ($g^2(\tau) > 1$) and anti-bunched light ($g^2(\tau) < 1$). Very recent results even indicate that these beats can occur on a much longer timescale than the non-radiative coherence time of the individual qubits [PP20]. Observing this genuine multi-qubit quantum effect is possible with the 8 qubit metamaterial of this work and established techniques to measure $g^2(\tau)$ with microwaves [Sil+10].

2. **Doubly excited polaritons**: the intrinsic non-linearity at the few photon level of the qubits leads to unique excitations when several photons are inserted into wQED systems. Decaying doubly excited polaritons in the two-excitation sector can be probed in the incoherent spectrum emitted from such structures [Ke+19]. Recently it was theoretically derived that some of the doubly excited polaritons show *selfinduced localization*, meaning one excitation forms a standing wave and the second gets trapped in it and is thus spatially localized [Zho+20]. Using a similar wQED system as in this work, but with individual qubit readout, would allow to probe the spatial mode profile of such exotic excitations.

3. **Realization of a quantum memory**: a quantum memory, which coherently stores microwave pulses can be realized based on one-dimensional wQED systems (see [LS12; Ase+17]). The memory protocol utilizes the concept of electromagnetically induced transparency (EIT), which is closely related to the demonstrated collective Autler-Townes splitting of this work. As discussed in this thesis, efficient EIT can only be reached with Λ-type three-level systems. Furthermore, efficient storage might require a longer structure than eight qubits [Ase+17]. Therefore, an efficient quantum memory could be realized based on a wQED system with fluxonium qubits which can feature a Λ-type three-level structure, instead of transmons [LS12].

In conclusion, we have succeeded to realize a superconducting wQED system with increased qubit number and local control. Beside a detailed analysis of the polaritonic eigenmodes, we showcased a first demonstration of slow light in the quantum metamaterial. Based on this work, further effects like non-classical light can be explored and a foundation for the realization of a quantum memory was set. We are therefore confident that our work is of relevance for the field of waveguide QED, which has implications on the development of new technologies for quantum information processing and the fundamental studies of quantum metamaterials.

Bibliography

[Abd+10] A. A. Abdumalikov, O. Astafiev, A. M. Zagoskin, Y. A. Pashkin, Y. Nakamura, and J. S. Tsai: *Electromagnetically Induced Transparency on a Single Artificial Atom*. Physical Review Letters **104**.19 (2010), p. 193601. DOI: 10.1103/PhysRevLett.104.193601 (cit. on pp. 3, 20, 26).

[Abd+11] A. A. Abdumalikov, O. V. Astafiev, Y. A. Pashkin, Y. Nakamura, and J. S. Tsai: *Dynamics of Coherent and Incoherent Emission from an Artificial Atom in a 1D Space*. Physical Review Letters **107**.4 (2011). Publisher: American Physical Society, p. 043604. DOI: 10.1103/PhysRevLett.107.043604 (cit. on pp. 3, 20).

[Abi10] T. Y. Abi-Salloum: *Electromagnetically induced transparency and Autler-Townes splitting: Two similar but distinct phenomena in two categories of three-level atomic systems*. Physical Review A **81**.5 (2010), p. 053836. DOI: 10.1103/PhysRevA.81.053836 (cit. on p. 29).

[Alb+19] A. Albrecht, L. Henriet, A. Asenjo-Garcia, P. B. Dieterle, O. Painter, and D. E. Chang: *Subradiant states of quantum bits coupled to a one-dimensional waveguide*. New Journal of Physics **21**.2 (2019), p. 025003. DOI: 10.1088/1367-2630/ab0134 (cit. on pp. 29, 32, 36, 70).

[AB63] V. Ambegaokar and A. Baratoff: *Tunneling Between Superconductors*. Physical Review Letters **10**.11 (1963). Publisher: American Physical Society, pp. 486–489. DOI: 10.1103/PhysRevLett.10.486 (cit. on p. 10).

[And58] P. W. Anderson: *Absence of Diffusion in Certain Random Lattices*. Physical Review **109**.5 (1958), pp. 1492–1505. DOI: 10.1103/physrev.109.1492 (cit. on p. 84).

[ADS11] P. M. Anisimov, J. P. Dowling, and B. C. Sanders: *Objectively Discerning Autler-Townes Splitting from Electromagnetically Induced Transparency*. Physical Review Letters **107**.16 (2011). Publisher: American Physical Society, p. 163604. DOI: 10.1103/PhysRevLett.107.163604 (cit. on pp. 29, 78).

[Aru+19] F. Arute, K. Arya, R. Babbush, D. Bacon, J. C. Bardin, R. Barends, R. Biswas, S. Boixo, F. G. S. L. Brandao, D. A. Buell, B. Burkett, Y. Chen, Z. Chen, B. Chiaro, R. Collins, W. Courtney, A. Dunsworth, E. Farhi, B. Foxen, A. Fowler, C. Gidney, M. Giustina, R. Graff, K. Guerin, S. Habegger, M. P. Harrigan, M. J. Hartmann, A. Ho, M. Hoffmann, T. Huang, T. S. Humble, S. V. Isakov, E. Jeffrey, Z. Jiang, D. Kafri, K. Kechedzhi, J. Kelly, P. V. Klimov, S. Knysh, A. Korotkov, F. Kostritsa, D. Landhuis, M. Lindmark, E. Lucero, D. Lyakh, S. Mandrà, J. R. McClean, M. McEwen, A. Megrant, X. Mi, K. Michielsen,

M. Mohseni, J. Mutus, O. Naaman, M. Neeley, C. Neill, M. Y. Niu, E. Ostby, A. Petukhov, J. C. Platt, C. Quintana, E. G. Rieffel, P. Roushan, N. C. Rubin, D. Sank, K. J. Satzinger, V. Smelyanskiy, K. J. Sung, M. D. Trevithick, A. Vainsencher, B. Villalonga, T. White, Z. J. Yao, P. Yeh, A. Zalcman, H. Neven, and J. M. Martinis: *Quantum supremacy using a programmable superconducting processor*. Nature **574**.7779 (2019), pp. 505–510. DOI: 10.1038/s41586-019-1666-5 (cit. on p. 2).

[Asa+15] H. Asai, S. Savel'ev, S. Kawabata, and A. M. Zagoskin: *Effects of lasing in a one-dimensional quantum metamaterial*. Physical Review B **91**.13 (2015). DOI: 10.1103/physrevb.91.134513 (cit. on p. 89).

[Ase+17] A. Asenjo-Garcia, M. Moreno-Cardoner, A. Albrecht, H. J. Kimble, and D. E. Chang: *Exponential Improvement in Photon Storage Fidelities Using Subradiance and "Selective Radiance" in Atomic Arrays*. Physical Review X **7**.3 (2017), p. 031024. DOI: 10.1103/PhysRevX.7.031024 (cit. on pp. 32, 33, 69, 70, 78, 81, 89, 97).

[Ast+10a] O. Astafiev, A. M. Zagoskin, A. A. Abdumalikov, Y. A. Pashkin, T. Yamamoto, K. Inomata, Y. Nakamura, and J. S. Tsai: *Resonance Fluorescence of a Single Artificial Atom*. Science **327**.5967 (2010), pp. 840–843. DOI: 10.1126/science.1181918 (cit. on pp. 3, 19, 20, 23, 24, 72).

[Ast+10b] O. V. Astafiev, A. A. Abdumalikov, A. M. Zagoskin, Y. A. Pashkin, Y. Nakamura, and J. S. Tsai: *Ultimate On-Chip Quantum Amplifier*. Physical Review Letters **104**.18 (2010), p. 183603. DOI: 10.1103/PhysRevLett.104.183603 (cit. on pp. 3, 20).

[AT55] S. H. Autler and C. H. Townes: *Stark Effect in Rapidly Varying Fields*. Physical Review **100**.2 (1955). Publisher: American Physical Society, pp. 703–722. DOI: 10.1103/PhysRev.100.703 (cit. on p. 27).

[Bab08] T. Baba: *Slow light in photonic crystals*. Nature Photonics **2**.8 (2008), pp. 465–473. DOI: 10.1038/nphoton.2008.146 (cit. on p. 75).

[Bab+15] R. Babbush, J. McClean, D. Wecker, A. Aspuru-Guzik, and N. Wiebe: *Chemical basis of Trotter-Suzuki errors in quantum chemistry simulation*. Physical Review A **91**.2 (2015). DOI: 10.1103/physreva.91.022311 (cit. on p. 1).

[BCS57] J. Bardeen, L. N. Cooper, and J. R. Schrieffer: *Microscopic Theory of Superconductivity*. Physical Review **106**.1 (1957). Publisher: American Physical Society, pp. 162–164. DOI: 10.1103/PhysRev.106.162 (cit. on p. 9).

[Bil+20] A. Bilmes, A. Megrant, P. Klimov, G. Weiss, J. M. Martinis, A. V. Ustinov, and J. Lisenfeld: *Resolving the positions of defects in superconducting quantum bits*. Scientific Reports **10**.1 (2020), p. 3090. DOI: 10.1038/s41598-020-59749-y (cit. on p. 60).

[Bil+21] A. Bilmes, S. Volosheniuk, J. D. Brehm, A. V. Ustinov, and J. Lisenfeld: *Quantum sensors for microscopic tunneling systems*. npj Quantum Information **7**.1 (2021), p. 27. DOI: 10.1038/s41534-020-00359-x (cit. on p. 60).

[Bla+04] A. Blais, R.-S. Huang, A. Wallraff, S. M. Girvin, and R. J. Schoelkopf: *Cavity quantum electrodynamics for superconducting electrical circuits: An architecture for quantum computation*. Physical Review A **69**.6 (2004). Publisher: American Physical Society, p. 062320. DOI: 10.1103/PhysRevA.69.062320 (cit. on pp. 2, 18).

[Bou+98] V. Bouchiat, D. Vion, P. Joyez, D. Esteve, and M. H. Devoret: *Quantum coherence with a single Cooper pair*. Physica Scripta **1998**.T76 (1998). Publisher: IOP Publishing, p. 165. DOI: 10.1238/Physica.Topical.076a00165 (cit. on p. 14).

[Bra+15] J. Braumüller, J. Cramer, S. Schlör, H. Rotzinger, L. Radtke, A. Lukashenko, P. Yang, S. T. Skacel, S. Probst, M. Marthaler, L. Guo, A. V. Ustinov, and M. Weides: *Multiphoton dressing of an anharmonic superconducting many-level quantum circuit*. Physical Review B **91**.5 (2015). Publisher: American Physical Society, p. 054523. DOI: 10.1103/PhysRevB.91.054523 (cit. on pp. 14, 73).

[Bre+17] J. D. Brehm, A. Bilmes, G. Weiss, A. V. Ustinov, and J. Lisenfeld: *Transmission-line resonators for the study of individual two-level tunneling systems*. Applied Physics Letters **111**.11 (2017). Publisher: American Institute of Physics, p. 112601. DOI: 10.1063/1.5001920 (cit. on p. 60).

[Bre+21] J. D. Brehm, A. N. Poddubny, A. Stehli, T. Wolz, H. Rotzinger, and A. V. Ustinov: *Waveguide bandgap engineering with an array of superconducting qubits*. npj Quantum Materials **6**.1 (2021), p. 10. DOI: 10.1038/s41535-021-00310-z (cit. on pp. 4, 32, 35, 60, 61, 67, 70, 95, 125, 126).

[Cad] Cadence: *Cadence TX-Line Transmission-Line Calculator*. https://www.awr.com/awr-software/options/tx-line. Accessed: 2020-11-26 (cit. on p. 58).

[Can+15] T. Caneva, M. T. Manzoni, T. Shi, J. S. Douglas, J. I. Cirac, and D. E. Chang: *Quantum dynamics of propagating photons with strong interactions: a generalized input–output formalism*. New Journal of Physics **17**.11 (2015), p. 113001. DOI: 10.1088/1367-2630/17/11/113001 (cit. on p. 30).

[Cha+12] D. E. Chang, L. Jiang, A. V. Gorshkov, and H. J. Kimble: *Cavity QED with atomic mirrors*. New Journal of Physics **14**.6 (2012), p. 063003. DOI: 10.1088/1367-2630/14/6/063003 (cit. on pp. 3, 35, 128).

[CW08] J. Clarke and F. K. Wilhelm: *Superconducting quantum bits*. Nature **453**.7198 (2008), pp. 1031–1042. DOI: 10.1038/nature07128 (cit. on p. 1).

[CM58] J. F. Cochran and D. E. Mapother: *Superconducting Transition in Aluminum*. Physical Review **111**.1 (1958). Publisher: American Physical Society, pp. 132–142. DOI: 10.1103/PhysRev.111.132 (cit. on p. 49).

[Cór+15] A. Córcoles, E. Magesan, S. J. Srinivasan, A. W. Cross, M. Steffen, J. M. Gambetta, and J. M. Chow: *Demonstration of a quantum error detection code using a square lattice of four superconducting qubits*. Nature Communications **6**.1 (2015), p. 6979. DOI: 10.1038/ncomms7979 (cit. on p. 2).

[Deu+95] I. H. Deutsch, R. J. C. Spreeuw, S. L. Rolston, and W. D. Phillips: *Photonic band gaps in optical lattices*. Physical Review A **52**.2 (1995), pp. 1394–1410. DOI: 10.1103/PhysRevA.52.1394 (cit. on pp. 33, 36).

[DS13] M. H. Devoret and R. J. Schoelkopf: *Superconducting Circuits for Quantum Information: An Outlook*. Science **339**.6124 (2013), pp. 1169–1174. DOI: 10.1126/science.1231930 (cit. on p. 1).

[Dic54] R. H. Dicke: *Coherence in Spontaneous Radiation Processes*. Physical Review **93**.1 (1954). Publisher: American Physical Society, pp. 99–110. DOI: 10.1103/PhysRev.93.99 (cit. on p. 32).

[DHB20] F. Dinc, L. E. Hayward, and A. M. Brańczyk: *Multidimensional super- and subradiance in waveguide quantum electrodynamics*. Physical Review Research **2**.4 (2020). DOI: 10.1103/physrevresearch.2.043149 (cit. on p. 70).

[Dmi+17] A. Y. Dmitriev, R. Shaikhaidarov, V. N. Antonov, T. Hönigl-Decrinis, and O. V. Astafiev: *Quantum wave mixing and visualisation of coherent and superposed photonic states in a waveguide*. Nature Communications **8**.1 (2017), p. 1352. DOI: 10.1038/s41467-017-01471-x (cit. on pp. 3, 20).

[Dol77] G. J. Dolan: *Offset masks for lift-off photoprocessing*. Applied Physics Letters **31**.5 (1977). Publisher: American Institute of Physics, pp. 337–339. DOI: 10.1063/1.89690 (cit. on p. 44).

[Dut+07] M. V. G. Dutt, L. Childress, L. Jiang, E. Togan, J. Maze, F. Jelezko, A. S. Zibrov, P. R. Hemmer, and M. D. Lukin: *Quantum Register Based on Individual Electronic and Nuclear Spin Qubits in Diamond*. Science **316**.5829 (2007), pp. 1312–1316. DOI: 10.1126/science.1139831 (cit. on p. 1).

[Eve+19] J. L. Everett, D. B. Higginbottom, G. T. Campbell, P. K. Lam, and B. C. Buchler: *Stationary Light in Atomic Media*. Advanced Quantum Technologies **2**.5-6 (2019), p. 1800100. DOI: 10.1002/qute.201800100 (cit. on p. 3).

[FKS10] S. Fan, Ş. E. Kocabaş, and J.-T. Shen: *Input-output formalism for few-photon transport in one-dimensional nanophotonic waveguides coupled to a qubit*. Physical Review A **82**.6 (2010). Publisher: American Physical Society, p. 063821. DOI: 10.1103/PhysRevA.82.063821 (cit. on p. 22).

[Fan17] Y. L. Fang: *Waveguide QED: Multiple Qubits, Inelastic Scattering, and Non-Markovianity*. PhD thesis. Duke University, 2017 (cit. on p. 23).

[FZB14] Y.-L. L. Fang, H. Zheng, and H. U. Baranger: *One-dimensional waveguide coupled to multiple qubits: photon-photon correlations*. EPJ Quantum Technology **1**.1 (2014), p. 3. DOI: 10.1140/epjqt3 (cit. on pp. 3, 29, 84, 97).

[Fey82] R. P. Feynman: *Simulating physics with computers*. International Journal of Theoretical Physics **21**.6-7 (1982), pp. 467–488. DOI: 10.1007/bf02650179 (cit. on p. 1).

[Fil+11] S. Filipp, M. Göppl, J. M. Fink, M. Baur, R. Bianchetti, L. Steffen, and A. Wallraff: *Multimode mediated qubit-qubit coupling and dark-state symmetries in circuit quantum electrodynamics*. Phys. Rev. A **83** (2011), p. 063827. DOI: 10.1103/PhysRevA.83.063827 (cit. on p. 72).

[FIM05] M. Fleischhauer, A. Imamoglu, and J. P. Marangos: *Electromagnetically induced transparency: Optics in coherent media*. Reviews of Modern Physics **77**.2 (2005), pp. 633–673. DOI: 10.1103/RevModPhys.77.633 (cit. on pp. 28, 38, 39, 81).

[For+16] P. Forn-Diaz, J. J. Garcia-Ripoll, B. Peropadre, J.-L. Orgiazzi, M. A. Yurtalan, R. Belyansky, C. M. Wilson, and A. Lupascu: *Ultrastrong coupling of a single artificial atom to an electromagnetic continuum in the nonperturbative regime*. Nature Physics **13**.1 (2016), pp. 39–43. DOI: 10.1038/nphys3905 (cit. on p. 2).

[Fri44] H. Friis: *Noise Figures of Radio Receivers*. Proceedings of the IRE **32**.7 (1944). Conference Name: Proceedings of the IRE, pp. 419–422. DOI: 10.1109/JRPROC.1944.232049 (cit. on p. 53).

[GC85] C. W. Gardiner and M. J. Collett: *Input and output in damped quantum systems: Quantum stochastic differential equations and the master equation*. Physical Review A **31**.6 (1985). Publisher: American Physical Society, pp. 3761–3774. DOI: 10.1103/PhysRevA.31.3761 (cit. on p. 21).

[GZ04] C. Gardiner and P. Zoller: *Quantum Noise: A Handbook of Markovian and Non-Markovian Quantum Stochastic Methods with Applications to Quantum Optics*. 3rd ed. Springer Series in Synergetics. Berlin Heidelberg: Springer-Verlag, 2004. URL: https://www.springer.com/de/book/9783540223016 (visited on 08/19/2020) (cit. on p. 51).

[Gea+95] J. Gea-Banacloche, Y.-q. Li, S.-z. Jin, and M. Xiao: *Electromagnetically induced transparency in ladder-type inhomogeneously broadened media: Theory and experiment*. Physical Review A **51**.1 (1995). Publisher: American Physical Society, pp. 576–584. DOI: 10.1103/PhysRevA.51.576 (cit. on p. 27).

[Geb+20a] R. Gebauer, N. Karcher, D. Gusenkova, M. Spiecker, L. Grünhaupt, I. Takmakov, P. Winkel, L. Planat, N. Roch, W. Wernsdorfer, A. V. Ustinov, M. Weber, M. Weides, I. M. Pop, and O. Sander: *State preparation of a fluxonium qubit with feedback from a custom FPGA-based platform*. AIP Conference Proceedings **2241**.1 (2020). Publisher: American Institute of Physics, p. 020015. DOI: 10.1063/5.0011721 (cit. on p. 54).

[Geb+20b] R. Gebauer, N. Karcher, J. Hurst, M. Weber, and O. Sander: *Accelerating complex control schemes on a heterogeneous MPSoC platform for quantum computing*. arXiv:2004.07755 [quant-ph] (2020). arXiv: 2004.07755. URL: http://arxiv.org/abs/2004.07755 (visited on 08/21/2020) (cit. on p. 54).

[GR16] M. Gegg and M. Richter: *Efficient and exact numerical approach for many multi-level systems in open system CQED*. New Journal of Physics **18**.4 (2016). Publisher: IOP Publishing, p. 043037. DOI: 10.1088/1367-2630/18/4/043037 (cit. on p. 124).

[Gol+09] F. Goldfarb, T. Lauprêtre, J. Ruggiero, F. Bretenaker, J. Ghosh, and R. Ghosh: *Electromagnetically-induced transparency, slow light, and negative group velocities in a room temperature vapor of 4He∗*. Comptes Rendus Physique **10**.10 (2009), pp. 919–926. DOI: 10.1016/j.crhy.2009.10.004 (cit. on p. 78).

[Gon+17] A. González-Tudela, V. Paulisch, H. J. Kimble, and J. I. Cirac: *Efficient Multiphoton Generation in Waveguide Quantum Electrodynamics*. Physical Review Letters **118**.21 (2017), p. 213601. DOI: 10.1103/PhysRevLett.118.213601 (cit. on p. 3).

[Gou+15] B. Gouraud, D. Maxein, A. Nicolas, O. Morin, and J. Laurat: *Demonstration of a Memory for Tightly Guided Light in an Optical Nanofiber*. Physical Review Letters **114**.18 (2015). Publisher: American Physical Society, p. 180503. DOI: 10.1103/PhysRevLett.114.180503 (cit. on pp. 39, 75).

[Gro97] L. K. Grover: *Quantum Mechanics Helps in Searching for a Needle in a Haystack*. Physical Review Letters **79**.2 (1997), pp. 325–328. DOI: 10.1103/physrevlett.79.325 (cit. on p. 1).

[Gu+17] X. Gu, A. F. Kockum, A. Miranowicz, Y.-x. Liu, and F. Nori: *Microwave photonics with superconducting quantum circuits*. Physics Reports **718-719** (2017), pp. 1–102. DOI: 10.1016/j.physrep.2017.10.002 (cit. on pp. 2, 3, 20).

[HFS16] H. R. Haakh, S. Faez, and V. Sandoghdar: *Polaritonic normal-mode splitting and light localization in a one-dimensional nanoguide*. Physical Review A **94**.5 (2016). Publisher: American Physical Society, p. 053840. DOI: 10.1103/PhysRevA.94.053840 (cit. on pp. 35, 67, 84).

[Hao+18] L. Hao, Y. Jiao, Y. Xue, X. Han, S. Bai, J. Zhao, and G. Raithel: *Transition from electromagnetically induced transparency to Autler–Townes splitting in cold cesium atoms*. New Journal of Physics **20**.7 (2018). Publisher: IOP Publishing, p. 073024. DOI: 10.1088/1367-2630/aad153 (cit. on p. 29).

[Hau+99] L. V. Hau, S. E. Harris, Z. Dutton, and C. H. Behroozi: *Light speed reduction to 17 metres per second in an ultracold atomic gas*. Nature **397**.6720 (1999), pp. 594–598. DOI: 10.1038/17561 (cit. on pp. 38, 75, 76).

[Hem+18] C. Hempel, C. Maier, J. Romero, J. McClean, T. Monz, H. Shen, P. Jurcevic, B. P. Lanyon, P. Love, R. Babbush, A. Aspuru-Guzik, R. Blatt, and C. F. Roos: *Quantum Chemistry Calculations on a Trapped-Ion Quantum Simulator*. Phys. Rev. X **8** (2018), p. 031022. DOI: 10.1103/PhysRevX.8.031022 (cit. on p. 1).

[Hoi+12] I.-C. Hoi, T. Palomaki, J. Lindkvist, G. Johansson, P. Delsing, and C. M. Wilson: *Generation of Nonclassical Microwave States Using an Artificial Atom in 1D Open Space*. Physical Review Letters **108**.26 (2012), p. 263601. DOI: 10.1103/PhysRevLett.108.263601 (cit. on pp. 3, 20).

[Hoi+13] I.-C. Hoi, C. M. Wilson, G. Johansson, J. Lindkvist, B. Peropadre, T. Palomaki, and P. Delsing: *Microwave quantum optics with an artificial atom in one-dimensional open space*. New Journal of Physics **15**.2 (2013), p. 025011. DOI: 10.1088/1367-2630/15/2/025011 (cit. on pp. 3, 20, 84).

[Hoi+11] I.-C. Hoi, C. M. Wilson, G. Johansson, T. Palomaki, B. Peropadre, and P. Delsing: *Demonstration of a Single-Photon Router in the Microwave Regime*. Physical Review Letters **107**.7 (2011). Publisher: American Physical Society, p. 073601. DOI: 10.1103/PhysRevLett.107.073601 (cit. on pp. 3, 20, 28, 74).

[Hoi13] I. C. Hoi: *Quantum Optics with Propagating Microwaves in Superconducting Circuits*. PhD thesis. Chalmers, Microtechnology and Nanoscience (MC2), 2013 (cit. on pp. 23, 27, 123).

[Hön+18] T. Hönigl-Decrinis, I. V. Antonov, R. Shaikhaidarov, V. N. Antonov, A. Y. Dmitriev, and O. V. Astafiev: *Mixing of coherent waves in a single three-level artificial atom*. Physical Review A **98**.4 (2018), p. 041801. DOI: 10.1103/PhysRevA.98.041801 (cit. on pp. 3, 20).

[Hön+20] T. Hönigl-Decrinis, R. Shaikhaidarov, S. de Graaf, V. Antonov, and O. Astafiev: *Two-Level System as a Quantum Sensor for Absolute Calibration of Power*. Physical Review Applied **13**.2 (2020). Publisher: American Physical Society, p. 024066. DOI: 10.1103/PhysRevApplied.13.024066 (cit. on p. 65).

[Hut+17] M. D. Hutchings, J. B. Hertzberg, Y. Liu, N. T. Bronn, G. A. Keefe, M. Brink, J. M. Chow, and B. L. T. Plourde: *Tunable Superconducting Qubits with Flux-Independent Coherence*. Physical Review Applied **8**.4 (2017). Publisher: American Physical Society, p. 044003. DOI: 10.1103/PhysRevApplied.8.044003 (cit. on p. 64).

[INJ94] E. L. Ivchenko, A. I. Nesvizhskii, and S. Jorda: *Bragg reflection of light from quantum-well structures*. Phys. Solid State **36** (1994), pp. 1156–1161 (cit. on pp. 127, 128).

[Ivc05] E. L. Ivchenko: *Optical Spectroscopy of Semiconductor Nanostructures*. Alpha Science, 2005 (cit. on pp. 31, 36, 67).

[Joo+10] J. Joo, J. Bourassa, A. Blais, and B. C. Sanders: *Electromagnetically Induced Transparency with Amplification in Superconducting Circuits*. Phys. Rev. Lett. **105** (2010), p. 073601. DOI: 10.1103/PhysRevLett.105.073601 (cit. on p. 82).

[Jos62] B. D. Josephson: *Possible new effects in superconductive tunnelling*. Physics Letters **1**.7 (1962), pp. 251–253. DOI: 10.1016/0031-9163(62)91369-0 (cit. on p. 10).

[Kam11] H. Kamerlingh Onnes: *The resistance of pure mercury at helium temperatures*. Commun. Phys. Lab. Univ. Leiden, b **120** (1911) (cit. on p. 9).

[Kan18] B. Kannan: *Waveguide Quantum Electrodynamics with Superconducting Qubits*. MA thesis. Massachusetts Institute of Technology, 2018 (cit. on p. 20).

[Kan+20] B. Kannan, D. Campbell, F. Vasconcelos, R. Winik, D. Kim, M. Kjaergaard, P. Krantz, A. Melville, B. M. Niedzielski, J. Yoder, T. P. Orlando, S. Gustavsson, and W. D. Oliver: *Generating Spatially Entangled Itinerant Photons with Waveguide Quantum Electrodynamics*. arXiv:2003.07300 [quant-ph] (2020). arXiv: 2003.07300. URL: http://arxiv.org/abs/2003.07300 (visited on 06/24/2020) (cit. on pp. 3, 29).

[Ke+19] Y. Ke, A. V. Poshakinskiy, C. Lee, Y. S. Kivshar, and A. N. Poddubny: *Inelastic Scattering of Photon Pairs in Qubit Arrays with Subradiant States*. Phys. Rev. Lett. **123** (2019), p. 253601. DOI: 10.1103/PhysRevLett.123.253601 (cit. on p. 97).

[Kel+15] J. Kelly, R. Barends, A. G. Fowler, A. Megrant, E. Jeffrey, T. C. White, D. Sank, J. Y. Mutus, B. Campbell, Y. Chen, Z. Chen, B. Chiaro, A. Dunsworth, I.-C. Hoi, C. Neill, P. J. J. O'Malley, C. Quintana, P. Roushan, A. Vainsencher, J. Wenner, A. N. Cleland, and J. M. Martinis: *State preservation by repetitive error detection in a superconducting quantum circuit*. Nature **519**.7541 (2015), pp. 66–69. DOI: 10.1038/nature14270 (cit. on p. 2).

[Ken+19] O. Kennedy, J. Burnett, J. Fenton, N. Constantino, P. Warburton, J. Morton, and E. Dupont-Ferrier: *Tunable Nb Superconducting Resonator Based on a Constriction Nano-SQUID Fabricated with a Ne Focused Ion Beam*. Physical Review Applied **11**.1 (2019). Publisher: American Physical Society, p. 014006. DOI: 10.1103/PhysRevApplied.11.014006 (cit. on p. 11).

[Kha+12] M. S. Khalil, M. J. A. Stoutimore, F. C. Wellstood, and K. D. Osborn: *An analysis method for asymmetric resonator transmission applied to superconducting devices*. Journal of Applied Physics **111**.5 (2012). Publisher: American Institute of Physics, p. 054510. DOI: 10.1063/1.3692073 (cit. on pp. 25, 69).

[Kim08] H. J. Kimble: *The quantum internet*. Nature **453**.7198 (2008), pp. 1023–1030. DOI: 10.1038/nature07127 (cit. on p. 3).

[Kja+20] M. Kjaergaard, M. E. Schwartz, J. Braumüller, P. Krantz, J. I.-J. Wang, S. Gustavsson, and W. D. Oliver: *Superconducting Qubits: Current State of Play*. Annual Review of Condensed Matter Physics **11**.1 (2020), pp. 369–395. DOI: 10.1146/annurev-conmatphys-031119-050605 (cit. on p. 1).

[Kli+18] P. V. Klimov, J. Kelly, Z. Chen, M. Neeley, A. Megrant, B. Burkett, R. Barends, K. Arya, B. Chiaro, Y. Chen, A. Dunsworth, A. Fowler, B. Foxen, C. Gidney, M. Giustina, R. Graff, T. Huang, E. Jeffrey, E. Lucero, J. Y. Mutus, O. Naaman, C. Neill, C. Quintana, P. Roushan, D. Sank, A. Vainsencher, J. Wenner, T. C. White, S. Boixo, R. Babbush, V. N. Smelyanskiy, H. Neven, and J. M. Martinis: *Fluctuations of Energy-Relaxation Times in Superconducting Qubits*. Phys. Rev. Lett. **121** (2018), p. 090502. DOI: 10.1103/PhysRevLett.121.090502 (cit. on p. 60).

[KLM01] E. Knill, R. Laflamme, and G. J. Milburn: *A scheme for efficient quantum computation with linear optics*. Nature **409**.6816 (2001), pp. 46–52. DOI: 10.1038/35051009 (cit. on p. 1).

[Koc+07] J. Koch, T. M. Yu, J. Gambetta, A. A. Houck, D. I. Schuster, J. Majer, A. Blais, M. H. Devoret, S. M. Girvin, and R. J. Schoelkopf: *Charge-insensitive qubit design derived from the Cooper pair box*. Physical Review A **76**.4 (2007), p. 042319. DOI: 10.1103/PhysRevA.76.042319 (cit. on pp. 12, 15, 17, 18).

[KVM07] P. J. Koppinen, L. M. Väistö, and I. J. Maasilta: *Complete stabilization and improvement of the characteristics of tunnel junctions by thermal annealing*. Applied Physics Letters **90**.5 (2007). Publisher: American Institute of Physics, p. 053503. DOI: 10.1063/1.2437662 (cit. on p. 47).

[KP07] V. A. Kosobukin and A. N. Poddubny: *Exciton-polariton absorption in periodic and disordered quantum-well chains*. Physics of the Solid State **49**.10 (2007), pp. 1977–1987. DOI: 10.1134/s1063783407100289 (cit. on p. 127).

[Kra+19] P. Krantz, M. Kjaergaard, F. Yan, T. P. Orlando, S. Gustavsson, and W. D. Oliver: *A Quantum Engineer's Guide to Superconducting Qubits*. arXiv:1904.06560 [cond-mat, physics:physics, physics:quant-ph] (2019). arXiv: 1904.06560. URL: http://arxiv.org/abs/1904.06560 (visited on 06/04/2019) (cit. on pp. 5, 7, 11, 13, 14, 23).

[Kre+20] J. M. Kreikebaum, K. P. O'Brien, A. Morvan, and I. Siddiqi: *Improving wafer-scale Josephson junction resistance variation in superconducting quantum coherent circuits*. Superconductor Science and Technology **33**.6 (2020), 06LT02. DOI: 10.1088/1361-6668/ab8617 (cit. on pp. 84, 94).

[Kri+19] S. Krinner, S. Storz, P. Kurpiers, P. Magnard, J. Heinsoo, R. Keller, J. Lütolf, C. Eichler, and A. Wallraff: *Engineering cryogenic setups for 100-qubit scale superconducting circuit systems*. EPJ Quantum Technology **6**.1 (2019). Number: 1 Publisher: SpringerOpen, pp. 1–29. DOI: 10.1140/epjqt/s40507-019-0072-0 (cit. on p. 51).

[Kro+19] T. Kroh, J. Wolters, A. Ahlrichs, A. W. Schell, A. Thoma, S. Reitzenstein, J. S. Wildmann, E. Zallo, R. Trotta, A. Rastelli, O. G. Schmidt, and O. Benson: *Slow and fast single photons from a quantum dot interacting with the excited state hyperfine structure of the Cesium D 1 -line*. Scientific Reports **9**.1 (2019). Number: 1 Publisher: Nature Publishing Group, p. 13728. DOI: 10.1038/s41598-019-50062-x (cit. on p. 75).

[Lal+13] K. Lalumière, B. C. Sanders, A. F. van Loo, A. Fedorov, A. Wallraff, and A. Blais: *Input-output theory for waveguide QED with an ensemble of inhomogeneous atoms*. Physical Review A **88**.4 (2013), p. 043806. DOI: 10.1103/PhysRevA.88.043806 (cit. on pp. 2, 3, 20, 30, 31, 73).

[Lan+10] B. P. Lanyon, J. D. Whitfield, G. G. Gillett, M. E. Goggin, M. P. Almeida, I. Kassal, J. D. Biamonte, M. Mohseni, B. J. Powell, M. Barbieri, A. Aspuru-Guzik, and A. G. White: *Towards quantum chemistry on a quantum computer*. Nature Chemistry **2**.2 (2010), pp. 106–111. DOI: 10.1038/nchem.483 (cit. on p. 1).

[Lec+11] F. Lecocq, I. M. Pop, Z. Peng, I. Matei, T. Crozes, T. Fournier, C. Naud, W. Guichard, and O. Buisson: *Junction fabrication by shadow evaporation without a suspended bridge*. Nanotechnology **22**.31 (2011). Publisher: IOP Publishing, p. 315302. DOI: 10.1088/0957-4484/22/31/315302 (cit. on p. 44).

[Lei+03] D. Leibfried, R. Blatt, C. Monroe, and D. Wineland: *Quantum dynamics of single trapped ions*. Reviews of Modern Physics **75**.1 (2003), pp. 281–324. DOI: 10.1103/revmodphys.75.281 (cit. on p. 1).

[Lep+19] J. Leppäkangas, J. D. Brehm, P. Yang, L. Guo, M. Marthaler, A. V. Ustinov, and M. Weides: *Resonance inversion in a superconducting cavity coupled to artificial atoms and a microwave background*. Physical Review A **99**.6 (2019). Publisher: American Physical Society, p. 063804. DOI: 10.1103/PhysRevA.99.063804 (cit. on pp. 35, 67).

[LS12] P. M. Leung and B. C. Sanders: *Coherent Control of Microwave Pulse Storage in Superconducting Circuits*. Physical Review Letters **109**.25 (2012), p. 253603. DOI: 10.1103/PhysRevLett.109.253603 (cit. on pp. 3, 78, 84, 97).

[Lie+19] B. Lienhard, J. Braumüller, W. Woods, D. Rosenberg, G. Calusine, S. Weber, A. Vepsäläinen, K. O'Brien, T. P. Orlando, S. Gustavsson, and W. D. Oliver: *Microwave Packaging for Superconducting Qubits*. arXiv:1906.05425 [quant-ph] (2019). arXiv: 1906.05425. URL: http://arxiv.org/abs/1906.05425 (visited on 08/17/2020) (cit. on p. 47).

[Lim+17] M. F. Limonov, M. V. Rybin, A. N. Poddubny, and Y. S. Kivshar: *Fano resonances in photonics*. Nature Photonics **11**.9 (2017), pp. 543–554. DOI: 10.1038/nphoton.2017.142 (cit. on p. 128).

[Liu+01] C. Liu, Z. Dutton, C. H. Behroozi, and L. V. Hau: *Observation of coherent optical information storage in an atomic medium using halted light pulses*. Nature **409**.6819 (2001), pp. 490–493. DOI: 10.1038/35054017 (cit. on p. 39).

[LLL35] F. London, H. London, and F. A. Lindemann: *The electromagnetic equations of the supraconductor*. Proceedings of the Royal Society of London. Series A - Mathematical and Physical Sciences **149**.866 (1935). Publisher: Royal Society, pp. 71–88. DOI: 10.1098/rspa.1935.0048 (cit. on p. 9).

[Loo14] A. F. van Loo: *Interactions in waveguide quantum electrodynamics*. PhD thesis. ETH Zurich, 2014 (cit. on pp. 23, 64).

[Loo+13] A. F. v. Loo, A. Fedorov, K. Lalumière, B. C. Sanders, A. Blais, and A. Wallraff: *Photon-Mediated Interactions Between Distant Artificial Atoms*. Science **342**.6165 (2013), pp. 1494–1496. DOI: 10.1126/science.1244324 (cit. on pp. 3, 29, 31).

[LU08] A. Lukashenko and A. V. Ustinov: *Improved powder filters for qubit measurements*. Review of Scientific Instruments **79**.1 (2008). Publisher: American Institute of Physics, p. 014701. DOI: 10.1063/1.2827515 (cit. on p. 53).

[LST09] A. I. Lvovsky, B. C. Sanders, and W. Tittel: *Optical quantum memory*. Nature Photonics **3**.12 (2009), pp. 706–714. DOI: 10.1038/nphoton.2009.231 (cit. on pp. 3, 75).

[Mac+14] P. Macha, G. Oelsner, J.-M. Reiner, M. Marthaler, S. André, G. Schön, U. Hübner, H.-G. Meyer, E. Il'ichev, and A. V. Ustinov: *Implementation of a quantum metamaterial using superconducting qubits*. Nature Communications **5**.1 (2014), p. 5146. DOI: 10.1038/ncomms6146 (cit. on p. 2).

[Mac+15] C. Macklin, K. O'Brien, D. Hover, M. E. Schwartz, V. Bolkhovsky, X. Zhang, W. D. Oliver, and I. Siddiqi: *A near–quantum-limited Josephson traveling-wave parametric amplifier*. Science **350**.6258 (2015). Publisher: American Association for the Advancement of Science Section: Report, pp. 307–310. DOI: 10.1126/science.aaa8525 (cit. on p. 53).

[MC19] D. Malz and J. I. Cirac: *Number-resolving photon detectors with atoms coupled to waveguides*. arXiv:1906.12296 [quant-ph] (2019). arXiv: 1906.12296. URL: http://arxiv.org/abs/1906.12296 (visited on 07/02/2019) (cit. on p. 3).

[Man20] D. Manzano: *A short introduction to the Lindblad master equation*. AIP Advances **10**.2 (2020). Publisher: American Institute of Physics, p. 025106. DOI: 10.1063/1.5115323 (cit. on pp. 7, 8, 33).

[Mar+05] J. M. Martinis, K. B. Cooper, R. McDermott, M. Steffen, M. Ansmann, K. D. Osborn, K. Cicak, S. Oh, D. P. Pappas, R. W. Simmonds, and C. C. Yu: *Decoherence in Josephson Qubits from Dielectric Loss*. Physical Review Letters **95**.21 (2005). Publisher: American Physical Society, p. 210503. DOI: 10.1103/PhysRevLett.95.210503 (cit. on pp. 46, 60).

[Mar+03] J. M. Martinis, S. Nam, J. Aumentado, K. M. Lang, and C. Urbina: *Decoherence of a superconducting qubit due to bias noise*. Physical Review B **67**.9 (2003). Publisher: American Physical Society, p. 094510. DOI: 10.1103/PhysRevB.67.094510 (cit. on p. 23).

[McR+20] C. R. H. McRae, H. Wang, J. Gao, M. Vissers, T. Brecht, A. Dunsworth, D. Pappas, and J. Mutus: *Materials loss measurements using superconducting microwave resonators*. arXiv:2006.04718 [physics, physics:quant-ph] (2020). URL: http://arxiv.org/abs/2006.04718 (visited on 08/12/2020) (cit. on p. 42).

[MO33] W. Meissner and R. Ochsenfeld: *Ein neuer Effekt bei Eintritt der Supraleitfähigkeit*. Naturwissenschaften **21**.44 (1933), pp. 787–788. DOI: 10.1007/BF01504252 (cit. on p. 9).

[MBD99] X. Meng, A. Bhat, and T. van Duzer: *Very small critical current spreads in Nb/Al-AlOx/Nb integrated circuits using low-temperature and low-stress ECR PECVD silicon oxide films*. IEEE Transactions on Applied Superconductivity **9** (1999). Conference Name: IEEE Transactions on Applied Superconductivity, pp. 3208–3211. DOI: 10.1109/77.783711 (cit. on p. 46).

[Mir+18] M. Mirhosseini, E. Kim, V. S. Ferreira, M. Kalaee, A. Sipahigil, A. J. Keller, and O. Painter: *Superconducting metamaterials for waveguide quantum electrodynamics*. Nature Communications **9**.1 (2018), p. 3706. DOI: 10.1038/s41467-018-06142-z (cit. on pp. 72, 75, 84, 86).

[Mir+19] M. Mirhosseini, E. Kim, X. Zhang, A. Sipahigil, P. B. Dieterle, A. J. Keller, A. Asenjo-Garcia, D. E. Chang, and O. Painter: *Cavity quantum electrodynamics with atom-like mirrors*. Nature **569**.7758 (2019). Number: 7758 Publisher: Nature Publishing Group, pp. 692–697. DOI: 10.1038/s41586-019-1196-1 (cit. on pp. 3, 22, 24, 29, 35).

[MS18] I. M. Mirza and J. C. Schotland: *Influence of disorder on electromagnetically induced transparency in chiral waveguide quantum electrodynamics*. Journal of the Optical Society of America B **35**.5 (2018), p. 1149. DOI: 10.1364/josab.35.001149 (cit. on pp. 84, 86).

[MF19] M. K. Moghaddam and R. Fleury: *Slow light engineering in resonant photonic crystal line-defect waveguides*. Opt. Express **27**.18 (2019), pp. 26229–26238. DOI: 10.1364/OE.27.026229 (cit. on p. 75).

[Mol69] B. R. Mollow: *Power Spectrum of Light Scattered by Two-Level Systems*. Physical Review **188**.5 (1969). Publisher: American Physical Society, pp. 1969–1975. DOI: 10.1103/PhysRev.188.1969 (cit. on p. 24).

[MCL19] C. Müller, J. H. Cole, and J. Lisenfeld: *Towards understanding two-level-systems in amorphous solids: insights from quantum circuits*. Reports on Progress in Physics **82**.12 (2019), p. 124501. DOI: 10.1088/1361-6633/ab3a7e (cit. on p. 46).

[NPT99] Y. Nakamura, Y. A. Pashkin, and J. S. Tsai: *Coherent control of macroscopic quantum states in a single-Cooper-pair box*. Nature **398**.6730 (1999). Number: 6730 Publisher: Nature Publishing Group, pp. 786–788. DOI: 10.1038/19718 (cit. on pp. 1, 14, 15).

[NK76] J. Niemeyer and V. Kose: *Observation of large dc supercurrents at nonzero voltages in Josephson tunnel junctions*. Applied Physics Letters **29**.6 (1976). Publisher: American Institute of Physics, pp. 380–382. DOI: 10.1063/1.89094 (cit. on p. 44).

[NWX11] I. Novikova, R. Walsworth, and Y. Xiao: *Electromagnetically induced transparency-based slow and stored light in warm atoms*. Laser & Photonics Reviews **6**.3 (2011), pp. 333–353. DOI: 10.1002/lpor.201100021 (cit. on p. 81).

[OS06] L. E. Ocola and A. Stein: *Effect of cold development on improvement in electron-beam nanopatterning resolution and line roughness*. Journal of Vacuum Science & Technology B: Microelectronics and Nanometer Structures **24**.6 (2006), p. 3061. DOI: 10.1116/1.2366698 (cit. on p. 44).

[Pau+18] V. Paulisch, H. J. Kimble, J. I. Cirac, and A. González-Tudela: *Generation of single- and two-mode multiphoton states in waveguide QED*. Physical Review A **97**.5 (2018), p. 053831. DOI: 10.1103/PhysRevA.97.053831 (cit. on p. 3).

[PKG16] V. Paulisch, H. J. Kimble, and A. González-Tudela: *Universal quantum computation in waveguide QED using decoherence free subspaces*. New Journal of Physics **18**.4 (2016). Publisher: IOP Publishing, p. 043041. DOI: 10.1088/1367-2630/18/4/043041 (cit. on p. 3).

[Pet05] J. R. Petta: *Coherent Manipulation of Coupled Electron Spins in Semiconductor Quantum Dots*. Science **309**.5744 (2005), pp. 2180–2184. DOI: 10.1126/science.1116955 (cit. on p. 1).

[Phi+01] D. F. Phillips, A. Fleischhauer, A. Mair, R. L. Walsworth, and M. D. Lukin: *Storage of Light in Atomic Vapor*. Physical Review Letters **86**.5 (2001). Publisher: American Physical Society, pp. 783–786. DOI: 10.1103/PhysRevLett.86.783 (cit. on p. 39).

[Pob07] F. Pobell: *Matter and methods at low temperatures : with 28 tables, and 81 problems*. 3., rev. and expanded ed. Berlin: Springer, 2007. URL: http://www.gbv.de/dms/bsz/toc/bsz263279715inh.pdf (cit. on p. 49).

[Pod20] A. N. Poddubny: *Quasiflat band enabling subradiant two-photon bound states*. Phys. Rev. A **101** (2020), p. 043845. DOI: 10.1103/PhysRevA.101.043845 (cit. on p. 125).

[Pop+12] I. M. Pop, T. Fournier, T. Crozes, F. Lecocq, I. Matei, B. Pannetier, O. Buisson, and W. Guichard: *Fabrication of stable and reproducible submicron tunnel junctions*. Journal of Vacuum Science & Technology B **30**.1 (2012). Publisher: American Vacuum Society, p. 010607. DOI: 10.1116/1.3673790 (cit. on pp. 46, 47).

[PP20] A. V. Poshakinskiy and A. N. Poddubny: *Quantum Borrmann effect for dissipation-immune photon-photon correlations*. arXiv: 2009.14049. (2020). URL: https://arxiv.org/abs/2009.14049 (visited on 02/08/2021) (cit. on p. 97).

[Poz11] D. Pozar: *Microwave Engineering, 4th Edition*. Wiley, 2011. URL: https://books.google.de/books?id=JegbAAAAQBAJ (cit. on pp. 21, 54).

[Pre18] J. Preskill: *Quantum Computing in the NISQ era and beyond*. Quantum **2** (2018), p. 79. DOI: 10.22331/q-2018-08-06-79 (cit. on p. 2).

[Pro+15] S. Probst, F. B. Song, P. A. Bushev, A. V. Ustinov, and M. Weides: *Efficient and robust analysis of complex scattering data under noise in microwave resonators*. Review of Scientific Instruments **86**.2 (2015), p. 024706. DOI: 10.1063/1.4907935 (cit. on pp. 24, 63).

[PV09] R. Purchase and S. Völker: *Spectral hole burning: examples from photosynthesis*. Photosynthesis Research **101**.2-3 (2009), pp. 245–266. DOI: 10.1007/s11120-009-9484-5 (cit. on pp. 89, 93).

[Put+16] S. Putz, A. Angerer, D. O. Krimer, R. Glattauer, W. J. Munro, S. Rotter, J. Schmiedmayer, and J. Majer: *Spectral hole burning and its application in microwave photonics*. Nature Photonics **11**.1 (2016), pp. 36–39. DOI: 10.1038/nphoton.2016.225 (cit. on pp. 89, 93).

[Qui+14] C. M. Quintana, A. Megrant, Z. Chen, A. Dunsworth, B. Chiaro, R. Barends, B. Campbell, Y. Chen, I.-C. Hoi, E. Jeffrey, J. Kelly, J. Y. Mutus, P. J. J. O'Malley, C. Neill, P. Roushan, D. Sank, A. Vainsencher, J. Wenner, T. C. White, A. N. Cleland, and J. M. Martinis: *Characterization and reduction of microfabrication-induced decoherence in superconducting quantum circuits*. Applied Physics Letters **105**.6 (2014). Publisher: American Institute of Physics, p. 062601. DOI: 10.1063/1.4893297 (cit. on p. 42).

[Rak+08] A. L. Rakhmanov, A. M. Zagoskin, S. Savel'ev, and F. Nori: *Quantum metamaterials: Electromagnetic waves in a Josephson qubit line*. Phys. Rev. B **77** (2008), p. 144507. DOI: 10.1103/PhysRevB.77.144507 (cit. on pp. 3, 89).

[Ras+19] A. Rastogi, E. Saglamyurek, T. Hrushevskyi, S. Hubele, and L. J. LeBlanc: *Discerning quantum memories based on electromagnetically-induced-transparency and Autler-Townes-splitting protocols*. Phys. Rev. A **100** (2019), p. 012314. DOI: 10.1103/PhysRevA.100.012314 (cit. on p. 81).

[Ree+12] M. D. Reed, L. DiCarlo, S. E. Nigg, L. Sun, L. Frunzio, S. M. Girvin, and R. J. Schoelkopf: *Realization of three-qubit quantum error correction with superconducting circuits*. Nature **482**.7385 (2012), pp. 382–385. DOI: 10.1038/nature10786 (cit. on p. 2).

[RD16] A. Roy and M. Devoret: *Introduction to parametric amplification of quantum signals with Josephson circuits*. Comptes Rendus Physique. Quantum microwaves / Micro-ondes quantiques **17**.7 (2016), pp. 740–755. DOI: 10.1016/j.crhy.2016.07.012 (cit. on p. 53).

[RWF17] D. Roy, C. M. Wilson, and O. Firstenberg: *Colloquium: Strongly interacting photons in one-dimensional continuum*. Rev. Mod. Phys. **89** (2017), p. 021001. DOI: 10.1103/RevModPhys.89.021001 (cit. on p. 2).

[Sch19] S. Schloer: *Intrinsic decoherence in superconducting quantum circuits*. PhD thesis. Karlsruhe Institute of Technology, 2019 (cit. on p. 49).

[Sch+19] S. Schlör, J. Lisenfeld, C. Müller, A. Bilmes, A. Schneider, D. P. Pappas, A. V. Ustinov, and M. Weides: *Correlating Decoherence in Transmon Qubits: Low Frequency Noise by Single Fluctuators*. Physical Review Letters **123**.19 (2019). Publisher: American Physical Society, p. 190502. DOI: 10.1103/PhysRevLett.123.190502 (cit. on p. 60).

[Sch+97] V. Schmidt, V. Müller, V. Schmidt, P. Müller, I. Grigorieva, and A. Ustinov: *The Physics of Superconductors: Introduction to Fundamentals and Applications*. Springer, 1997. URL: https://books.google.de/books?id=8O8svNo_tWoC (cit. on pp. 10, 12).

[Sch+08] J. A. Schreier, A. A. Houck, J. Koch, D. I. Schuster, B. R. Johnson, J. M. Chow, J. M. Gambetta, J. Majer, L. Frunzio, M. H. Devoret, S. M. Girvin, and R. J. Schoelkopf: *Suppressing charge noise decoherence in superconducting charge qubits*. Physical Review B **77**.18 (2008). Publisher: American Physical Society, p. 180502. DOI: 10.1103/PhysRevB.77.180502 (cit. on p. 15).

[Sch+05] D. I. Schuster, A. Wallraff, A. Blais, L. Frunzio, R.-S. Huang, J. Majer, S. M. Girvin, and R. J. Schoelkopf: *ac Stark Shift and Dephasing of a Superconducting Qubit Strongly Coupled to a Cavity Field*. Physical Review Letters **94**.12 (2005). Publisher: American Physical Society, p. 123602. DOI: 10.1103/PhysRevLett.94.123602 (cit. on p. 65).

[Sha+15] D. Shapiro, P. Macha, A. Rubtsov, and A. Ustinov: *Dispersive Response of a Disordered Superconducting Quantum Metamaterial*. Photonics **2**.2 (2015), pp. 449–458. DOI: 10.3390/photonics2020449 (cit. on p. 2).

[She+07] J.-T. Shen, M. L. Povinelli, S. Sandhu, and S. Fan: *Stopping single photons in one-dimensional circuit quantum electrodynamics systems*. Physical Review B **75**.3 (2007). DOI: 10.1103/physrevb.75.035320 (cit. on pp. 75, 82, 84).

[SSH97] A. Shnirman, G. Schön, and Z. Hermon: *Quantum Manipulations of Small Josephson Junctions*. Physical Review Letters **79**.12 (1997). Publisher: American Physical Society, pp. 2371–2374. DOI: 10.1103/PhysRevLett.79.2371 (cit. on p. 14).

[Sho94] P. Shor: *Algorithms for quantum computation: discrete logarithms and factoring*. *Proceedings 35th Annual Symposium on Foundations of Computer Science*. IEEE Comput. Soc. Press, 1994. DOI: 10.1109/sfcs.1994.365700 (cit. on p. 1).

[Shu+17] K. V. Shulga, P. Yang, G. P. Fedorov, M. V. Fistul, M. Weides, and A. V. Ustinov: *Observation of a collective mode of an array of transmon qubits*. JETP Letters **105**.1 (2017), pp. 47–50. DOI: 10.1134/s0021364017010143 (cit. on p. 2).

[Sil+10] M. P. da Silva, D. Bozyigit, A. Wallraff, and A. Blais: *Schemes for the observation of photon correlation functions in circuit QED with linear detectors*. Phys. Rev. A **82** (2010), p. 043804. DOI: 10.1103/PhysRevA.82.043804 (cit. on p. 97).

[SPW04] D. R. Smith, J. B. Pendry, and M. C. K. Wiltshire: *Metamaterials and Negative Refractive Index*. Science **305**.5685 (2004), pp. 788–792. DOI: 10.1126/science.1096796 (cit. on pp. 3, 35).

[Ste+20] A. Stehli, J. D. Brehm, T. Wolz, P. Baity, S. Danilin, V. Seferai, H. Rotzinger, A. V. Ustinov, and M. Weides: *Coherent superconducting qubits from a subtractive junction fabrication process*. Applied Physics Letters **117**.12 (2020). Publisher: American Institute of Physics, p. 124005. DOI: 10.1063/5.0023533 (cit. on p. 44).

[Tey+08] M. K. Tey, Z. Chen, S. A. Aljunid, B. Chng, F. Huber, G. Maslennikov, and C. Kurtsiefer: *Strong interaction between light and a single trapped atom without the need for a cavity*. Nature Physics **4**.12 (2008), pp. 924–927. DOI: 10.1038/nphys1096 (cit. on p. 19).

[Tin04] M. Tinkham: *Introduction to superconductivity*. 2. ed. Dover books on physics. Mineola, NY: Dover Publ., 2004. URL: http://www.gbv.de/dms/ilmenau/toc/378058371.PDF (cit. on pp. 9, 10).

[TL08] T. S. Tsoi and C. K. Law: *Quantum interference effects of a single photon interacting with an atomic chain inside a one-dimensional waveguide*. Physical Review A **78**.6 (2008), p. 063832. DOI: 10.1103/PhysRevA.78.063832 (cit. on pp. 32, 67, 69, 70).

[VIK98] M. R. Vladimirova, E. L. Ivchenko, and A. V. Kavokin: *Exciton polaritons in long-period quantum-well structures*. Semiconductors **32**.1 (1998), pp. 90–95. DOI: 10.1134/1.1187364 (cit. on p. 126).

[VD17] U. Vool and M. H. Devoret: *Introduction to Quantum Electromagnetic Circuits*. International Journal of Circuit Theory and Applications **45**.7 (2017), pp. 897–934. DOI: 10.1002/cta.2359 (cit. on pp. 13, 49).

[Wal+04] A. Wallraff, D. I. Schuster, A. Blais, L. Frunzio, R. S. Huang, J. Majer, S. Kumar, S. M. Girvin, and R. J. Schoelkopf: *Strong coupling of a single photon to a superconducting qubit using circuit quantum electrodynamics*. Nature **431**.7005 (2004), pp. 162–167. DOI: 10.1038/nature02851 (cit. on p. 2).

[Wan+14] H. Wang, X. Gu, Y.-x. Liu, A. Miranowicz, and F. Nori: *Optomechanical analog of two-color electromagnetically induced transparency: Photon transmission through an optomechanical device with a two-level system*. Phys. Rev. A **90** (2014), p. 023817. DOI: 10.1103/PhysRevA.90.023817 (cit. on p. 84).

[Wen+11] J. Wenner, M. Neeley, R. C. Bialczak, M. Lenander, E. Lucero, A. D. O'Connell, D. Sank, H. Wang, M. Weides, A. N. Cleland, and J. M. Martinis: *Wirebond crosstalk and cavity modes in large chip mounts for superconducting qubits*. Superconductor Science and Technology **24**.6 (2011), p. 065001. DOI: 10.1088/0953-2048/24/6/065001 (cit. on p. 93).

[Wie+97] D. S. Wiersma, P. Bartolini, A. Lagendijk, and R. Righini: *Localization of light in a disordered medium*. Nature **390**.6661 (1997), pp. 671–673. DOI: 10.1038/37757 (cit. on p. 84).

[WR20] L. A. Williamson and J. Ruostekoski: *Optical response of atom chains beyond the limit of low light intensity: The validity of the linear classical oscillator model*. Physical Review Research **2**.2 (2020). Publisher: American Physical Society, p. 023273. DOI: 10.1103/PhysRevResearch.2.023273 (cit. on p. 25).

[WS10] D. Witthaut and A. S. Sørensen: *Photon scattering by a three-level emitter in a one-dimensional waveguide*. New Journal of Physics **12**.4 (2010), p. 043052. DOI: 10.1088/1367-2630/12/4/043052 (cit. on pp. 36, 74, 84, 85, 88).

[Wu+17] X. Wu, J. L. Long, H. S. Ku, R. E. Lake, M. Bal, and D. P. Pappas: *Overlap junctions for high coherence superconducting qubits*. Applied Physics Letters **111**.3 (2017). Publisher: American Institute of Physics, p. 032602. DOI: 10.1063/1.4993937 (cit. on p. 44).

[YRZ01] M. Yan, E. G. Rickey, and Y. Zhu: *Electromagnetically induced transparency in cold rubidium atoms*. JOSA B **18**.8 (2001). Publisher: Optical Society of America, pp. 1057–1062. DOI: 10.1364/JOSAB.18.001057 (cit. on pp. 28, 78, 82).

[Yan+20] P. Yang, J. D. Brehm, J. Leppäkangas, L. Guo, M. Marthaler, I. Boventer, A. Stehli, T. Wolz, A. V. Ustinov, and M. Weides: *Probing the Tavis-Cummings Level Splitting with Intermediate-Scale Superconducting Circuits*. Physical Review Applied **14**.2 (2020). Publisher: American Physical Society, p. 024025. DOI: 10.1103/PhysRevApplied.14.024025 (cit. on pp. 2, 60).

[YF04] M. F. Yanik and S. Fan: *Stopping Light All Optically*. Phys. Rev. Lett. **92** (2004), p. 083901. DOI: 10.1103/PhysRevLett.92.083901 (cit. on pp. 75, 82).

[Yan+04] M. F. Yanik, W. Suh, Z. Wang, and S. Fan: *Stopping Light in a Waveguide with an All-Optical Analog of Electromagnetically Induced Transparency*. Phys. Rev. Lett. **93** (2004), p. 233903. DOI: 10.1103/PhysRevLett.93.233903 (cit. on pp. 75, 82).

[Yeh+17] J.-H. Yeh, J. LeFebvre, S. Premaratne, F. C. Wellstood, and B. S. Palmer: *Microwave attenuators for use with quantum devices below 100 mK*. Journal of Applied Physics **121**.22 (2017). Publisher: American Institute of Physics, p. 224501. DOI: 10.1063/1.4984894 (cit. on p. 51).

[ZFR16] A. M. Zagoskin, D. Felbacq, and E. Rousseau: *Quantum metamaterials in the microwave and optical ranges*. EPJ Quantum Technology **3**.1 (2016). DOI: 10.1140/epjqt/s40507-016-0040-x (cit. on p. 3).

[ZM19] Y.-X. Zhang and K. Mølmer: *Theory of Subradiant States of a One-Dimensional Two-Level Atom Chain*. Phys. Rev. Lett. **122** (2019), p. 203605. DOI: 10.1103/PhysRevLett.122.203605 (cit. on p. 126).

[ZB19] X. H. H. Zhang and H. U. Baranger: *Heralded Bell State of Dissipative Qubits Using Classical Light in a Waveguide*. Physical Review Letters **122**.14 (2019), p. 140502. DOI: 10.1103/PhysRevLett.122.140502 (cit. on p. 3).

[ZB13] H. Zheng and H. U. Baranger: *Persistent Quantum Beats and Long-Distance Entanglement from Waveguide-Mediated Interactions*. Phys. Rev. Lett. **110** (2013), p. 113601. DOI: 10.1103/PhysRevLett.110.113601 (cit. on p. 97).

[Zho+20] J. Zhong, N. A. Olekhno, Y. Ke, A. V. Poshakinskiy, C. Lee, Y. S. Kivshar, and A. N. Poddubny: *Photon-Mediated Localization in Two-Level Qubit Arrays*. Phys. Rev. Lett. **124** (2020), p. 093604. DOI: 10.1103/PhysRevLett.124.093604 (cit. on pp. 3, 97).

[Zum+08] G. Zumofen, N. M. Mojarad, V. Sandoghdar, and M. Agio: *Perfect Reflection of Light by an Oscillating Dipole*. Physical Review Letters **101**.18 (2008). Publisher: American Physical Society, p. 180404. DOI: 10.1103/PhysRevLett.101.180404 (cit. on p. 19).

List of Publications

[Bil+21] A. Bilmes, S. Volosheniuk, J. D. Brehm, A. V. Ustinov, and J. Lisenfeld: *Quantum sensors for microscopic tunneling systems*. npj Quantum Information **7**.1 (2021), p. 27. DOI: 10.1038/s41534-020-00359-x.

[Bre+17] J. D. Brehm, A. Bilmes, G. Weiss, A. V. Ustinov, and J. Lisenfeld: *Transmission-line resonators for the study of individual two-level tunneling systems*. Applied Physics Letters **111**.11 (2017). Publisher: American Institute of Physics, p. 112601. DOI: 10.1063/1.5001920.

[Bre+21] J. D. Brehm, A. N. Poddubny, A. Stehli, T. Wolz, H. Rotzinger, and A. V. Ustinov: *Waveguide bandgap engineering with an array of superconducting qubits*. npj Quantum Materials **6**.1 (2021), p. 10. DOI: 10.1038/s41535-021-00310-z.

[Lep+19] J. Leppäkangas, J. D. Brehm, P. Yang, L. Guo, M. Marthaler, A. V. Ustinov, and M. Weides: *Resonance inversion in a superconducting cavity coupled to artificial atoms and a microwave background*. Physical Review A **99**.6 (2019). Publisher: American Physical Society, p. 063804. DOI: 10.1103/PhysRevA.99.063804.

[Ste+20] A. Stehli, J. D. Brehm, T. Wolz, P. Baity, S. Danilin, V. Seferai, H. Rotzinger, A. V. Ustinov, and M. Weides: *Coherent superconducting qubits from a subtractive junction fabrication process*. Applied Physics Letters **117**.12 (2020). Publisher: American Institute of Physics, p. 124005. DOI: 10.1063/5.0023533.

[Yan+20] P. Yang, J. D. Brehm, J. Leppäkangas, L. Guo, M. Marthaler, I. Boventer, A. Stehli, T. Wolz, A. V. Ustinov, and M. Weides: *Probing the Tavis-Cummings Level Splitting with Intermediate-Scale Superconducting Circuits*. Physical Review Applied **14**.2 (2020). Publisher: American Physical Society, p. 024025. DOI: 10.1103/PhysRevApplied.14.024025.

Appendix

A Fabrication parameters

A.1 Sample A

The fabrication steps listed in Tab. 1 were consecutively executed to fabricate sample A (8 qubit metamaterial).

Table 1: Consecutive steps for the fabrication of Sample A (8 qubit metamaterial) with description of involved devices and parameters.

#	Step (Device)	Parameters
1	substrate cleaning	H_2SO_4+H_2O_2, 10 min
2	substrate cleaning	NEP+IPA right before resist appl.
3	EL-13 spin coating (Polos MCD 200)	ramp rate: 1000 rpm/s, spin speed: 2000 rpm, spin time: 100 s, HP: 200 °C, 5 min
4	A-4 spin coating (Polos MCD 200)	ramp rate: 1000 rpm/s, spin speed: 2000 rpm, spin time: 100 s, HP: 200 °C, 5 min
5	gold sputtering (Kresington)	time: 30 s, current: 30 mA
6	e-beam exposure (JEOL JBX-5500ZD)	
7	gold removal	15 s Lugol solution (15 %)
8	resist development	IPA/H_2O 3:1 @ 6 °C, 90 s
9	O_2-plasma clean	flow: 15 %, power: 76 %, time: 6 min
10	shadow evap. (Plassys MEB550s)	
	(1) descum	5 sccm Ar/10 sccm O_2, voltage: 400 V, current: 15 mA, time: 40 s
	(2) Al evaporation	rate: 1 nm/s, thickness: 45 nm, angle: $+30.00°$
	(3) oxidation	static, O_2-pressure: 10 mbar, time: 10 min
	(4) Al evaporation	rate: 1 nm/s, thickness: 55 nm, angle: $-30.00°$
11	lift-off	NEP @ 90 °C for 4 h + ultrasonic bath

12	S1805 spin coating (Polos MCD 200)	ramp rate: 500 rpm/s, ramp speed: 500 rpm, ramp time: 5 s, spin speed: 4500 rpm, spin time: 100 s, reflow: 30 s, HP: 115 °C, 1 min
13	optical exposure (Carl Suess MA6)	dose: 13 (mW/cm^2), contact mode: hard, time: 4 s
14	resist development	MF 319, time: 30 s, stop development in H_2O
15	Al evaporation (Plassys MEB550s)	
	(1) descum	5 sccm Ar/10 sccm O_2, voltage: 400 V, current: 15 mA, time: 20 s
	(2) Al evaporation	rate: 1 nm/s, thickness: 75 nm, angle: 0.00°
16	lift-off	NEP @ 90 °C for 4 h + ultrasonic bath

A.2 Sample B

The fabrication steps listed in Tab. 2 were consecutively executed to fabricate sample B (90 qubit metamaterial).

Table 2: Consecutive steps for the fabrication of Sample B (90 qubit metamaterial) with description of involved devices and parameters.

#	Step (Device)	Parameters
1	substrate cleaning	H_2SO_4+H_2O_2, 10 min
2	substrate cleaning	NEP+IPA right before resist appl.
3	EL-13 spin coating (Polos MCD 200)	ramp rate: 1000 rpm/s, spin speed: 2000 rpm, spin time: 100 s, HP: 200 °C, 5 min
4	A-4 spin coating (Polos MCD 200)	ramp rate: 1000 rpm/s, spin speed: 2000 rpm, spin time: 100 s, HP: 200 °C, 5 min
5	gold sputtering (Kresington)	time: 15 s, current: 30 mA
6	e-beam exposure (JEOL JBX-5500ZD)	
7	gold removal	15 s Lugol solution (15 %)
8	resist development	IPA/H_2O 3:1 @ 6 °C, 88 s
9	O_2-plasma clean	flow: 15 %, power: 80 %, time: 6 min
10	shadow evap. (Plassys MEB550s)	
	(1) descum	5 sccm Ar/10 sccm O_2, voltage: 400 V, current: 15 mA, time: 120 s
	(2) Al evaporation	rate: 1 nm/s, thickness: 45 nm, angle: +24.00°
	(3) oxidation	static, O_2-pressure: 25 mbar, time: 90 min
	(4) Al evaporation	rate: 1 nm/s, thickness: 55 nm, angle: −24.00°

11	lift-off	NEP @ 90 °C for 4 h + ultrasonic bath
12	EL-13 spin coating (Polos MCD 200)	ramp rate: 1000 rpm/s, spin speed: 2000 rpm, spin time: 100 s, HP: 200 °C, 5 min
13	A-4 spin coating (Polos MCD 200)	ramp rate: 1000 rpm/s, spin speed: 2000 rpm, spin time: 100 s, HP: 200 °C, 5 min
14	gold sputtering (Kresington)	time: 15 s, current: 30 mA
15	e-beam exposure (JEOL JBX-5500ZD)	
16	gold removal	15 s Lugol solution (15 %)
17	optical exposure (Carl Suess MA6)	constant power: 500 W, contact mode: hard, time: 2100 s
18	resist development	IPA/H_2O 3:1 @ 6 °C, 84 s
19	Al evaporation (Plassys MEB550s)	
	(1) descum	5 sccm Ar/10 sccm O_2, voltage: 400 V, current: 15 mA, time: 20 s
	(2) Al evaporation	rate: 1 nm/s, thickness: 75 nm, angle: 0.00°
20	lift-off	NEP @ 90 °C for 4 h + ultrasonic bath

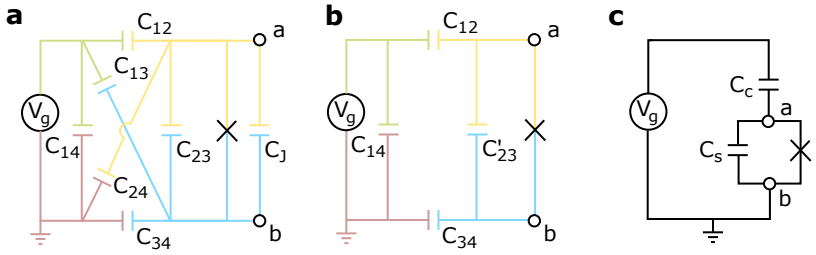

Figure 1: (a) Full capacitance network of the transmon qubit. (b) Simplified network after neglecting small cross-capacitances C_{24} and C_{13} and absorbing the junction capacitance C_J in C'_{23}. (c) Effective circuit of a transmon qubit.

B Derivations and Calculations

B.1 Capacitance Network of the Transmon Qubit

In the following the effective transmon circuit (compare Fig. 1(c)) is derived from its actual circuit as implemented in the experiment (Fig. 1(a)). To simplify the following calculation, the cross-capacitances C_{24} and C_{13} are neglected (compare Fig. 1(b)). Numerical simulations of the capacitance matrix indicate that this is well justified for the used geometries. The intrinsic junction capacitance C_J is absorbed into $C'_{23} = C_{23} + C_J$. By using Thevenin's theorem the circuit of Fig. 1(b) can be replaced by a renormalized voltage source $V' = \beta V_g = V_a - V_b$ and one effective capacitance C_Σ. The latter is extracted by replacing the voltage source by a short:

$$C_\Sigma = C'_{23} + \left(\frac{1}{C_{12}} + \frac{1}{C_{14}} + \frac{1}{C_{34}}\right)^{-1} \approx C'_{23} + \frac{C_{12}C_{34}}{C_{12} + C_{34}} \tag{1}$$

In the last step $C_{14} \to \infty$ was assumed. It is now instructive to split C_Σ into two parallel capacitances (C_s and C_c with $\beta = C_c/(C_s + C_c) = C_c/C_\Sigma$ as depicted in Fig. 1(c)), acting as a voltage divider by the factor β to regain the original voltage V_g driving the circuit. The Thevenin voltage $V_a - V_b = V'$ can be related with V_g via Kirchhoff relations:

$$0 = V_a(C_{12} + C'_{23}) - V_g C_{12} - V_b C'_{23} \tag{2}$$

$$0 = V_b(C'_{23} + C_{34}) - V_a C'_{23} \tag{3}$$

Thus, β is given by:

$$\beta = \frac{V_a - V_b}{V_g} = \frac{C_{12}C_{34}}{C'_{23}C_{34} + C_{12}(C'_{23} + C_{34})} \tag{4}$$

The coupling capacitance is therefore given by:

$$C_c = \beta C_\Sigma = \frac{C_{12}C_{34}}{C_{12}+C_{34}} \tag{5}$$

The total effective capacitance can then be re-expressed by $C_\Sigma = C_c + C_{23} + C_J$.

B.2 Transformation in a Doubly-Rotating Frame

This derivation is based on the calculations presented in reference [Hoi13]. The Hamiltonian of a three level system with the levels $|0\rangle$, $|1\rangle$, $|2\rangle$ at frequencies ω_0, ω_1, ω_2 under the influence of two classical drives at strengths Ω_p, Ω_c and frequencies ω_p and ω_c is given by:

$$H = \hbar \begin{pmatrix} \omega_0 & 0 & 0 \\ 0 & \omega_1 & 0 \\ 0 & 0 & \omega_2 \end{pmatrix} + \hbar \begin{pmatrix} 0 & \Omega_p \cos\omega_p t & 0 \\ \Omega_p \cos\omega_p t & 0 & \Omega_c \cos\omega_c t \\ 0 & \Omega_c \cos\omega_c t & 0 \end{pmatrix} \tag{6}$$

In the next step the goal is to find a unitary transformation U, which eliminates all time dependent oscillating parts of both drives in the Hamiltonian. As an ansatz for U we chose:

$$U(t) = \begin{pmatrix} \exp(i\phi_0(t)) & 0 & 0 \\ 0 & \exp(i\phi_1(t)) & 0 \\ 0 & 0 & \exp(i\phi_2(t)) \end{pmatrix} \quad \text{with} \quad \phi_i(t) \in \mathbb{R} \tag{7}$$

It is easy to check that $U(t)$ fulfills $UU^\dagger = \mathbb{1}$. Applying the transformation of Eq. 7 to Eq. 6 yields:

$$\begin{aligned} \frac{H'}{\hbar} &= U(t)HU^\dagger(t)/\hbar - iU(t)\dot{U}^\dagger(t) \\ &= \begin{pmatrix} \omega_0 - \dot{\phi_0}(t) & \frac{\Omega_p(1+\exp(-2i\omega_p t))}{2\exp(i(-\omega_p t-\phi_0(t)+\phi_1(t)))} & 0 \\ \frac{\Omega_p(1+\exp(2i\omega_p t))}{2\exp(i(\omega_p t+\phi_0(t)-\phi_1(t)))} & \omega_1 - \dot{\phi_1}(t) & \frac{\Omega_c(1+\exp(-2i\omega_c t))}{2\exp(i(-\omega_c t-\phi_1(t)+\phi_2(t)))} \\ 0 & \frac{\Omega_c(1+\exp(2i\omega_c t))}{2\exp(i(\omega_c t+\phi_1(t)-\phi_2(t)))} & \omega_2 - \dot{\phi_2}(t) \end{pmatrix} \end{aligned} \tag{8}$$

Neglecting the fast rotating terms ($\exp(\pm 2i\omega_p t) \approx \exp(\pm 2i\omega_c t) \approx 0$) and using the following constraints,

$$\omega_0 - \dot{\phi_0}(t) = 0 \tag{9}$$

$$-\omega_p t - \phi_0(t) + \phi_1(t) = 0 \tag{10}$$

$$-\omega_c t - \phi_1(t) + \phi_2(t) = 0 \tag{11}$$

the transformed Hamiltonian in the doubly-rotating frame evaluates to:

$$H' \approx \hbar \begin{pmatrix} 0 & \frac{\Omega_\mathrm{p}}{2} & 0 \\ \frac{\Omega_\mathrm{p}}{2} & \omega_{10} - \omega_\mathrm{p} & \frac{\Omega_\mathrm{c}}{2} \\ & \frac{\Omega_\mathrm{c}}{2} & \omega_{21} - \omega_\mathrm{c} + \omega_{10} - \omega_\mathrm{p} \end{pmatrix} \tag{12}$$

Here, the frequency differences ($\omega_{10} = \omega_1 - \omega_0$, $\omega_{21} = \omega_2 - \omega_1$) are used.

B.3 Decoherence Rates of a Three-Level System

The non-unitarian part of the Lindblad master equation is given by the sum of dissipators $\Gamma_{ij}\mathcal{D}[A]\rho = \Gamma_{ij}[A\rho A^\dagger - \frac{1}{2}\{A^\dagger A, \rho\}]$ of all decoherence channels of the system under investigation. For a ladder-type three level system, which is subject to relaxation (but no thermal activation) and pure dephasing (with rates Γ_{ij} and Γ_ϕ^{ij} for the $i \to j$ transition) the sum of all dissipators is given by [GR16]:

$$\begin{aligned} \mathcal{L}[\rho] &= \Gamma_{10}\mathcal{D}[\sigma_{01}]\rho + \Gamma_{21}\mathcal{D}[\sigma_{12}]\rho + \Gamma_{20}\mathcal{D}[\sigma_{02}]\rho \\ &+ \frac{\Gamma_\phi^{20}}{2}\mathcal{D}[\sigma_{22} - \sigma_{00}] + \frac{\Gamma_\phi^{21}}{2}\mathcal{D}[\sigma_{22} - \sigma_{11}] + \frac{\Gamma_\phi^{10}}{2}\mathcal{D}[\sigma_{11} - \sigma_{00}] \\ &= \begin{pmatrix} \Gamma_{10}\rho_{11} + \Gamma_{20}\rho_{22} & -\gamma_{01}\rho_{01} & -\gamma_{02}\rho_{02} \\ -\gamma_{10}\rho_{10} & -\Gamma_{10}\rho_{11} + \Gamma_{21}\rho_{22} & -\gamma_{12}\rho_{12} \\ -\gamma_{20}\rho_{20} & -\gamma_{20}\rho_{20} & -\Gamma_{20}\rho_{22} - \Gamma_{21}\rho_{22} \end{pmatrix} \end{aligned} \tag{13}$$

with $\sigma_{ij} = |i\rangle\langle j|$, $\rho = \sum_{i,j=0}^{2} \rho_{ij} |i\rangle\langle j|$ and the effective decoherence rates $\gamma_{ij} = \gamma_{ji}$ as introduced in Sec. 3.1.2 of the main text:

$$\gamma_{10} = \frac{\Gamma_{10}}{2} + \Gamma_\phi^{10} + \frac{1}{4}(\Gamma_\phi^{20} + \Gamma_\phi^{21}) \tag{14}$$

$$\gamma_{20} = \frac{1}{2}(\Gamma_{20} + \Gamma_{21}) + \Gamma_\phi^{20} + \frac{1}{4}(\Gamma_\phi^{10} + \Gamma_\phi^{21}) \tag{15}$$

$$\gamma_{21} = \frac{1}{2}(\Gamma_{20} + \Gamma_{21} + \Gamma_{10}) + \Gamma_\phi^{21} + \frac{1}{4}(\Gamma_\phi^{10} + \Gamma_\phi^{20}) \tag{16}$$

Note that γ_{20} has a contribution of the $2 \to 1$ relaxation, which makes the $2 \to 0$ decoherence rate comparably large, even in the limit of negligible pure dephasing and $\Gamma_{20} = 0$. The implications on electromagnetically induced transparency is discussed in the main text in Sec. 5.5.1.

B.4 Relation between S-Matrix and Susceptibility

The linear electrical susceptibility χ is defined as:

$$P = \epsilon_0 \chi E \tag{17}$$

P is the polarization and E the electrical field. Simultaneously the polarization is defined as total dipolemoment μ per volume:

$$P = -\frac{\langle \mu \rangle}{V} = -\frac{\mathrm{Tr}(\rho\mu)}{V} \approx -2\frac{\mu_{10}\rho_{10}}{V} \tag{18}$$

In the last step only the contributions of the $0 \rightarrow 1$ transition to the optical susceptibility where included and all other therms were dropped, since in this work the optical response of the qubits is only probed around this transition. Combining Eqs. 17 and 18 yields:

$$\chi \propto \rho_{10} \tag{19}$$

Simultaneously, Eqs. 3.9, 3.9 and 3.12 of the main text and Eq. 19 indicate that $S_{22} \propto \chi$.

B.5 Linewidth Scaling of Polariton Modes

In the following, an analytical expression for the subradiant state linewidth Γ_ξ in the single excitation sector is derived. The derivation is taken from the supplementary material of Ref. [Bre+21] and was performed by A. N. Poddubny.

In order to extract Γ_ξ, only the interaction term of H_{eff} (Eq. 3.30) in the main text is used:

$$H_{\mathrm{rs}} = -i\frac{\Gamma_{1\mathrm{D}}}{2}\exp(i\phi|r-s|) \quad \text{with} \quad \phi = \frac{\omega_{10}d}{c} \tag{20}$$

with H_{rs} being the interaction matrix element between qubit r and s. The inverse Hamiltonian of (20) $[H^{-1}]_{\mathrm{rs}}$ is exactly 3-diagonal [Pod20]:

$$[H^{-1}]_{\mathrm{rs}} = \frac{2}{\Gamma_{1\mathrm{D}}}\begin{pmatrix} -\frac{1}{2}\cot\phi + \frac{i}{2} & \frac{1}{2\sin\phi} & 0 & \cdots \\ \frac{1}{2\sin\phi} & -\cot\phi & \frac{1}{2\sin\phi} & \cdots \\ & \ddots & \ddots & \\ \cdots & \frac{1}{2\sin\phi} & -\cot\phi & \frac{1}{2\sin\phi} \\ \cdots & 0 & \frac{1}{2\sin\phi} & -\frac{1}{2}\cot\phi + \frac{i}{2} \end{pmatrix} \tag{21}$$

This means that the Schroedinger equation

$$H^{-1}\psi_\xi = \frac{1}{\omega_\xi}\psi_\xi \tag{22}$$

of the inverse Hamiltonian is just a tight-binding model. The radiative decay due to the photon escape into the waveguide is present only at the edges of the qubit

array and can be treated as a perturbation. For the lower polariton branch the following eigenenergies is obtained [ZM19; VIK98]:

$$\frac{\Gamma_{1D}/2}{\omega_\xi} = -\frac{2}{\phi}\sin^2\frac{k}{2} - \frac{2i}{N}\cos^2\frac{k}{2}, \qquad k = \frac{\xi\pi}{N} \tag{23}$$

where $\xi = 1, 2, ...N-1$ is the eigenmode number, sorted from the brightest (largest linewidth $= \Im(\omega_\xi)$) to the darkest (smallest linewidth). The solution of Eq. 23 can be recovered most easily in the limit $\phi \ll k \ll \pi$. In this case one can assume that $\cot\phi \approx 1/\sin\phi = 1/\phi$. Neglecting the radiative decay, the Schroedinger equation Eq. 22 yields the usual parabolic dispersion,

$$\frac{\Gamma_{1D}/2}{\omega_\xi^{(0)}} = -\frac{k^2}{2\phi}, \quad \psi_{\xi,s} = \sqrt{\frac{2}{N}}\cos k(s-\tfrac{1}{2})\,. \tag{24}$$

Now the radiative decay in Eq. 21 is taken into account by considering the imaginary terms in the first order of the perturbation theory:

$$\frac{\Gamma_{1D}/2}{\omega_\xi} = \frac{\Gamma_{1D}/2}{\omega_\xi^{(0)}} + \frac{i}{2}(|\psi_{\xi,1}|^2 + |\psi_{\xi,N}|^2) = -\frac{\pi^2\xi^2}{2\phi N^2} + \frac{2i}{N}\,, \tag{25}$$

which is equivalent to Eq. 23 in the considered limit of small $\xi \ll N$. Inverting Eq. 25 we find for $\phi \ll 1$

$$\Gamma_\xi = 2\mathrm{Im}(\omega_\xi) = \frac{8\Gamma_{1D}N^3\phi^2}{\xi^4\pi^4}\,. \tag{26}$$

B.6 Fano Interference of Polaritonic Modes

In the following, the Fano-type interference between a detuned qubit and the collective modes of an ensemble of resonant qubits is derived. The derivation is taken from the supplementary material of Ref. [Bre+21] and was performed by A. N. Poddubny.

In this section light reflection from the N-qubit array is considered, where first $N-1$ qubits are in resonance and the last qubit is detuned from the resonance. The goal is to explain analytically the disappearance of the reflection dips for certain values of the detuning, for example at the frequency 7.894 GHz in Fig. 5.10 of the main text. In order to obtain a better understanding of the resonances in the reflection, an approach based on the Hamiltonian of Eq. 20 is used. When the inductances $L_{1,2}$ at the waveguide edges, leading to additional reflections, are not taken into account, this approach is exactly equivalent to the transfer matrix

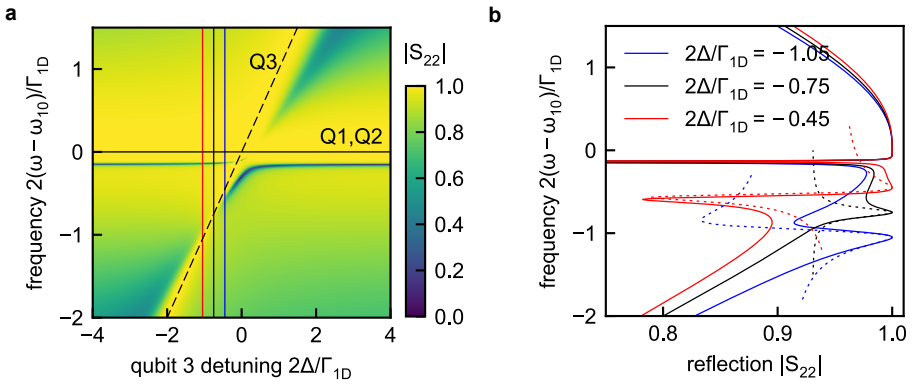

Figure 2: (a) Reflection spectra from an array of 3 qubits where the first two are tuned to the the frequency ω_{10} (solid horizontal line) and last one to $\omega_{10}+\Delta$ (dashed inclined line). (b) Reflection spectra for three values of detuning, that are indicated on the graph, and shown by the vertical lines in (a). Solid curves present the results of a numerical calculation using Eq. 28, dashed curves have been obtained from the analytical Eq. 32. The calculation has been performed for $\phi=\omega_0 d/c=0.15$.

method [INJ94; KP07]. First, the equation for the dimensionless dipole moments of the qubits ψ_s, induced by the incoming wave at the frequency ω, is solved

$$\sum_{s=1}^{N}[H_{rs}+(\omega_s-\omega)\delta_{rs}]\psi_s=e^{i(r-1)\phi}\,,\quad r=1\ldots N\,, \tag{27}$$

where it is assumed that the qubits are located at the points $x=0,d,\ldots(N-1)d$. After the dipole moments ψ_s have been found from the solution of the system Eq. 27, the amplitude reflection and transmission coefficients r and t are given by

$$r=\frac{i\Gamma_{1D}}{2}\sum_{s=1}^{N}\psi_s e^{-i(s-1)\phi},\quad t=1+\frac{i\Gamma_{1D}}{2}\sum_{s=1}^{N}\psi_s e^{i(s-1)\phi}\,. \tag{28}$$

In the Markovian approximation the phase $\phi=\omega d/c$ in Eqs. 27,28 is evaluated at the qubit resonance frequency, $\phi=\omega_{10}d/c$. Hence, Eqs. 27,28 reduce to a standard input-output problem.

Now, the interferences in reflection for the specific case of $N=3$ qubits with the resonance frequencies ω_{10},ω_{10} and $\omega_{10}+\Delta$ will be illustrated. The goal is to examine the light-induced coupling between the resonant dimer formed by the first two qubits with the last qubit and the Fano-like interferences in more detail. Due to the dense qubit spacing ($\phi\ll 1$), the first two resonant qubits can be described by

a symmetric superradiant state, $\psi_1 = \psi_2 = \frac{1}{\sqrt{2}}\psi_{\mathrm{SR}}$. As a result, the system Eq. 27 in the reduced basis reads

$$\begin{aligned} (\omega_{10} - i\Gamma_{1\mathrm{D}} - \omega)\,\psi_{\mathrm{SR}} &- \frac{i\Gamma_{1\mathrm{D}}}{2\sqrt{2}}(e^{i\phi} + e^{2i\phi})\psi_3 = \frac{1 + e^{i\phi}}{\sqrt{2}}\,, \\ \left(\omega_{10} + \Delta - \frac{i\Gamma_{1\mathrm{D}}}{2} - \omega\right)\psi_3 &- \frac{i\Gamma_{1\mathrm{D}}}{2\sqrt{2}}(e^{i\phi} + e^{2i\phi})\psi_{\mathrm{SR}} = e^{2i\phi}\,. \end{aligned} \tag{29}$$

and the reflection coefficient is given by

$$r = \frac{i\Gamma_{1\mathrm{D}}}{2}\left(\frac{1 + e^{i\phi}}{\sqrt{2}}\psi_{\mathrm{SR}} + e^{2i\phi}\psi_3\right)\,. \tag{30}$$

In the following, the frequency range is restricted to the case where the frequency is close to the detuned qubit resonance, i.e.

$$|\omega - \omega_{10} - \Delta| \ll \Delta\,. \tag{31}$$

In this spectral range the reflection coefficient Eq. 30, obtained from the system Eq. 29, can be approximately presented as

$$r \approx -ir_0\frac{\omega - \omega_{10} - \Delta + \frac{\Gamma_{1\mathrm{D}}}{2}(1/r_0^* + i)}{\omega - \omega_{10} - \Delta + \frac{\Gamma_{1\mathrm{D}}}{2}(r_0 + i)} \tag{32}$$

where

$$r_0 = \frac{1}{i + \frac{1}{3}(2\Delta/\Gamma_{1\mathrm{D}} + 5\phi) - \frac{4i\phi}{3}\Delta/\Gamma_{1\mathrm{D}}}\,, \tag{33}$$

and assuming that $\phi \ll 1$. Here, Eq. 33 describes the slow varying background of the reflection coefficient Eq. 32. This background corresponds to the mode, where the third qubit oscillates in phase with the first two. This interpretation becomes most clear in the regime where all the qubits are in the same point, $\phi = 0$, so that

$$r_0 = \frac{3}{3i + 2\Delta/\Gamma_{1\mathrm{D}}}\,. \tag{34}$$

Equation Eq. 34 describes just the resonant reflection determined by the superradiant mode of 3 qubits [INJ94; Cha+12]. The second factor in the reflection coefficient Eq. 32 describes the resonant coupling of the last qubit with the superradiant mode. This factor has a resonance at the frequency $\omega_{10} + \Delta - \Re(r_0)\Gamma_{1\mathrm{D}}/2$ with the radiative decay rate $(1 + \Im(r_0))\Gamma_{1\mathrm{D}}/2$. Both the radiative decay and the position of the resonance depend on the phase of the background reflection Eq. 34 at the resonance frequency of the detuned qubit $\omega_{10} + \Delta$. This is very similar to the general picture of Fano interference between two scattering channels with broad and narrow spectral resonances, resulting in characteristic asymmetric spectral lines [Lim+17]. The

reflection coefficient Eq. 33 cannot be completely reduced to the Fano equation because, contrary to the Fano case, both the superradiant mode and the last qubit mode are directly coupled to the input and output channels in Eq. 29. However, Eq. 33 also yields asymmetric reflection spectra, as is demonstrated by the calculation in Fig. 2. In this figure (similarly to Fig. 5.10 of the main text), the numerically calculated reflection spectra in dependence on the detuning Δ are shown. The right panel presents the spectra for three values of the detuning (solid lines) compared with the analytical result Eq. 32 (dashed lines). Similarly to Fig. 5.10 of the main text, Fig. 2 has a blindspot for the detuning $2\Delta/\Gamma_{1D} = -0.75 = -5\phi$ (vertical black line in Fig. 5.10(a)). The calculation in Fig. 2(b) demonstrates that the exact result is well described by the approximation Eq. 32 in the vicinity of the resonance of the detuned qubit. It can be seen, that for $2\Delta/\Gamma_{1D} + 5\phi = 0$, the background reflection coefficient Eq. 33 becomes purely imaginary. As such, the background provides a constructively interfering contribution at the last qubit resonance and results in the symmetric reflection peak. This is demonstrated by the black curves in Fig. 2(b). When the last qubit frequency $\omega_{10} + \Delta$ is detuned from $\omega_{10} - (5/2)\Gamma_{1D}\phi$, the interference stops being constructive, resulting in the asymmetric reflection resonances (blue and red lines in Fig. 2(b)). The two-mode model Eq. 29, describing Fano-like interferences between the modes of the last qubit and the given mode of first $N-1$ resonant qubits, has a very general character. It can be generalized for arbitrary values of N, explaining the blind spots in Fig. 5.10 of the main text.

Acknowledgements

I want to thank Prof. Dr. Alexey Ustinov for giving me the opportunity to work in his group and for supervising this thesis. I am very grateful for the excellent working conditions and the well equipped labs he provided at the KIT. Thank you for countless discussions, advice and the possibilities to visit various conferences and seminars in many foreign countries.

I'd like to thank Prof. Dr. Alexander Shnirman for being the second reviewer of this work and for collaborating with us on developing a better understanding of localization effects in the metamaterial.

I want to express my gratitude to our collaborator Dr. Alexander Poddubny who provided valuable calculations which improved significantly the overall understanding of the eight qubit metamaterial. He never got tired in discussing various facets of this work.

Special thanks go to Dr. Hannes Rotzinger for his advice concerning fabrication techniques and many physics related discussions. Furthermore, I want to thank Prof. Dr. Martin Weides for the fruitful collaboration in exploring the Tavis-Cummings system.

It were the colleagues at the Institute of Physics who made my time at the institute memorable. Thank you for countless laughs, discussions about physics and life in general, great evenings at conferences and your help in so many situations. I'd also like to thank my colleagues Dr. Andre Schneider, Dr. Kirill Shulga, Dr. Alexander Bilmes, Alexander Stehli, Tim Wolz, Max Christen and Micha Wildermuth for carefully proofreading this Thesis.

I want to thank *team silverfridge*, consisting of Dr. Jochen Braumüller, Dr. Steffen Schlör and foremost Alexander Stehli, for sharing the burden of running a wet dilution cryostat which required numerous *emergency* visits at the lab.

I'd like to express my gratitude to the staff at the NSL (Nanostructure Service Laboratory) of the Center for Functional Nanostructures at Karlsruhe Institute of Technology. I am grateful that Lucas Radtke and Dr. Silvia Diewald introduced me

to the nano-fabrication of thin films and helped me untiringly through dozens of sample generations.

I acknowledge generous financial and ideological support from Studienstiftung des Deutschen Volkes. Through their large range of offered activities and seminars I learned a lot and had interesting discussions with my fellow stipendiaries.

Finally, I want to thank my parents for making me who I am and my dear wife Theresa for her love.

Karlsruhe, December 2020 M.Sc. Jan David Brehm